DOCTORAL DISSERTATION

Preparation of Macroporous Particles Decorated with Cellulose Nanofiber and Their Protein Adsorption Performance

（セルロースナノファイバが担持したマクロポーラス微粒子の合成とタンパク質吸着特性）

Written by

Annie Mufyda Rahmatika

Supervisor

Associate Professor Takashi Ogi

Thermal Fluid Engineering Laboratory

Department of Chemical Engineering

Graduate School of Engineering

Hiroshima University

September 2020

Abstract

Effective protein adsorption has attracted attention for broad application in the biomedical field. To date, continuous improvement on adsorbent particles was developed by the utilization of various materials or modifying their physicochemical properties to increase the ability of adsorption, which is adjustable according to the required application. This dissertation introduced a combination of TEMPO-oxidized cellulose nanofiber (TOCN) and macroporous particles through a spray process as the new material for advanced protein adsorbent. It aims to gain a better understanding of the effect of surface functional groups and nanostructures on the adsorption behavior of protein as one of the macromolecules. Several parameters in the process of synthesis and adsorption performance have been carried out to investigate the effectiveness of this combination and to understand whether the driving factors in the adsorption process. A brief description of each chapter in this dissertation is shown below.

Chapter 1 provides the background and motivation for current research on development powder technology in protein adsorption. The theoretical explanation and review of the previous studies were presented in the development of physicochemical properties modification of adsorbent.

At first, in **Chapter 2**, this dissertation focused on the scheme selection of an effective way to prepare the macroporous particle by the spray-templating method. Macroporous carbon particles were prepared through poly (methyl methacrylate) (PMMA) templating in the variation of PMMA concentration and particle size to evaluate the formation of macroporous structures. The characteristics of resulted microporous carbon particles are then compared with those produced through polystyrene latex (PSL) templating. It was found that with similar morphological results, the PMMA template reduced the energy consumption for decomposition and produced a higher specific surface area of macroporous carbon particles compared to that using the PSL template.

PMMA templating method then used for synthesis macroporous SiO_2 particles in **Chapter 3** as the host of TEMPO-oxidized cellulose nanofiber (TOCN)

deposition. The performance of TOCN decorated macroporous SiO_2 (TOCN@macroporous SiO_2) particles then evaluated for lysozyme adsorption. The mass ratio of TOCN and SiO_2 particles was varied to understand the contribution of each component as well as to obtain the optimum conditions. The results show that TOCN@macroporous SiO_2 particles have a unique cellulose nanofiber network structure on the macroporous with highly-negative zeta potential(-62 ± 2 mV) close to the zeta potential of TOCN but possess higher specific surface area. The presence of macroporous SiO_2 particles leads to the improvement of lysozyme adsorption 17% higher than TOCN particles. Furthermore, TOCN@macroporous SiO_2 particles have very high reusability (> 90% adsorption capacity) and good adsorbate release (> 80%) after 10 times of use.

In **Chapter 4**, the macropore size of silica particles was adjusted to understand how TOCN depositions decorate the macropore structure. In addition, the adsorption kinetics, thermodynamics, and isothermal parameters were studied to analyze the driving factors of protein adsorption. The result shows that the adsorption process occurred spontaneously at any temperature with adsorption equilibrium achieved before 10 minutes due to the contribution of electrostatic interaction and hydrogen bonding. Furthermore, the protein adsorption capacity depends on protein interaction with the carboxylate group and the accessible pore space of adsorbent. The pore size corresponding to the length of TOCN can affect the TOCN deposition both to the external surface or penetrate the macropore structure. This deposition behavior was resulting in a broad pore size distribution with abundant accessible active sites that can adsorb large molecules such as lysozyme through a multi-layer adsorption process *via* a pore-filling mechanism.

General conclusions of all topics are listed in **Chapter 5**.

Contents

Chapter 1

Introduction

Protein is one of the macromolecules with the most necessary functions in our lives. Protein adsorption is a complex process that plays a significant role in a variety of critical biological-related methods [1]. Therefore, in recent decades, numerous researches have been devoted to exploring various materials as adsorbent particles or modifying their physicochemical properties to increase the ability of protein adsorption, which is adjustable according to the required application.

1.1. Application of protein adsorption

The control process of protein adsorption on the surface of the adsorbent material following the specific requirements is needed for various applications, such as separation, purification, drug delivery agents, biosensors, and hemodiafiltration filtration. (**Figure 1.1**).

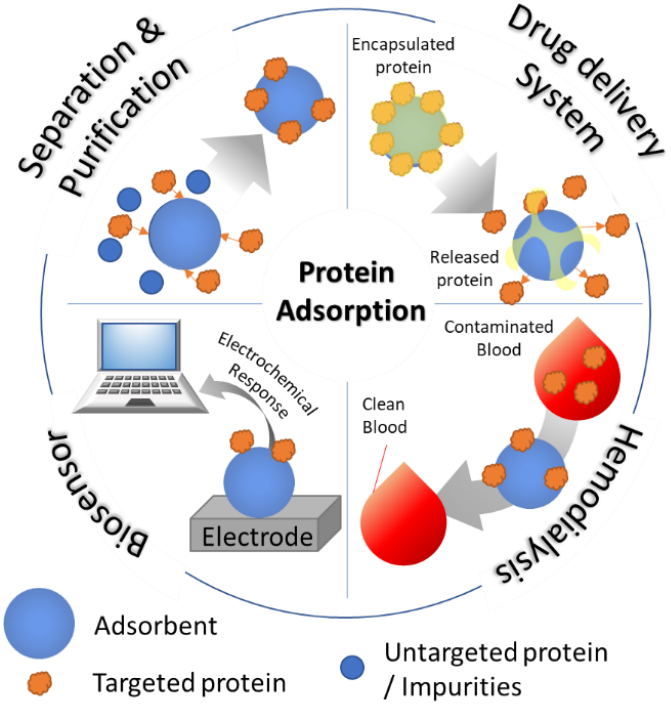

Figure 1.1 *Application of protein adsorption in the biomedical field*

1.1.1. Separation and purification

In bioseparation and purification technology, protein adsorption plays a vital role in separating the targeted protein from a complex mixture solution. Protein adsorption mainly performed by the micro-sized particle as an adsorbent in ion exchange and affinity chromatography. However, adsorbent particles were usually used in a packed column in chromatography has a poor mass transfer due to the small pore size of particles or low intraparticle connected channels [2,3]. As a result, long contacting time was required to allow the protein penetrates and fully adsorbed onto particles that lead to relatively low adsorption capacity. Therefore, designing adsorbents that are not only good at separation accuracy but also have a relatively high adsorption capacity, high surface area, and excellent mass transfer properties remains a significant challenge [4].

1.1.2. Drug delivery system

Protein adsorption also becomes a key for a successful drug delivery system because the protein drug was loaded on the carrier (adsorbent in drug delivery agent) particles by adsorption process. Adsorbing drugs on the nanostructured carrier particle can enhance drug physicochemical stability [5]. In addition, for poor-soluble protein drug, protein-drug carrier particles with high porosity are required to improve the solubility [6]. The high porosity carrier particles are enabling the better penetration of the solvent into the drug-excipient matrix. Therefore, designing the protein drug carrier that biocompatible, well-defined surface properties and consists of tunable pore sizes with a uniform porous structure are needed.

1.1.3. Biosensor

In diagnostic applications, such as biosensors, an adsorbent material should demonstrate the following characteristics. Good in selectivity, sensitivity, and specificity of the analyte to be tested[7]. For example, the selective adsorption of lysozyme from saliva, serum, urine, and tears for detecting leukemia, Alzheimer's, kidney failure, or renal disease [8–10]. In the process of adsorption in biosensor applications, adsorbent particles as a diagnostic material must be able to adsorb quickly and not easily disturbed by other components in the complex matrix of biological fluids. In this case, nanostructured composite particles with specific surface properties are usually used as a matrix to absorb selected proteins from human fluid samples.

1.1.4. Hemodiafiltration

Another application of protein adsorption is for the treatment of chronic hemodiafiltration. Usually, porous membranes were used in this field because it is effective at clearing small toxic compounds molecules like urea (small molecule) and β_2-microglobulin (middle molecule). Even though, unlike the natural kidney, the porous membrane is limited in clearing macromolecules (e.g., albumin)[11]. Thus, materials that mimic the structure or function of biological systems in certain aspects often encounter obstacles in practical applications. In other words, designing of biomolecular cleaning devices with efficient adsorption (can absorb small-macromolecules) become a big concern in this field.

From the above explanation, it cannot be denied that although adsorption of protein has many functions, designing advanced adsorbent particles that can be adapted to the required application is a big challenge.

1.2. Driving Force in Protein Adsorption

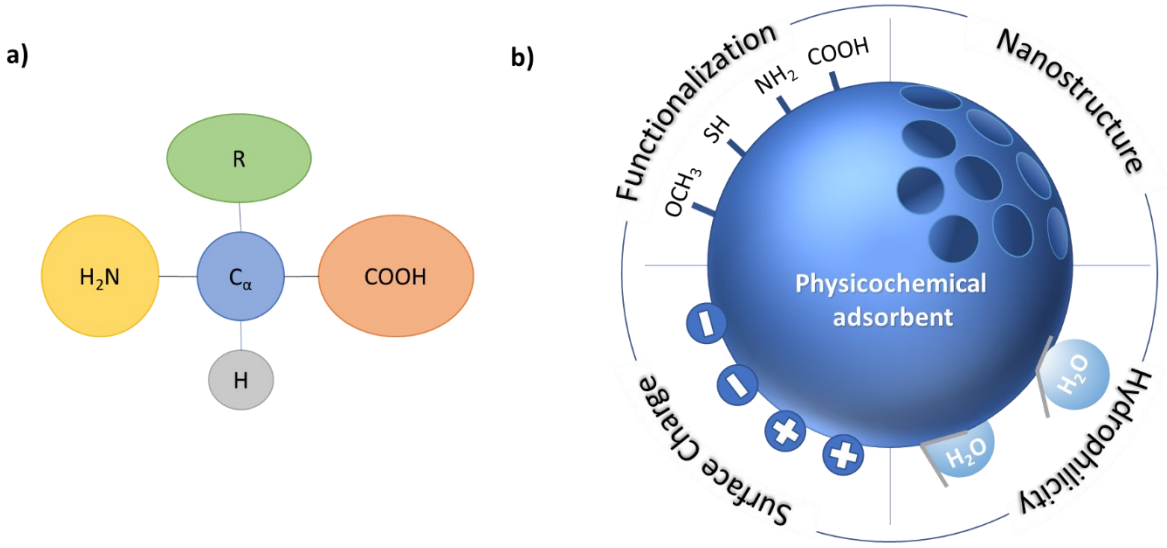

Figure 1.2 *a) Protein structure. b) The forces driving adsorption of proteins*

Proteins are composed of alpha-amino acids as their main building block [12]. As shown in **Figure 1.2a**, alpha-amino acids are consist of amine functional group, α-carbon, carboxylic acid functional group, and variable R-group. R-group itself consists of many variations, which then make amino acids have characteristics such as non-polar, positive and negative charged, and polar, in which each character tends specific physicochemical properties [13]. Based on these, the adsorbent particles were designed by the modification of physicochemical properties. The scenarios that usually carried out are controlling hydrophobicity, specific functionalization, and nanostructure (**Figure 1.2b).** Thus, the mechanism of protein adsorption can occur through the combinative forces of hydrophobic interaction, hydrogen bonding, electrostatic interactions, and van der Waals forces [14–19].

1.2.1 Effect of hydrophilicity

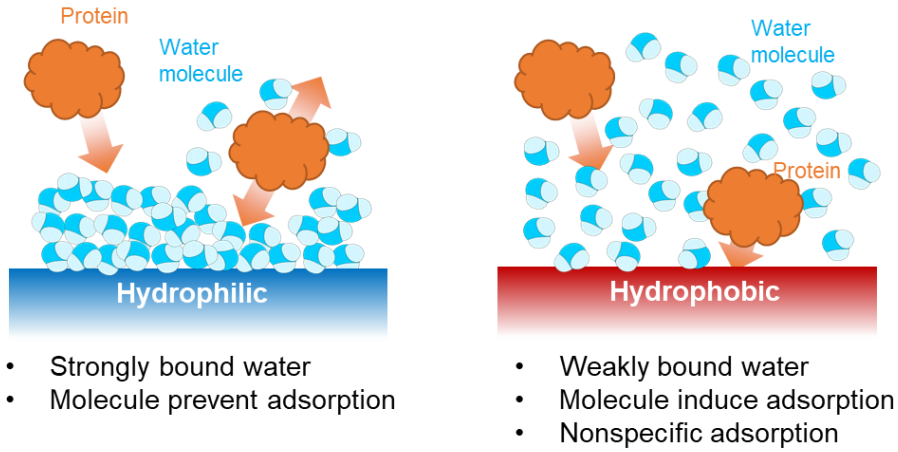

Figure 1.3. *Mechanism of protein adsorption due to hydrophobic interaction*

Protein adsorption is generally strongly driven by changes in entropy. The change in entropy can arise from the removal of water molecules from the surface of the absorbent to the bulk aqueous phase. Thus, the protein can be adsorbed on the adsorbent surface trough the dehydration force. In other words, surfaces that tend to have strongly bound water molecules (hydrophilic) require more enthalpy of dehydration to remove water molecules that allow the adsorption process to occur. Due to these reasons, in general, proteins tend to adsorb more readily to hydrophobic surfaces compared to hydrophilic ones (**Figure 1.3**). However, due to the highly

dehydrated hydrophobic surface, several proteins can be adsorbed simultaneously, which eventually resulting in non-specific adsorption. Indeed, the non-specific adsorption is undesirable for several applications due to its decreasing sensitivity, specificity, and reproducibility. Therefore, although a challenge remains to enhance the adsorption performance, material with the hydrophilic surface is more desirable due to several reasons: (1) the specific adsorption can be easily occurred by tuning the functionalization or nanostructure. (2) The hydrophilic surface has a more biocompatible attribute compared to the hydrophobic one [20]. (3) The majority of sustainable materials (e.g., natural polymers) have hydrophilic properties.

1.2.2 Effect of functionalization

The modification through surface chemical modification such as incorporating carboxylic acid (COOH) on the surface of the adsorbent or nanostructuring can be the appropriate strategies to address the challenge in making adsorbents with hydrophilic properties[21–25]. In an aqueous environment, proteins are generally electrically charged and surrounded by ions. The pH of the surrounding environment can influence the net charge of proteins through the acquisition or loss of protons, which makes the protein more positively or negatively charged. In acidic solutions, acidic functional groups are protonated and produce a positive charge (**Figure 1.4a)**. On the other hand, in alkaline solutions, negatively charged proteins are deprotonated from the functional groups of protein bases. Whereas at the isoelectric point, there is as much positive charge as the negative charge so that the net charge is zero, even though the high-charged fill remains on the surface of the protein. As illustrated in **Figure 1.4b**, the presence of the functional groups on the hydrophilic adsorbent can guide and generate more active sites by interaction with the functional groups (amino acid or carboxylic acid) of protein by electrostatic interaction or hydrogen bonding.

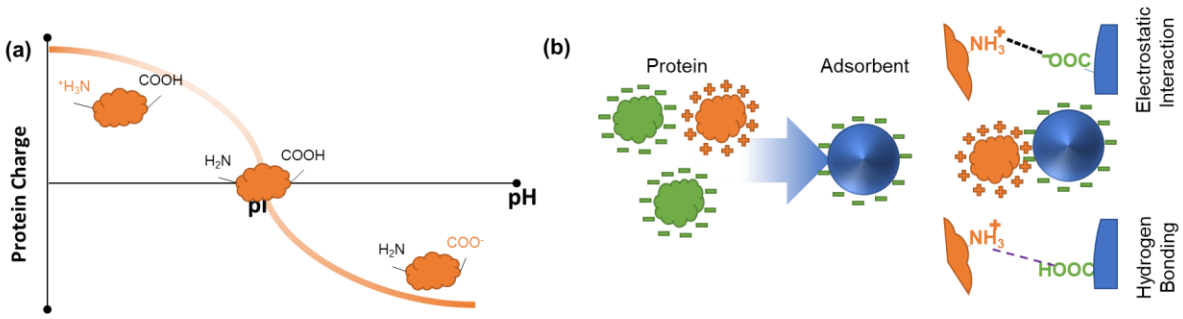

Figure 1.4 *(a) Isoelectric point of the protein. (b) Mechanism of protein adsorption due to the functionalized surface*

Surface functionalization is proven to enhance the adsorption ability of hydrophilic materials successfully. For example, Feng et al. enhanced the adsorption performance of ovalbumin and lysozyme by mixing the carboxymethyl chitosan with natural chitosan [26]. Meder et al. compared the effect of the functional group of amino, carboxyl, sulfonate, and phosphate groups and investigated their performance in adsorption of bovine serum albumin (BSA), lysozyme (Lyz) and trypsin (Try)[27]. The results show that electrostatic forces are the main driving force in protein–particle interaction. BSA that has a negative charge in neutral pH tends to be adsorbed to positively charge while Lys and Try, which negatively charged, tend to be adsorbed on negatively charged adsorbent particles. Therefore, the hydrophilic surface that has abundant functional groups and highly zeta potential will be highly desirable for efficient adsorption

1.2.3 Effect of nanostructure

Compared to a smooth surface or dense structures, nanostructured materials have been shown to have excellent biocompatibility properties due to increased interaction with proteins in the process of adsorption and conformation[28,29]. Nanostructure on particles leads to the presence of nano-roughness on the surface of the particles, which increases surface energy and ultimately drives to more significant protein adsorption[30]. Furthermore, the higher specific surface area owned by micro/nanostructured will provide much more adsorption sites for bioactive molecules. Inspired by this reason, the porous structure is the most attractive candidates for a wide range of applications in biomedical fields. The porous structure can increase the specific surface area and provide a proper interconnected channel that can enhance good penetration of fluids[31].

Another advantage of porous structures is that their pore size can be varied from micropores (<2 nm), mesopores (2-50 nm), and macropores (> 50 nm) according to the size of the protein to be absorbed. The appropriate pore size can undoubtedly bring many benefits in the process of adsorption and can control the penetration of selected protein into the porous structure (**Figure 1.5**). Deka et al. (2015) reported that besides the surface functionality, the adsorption of lysozyme was highly dependent on particle structural properties, such as pore size and pore volume [32]. Therefore, although some materials are naturally low affinity towards protein, various porous materials have hitherto been employed as protein adsorbents, such as mesoporous silica, porous carbons, porous resins, metal-organic frameworks, magnetic-based nanomaterials, and cellulose-based materials due to its ease of functionalization and ease of tuning the pore size [7,33–36]. However, the pore size of the materials, as mentioned above, is usually limited to the mesoporous range to yield a high specific surface area (SSA), large pore volume, controllable particle size, and excellent biocompatibility [37]. Unfortunately, this type of porosity has several limitations where diffusion plays a crucial function, especially for the adsorption of medium-large molecular-sized species [38]. Vinu et al. found that a longer time was required for lysozyme adsorption when the pore diameter was less than the molecular dimension of lysozyme [39]. It can be rationalized that adsorbing molecules have difficulty in reaching the available active sites in the mesoporous channel due to space limitations.

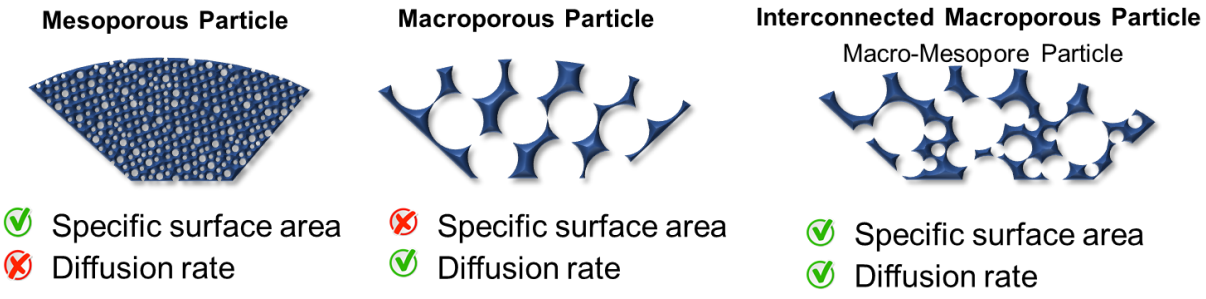

Figure 1.5. *Porous structure advantages in protein adsorption*

The previous researches then found that the diffusion problem can be solved by using a larger pore size where the pore size should be at least 2 times larger than the largest size of macromolecules. Therefore, the macroporous structure gives a promising superiority compared to the mesoporous structure, although consequently, it has a lower surface area. Suh as, the

macroporous structure offers a better permeability, better mass transfer diffusion, better intraparticle effective diffusivity, lower column backpressure, and more regular flow regime in static bed column [40–42]. Santos et al. studied the structure effect of SBA-15 for adsorption of biomolecules by different enlarged sizes of pores[43]. The results show that the modified SBA-15 with larger pore size shows a much higher adsorption capacity due to the shorter channel length, and good inter-particle channel formation. Sun et al. (2011) also show the advantages of the macroporous structure. They produced a porous monolith with two types of porous structures (mesoporous and macro-mesoporous) to adsorb two types of biomolecules with different molecule sizes [41]. The result shows that the presence of a macroporous structure successfully possesses higher adsorption capacity than that of the mesoporous silica materials.

Inspiring of the advantages of macroporous and mesoporous structure, macroporous particles with well-interconnected channels are significantly attractive both fundamentally and technologically. The interconnected channel could be producing a mesoporous area with sufficient exposed active surface in porous frameworks. The presence of macroporous as a gateway to the mesoporous area is an excellent strategy to provide efficient mass transportation with a rapid movement of large molecules throughout the framework. [44–47].

1.3. Synthesis of macroporous particle

By seeing the many advantages of macropore structure, the macroporous particles are rapidly becoming the material of choice in various industries and applications. Several routes to fabricate these materials were discovered. The summary of different methods for the synthesis of macroporous particles in the biomedical field is shown in **Table 1.1**.

1.3.1 Suspension polymerization method

This process typically uses the surfactant, monomer of the host material, and monomer of templating agents in the initial precursor solution. Initially, the surfactant is dissolved in water to make a micellar solution. The spherical micelle act as the template for the synthesis of spherical particles. After the stirring process, the monomer of the host, initiator, and monomer of the template was adsorbed inside of the micelle core[48]. Then, the polymerization reaction of the template particle occurs in-situ with host monomer material in the presence of an initiator. During the formation process, the two materials will interact, and self-assembly occurs in micelles core.

After completion of the reaction, the particles are separated and washed. Finally, the macroporous particles are obtained after removing the template by a heating or etching process. The advantage of this method is relatively easy and cheap because it is only used glassware in the manufacturing process. However, this process requires a lot of attention to get good reproducibility because the process is multiple steps with batch-to-batch synthesis routes. In addition, the resulted particles of <200 μm in size are generally produced in various sizes, depending on the precise control of the emulsification process and the resistance of the aggregation of droplets in the polymerization stage.

Table 1.1 *Synthesis method of macroporous particles*

Method	Particle size (μm)	Remarks	Schematic illustration
Suspension polymerization	5-10	Material : Polymer, silica Merit : Relatively easy Demerit : Multiple step (batch-to-batch synthesis routes), broad particle size distribution	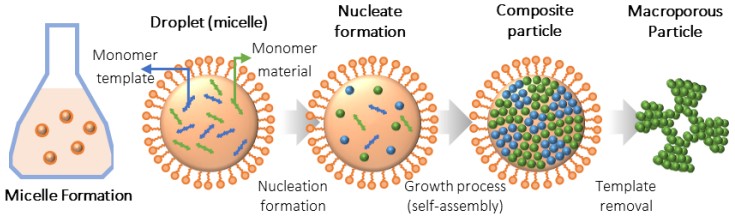
Seed swelling polymerization	0.5-200	Material : Polymer, resin Merit : Monodispersed particle, high porosity Demerit : Complicated, multiple steps, time consuming (10-12 hours)	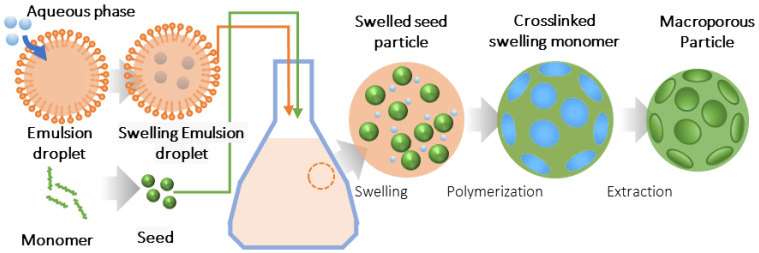
Microfluidics	10-1000	Material : Polymer Merit : Low reagent consumption, continuous route Demerit : Costly device, clogging and fouling	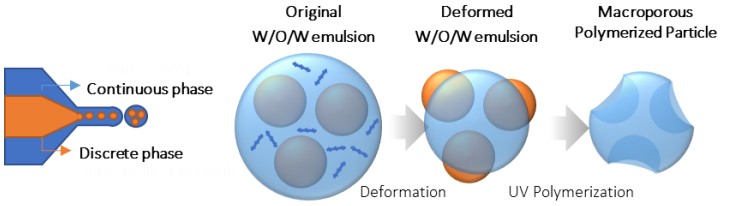
Spray process	0.5-20	Material : Polymer, resin, silica, carbon Merit : Easy, low reagent consumption, narrow pore size distribution Demerit : Selectivity to template	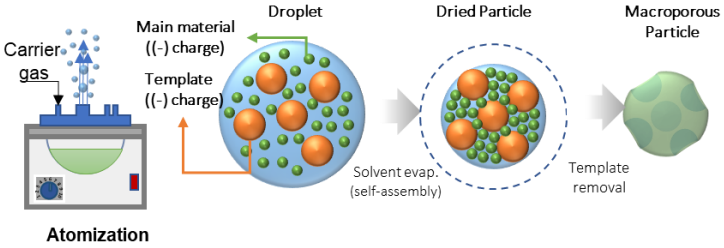

1.3.2 Seed swelling method

This method includes the formation of seed particles, the swelling process of porogens, the swelling process of monomer and a crosslinking agent, polymerization, and porogen removal by extraction [49]. At first, monodisperse seed particles were prepared in submicron size. In another place, swelling emulsion droplet that contained an aqueous phase, including activator, swelling agents, monomers, crosslinkers, initiators, and porogens, was prepared. Seed microspheres were then swelled with aqueous phase by dispersed aqueous phase emulsion droplet into seed particles. To produce a macroporous structure, porogens which usually is an organic solvent with a very good solvent to seed particle, inert, and easy to remove from the particle was needed [50]. After that, polymerization occurs in seed particles to form a network of polymers. Then, the monomer residue and porogens remain in the crosslinked polymer network were removed to produce a macroporous structure. As a result, the seed swelling polymerization method can render macroporous particles of <50 μm in size with high porosity and more narrow size distributions. Even so, this method is complicated and time-consuming because it consisted of multiple steps that required at least 10-12 hours for swelling and polymerization steps.

1.3.3 Microfluidic method

The microfluidic method was developed to overcome the complicated routes and abundant reagent consumption on conventional batch synthesis. With the microfluidic technique, a continuous process with a controllable parallel or sequential reaction was offered. As a result, the particle size polydispersity can be significantly reduced with low reagent consumption[48]. For manufacturing macropore particles, it can generally be classified by 4 methods: (1) simple polymerization with or without porogen, (2) phase emulsions as templates, (3) flow reactions under certain conditions, and (4) nano or micro-particle assembly [51]. This system generally involves at least two phases in the process where the inside phase (discrete phase) is a solvent that differs polarity from the outside aqueous phase (continuous phase). For example, the continuous phase is an aqueous solution, and the discrete phase is oil. Both of these phases are then infused at a flow rate which can be adjusted freely using the syringe pump connected to the device with the pipe. Continuous phase may contain monomers, polymers, or nanoparticles, which would later become the host material. The discrete phase is a solvent that can later be porogen or may also contain polymers, which will be the template. Then, the volatile phase is removed

beforehand. After that, the template is removed, and macropore particles are washed to remove residual residues [52]. However, microfluidic devices are generally costly with components consisting of slide glass, polyethylene or Teflon tubes, square glass capillaries, round glass capillaries, and syringe tips. Furthermore, the structure of the microreactor must be properly calculated because the size and shape of the microchannel greatly affect the droplet size and failure process, such as clogging and fouling.

1.3.4 Spray method

Another route is by using the spray method. The fabrication of macroporous particles by the spray method usually uses a combination of host and template particles. The pore size of the particles can be controlled by adjusting the size of the template. Initially, the precursors containing the host and template particles are sprayed and form a droplet to the hot gasses. Then, due to the influence of mechanical and electrical forces on the droplet, the template and the host will experience self-assembly and dry up to become the final product. The important point here is that a porous structure will form if the charges of host and template components are of the same sign of zeta potential [53]. Dried particles then have a macroporous structure by removing the template particle by heating or chemical etching.

Among the mentioned synthesis method, the spray process is considered to be a better method because it has many advantages such as easy to operate, simple, and produce a spherical particle with narrow particle size distribution. In addition, the spraying process can easily control the characteristics of the final product. By controlling the operating conditions of the drying process, we can get the shape, density, and morphology of the final product that we want. However, in the manufacture of macroporous particles with a spray process, we should take consideration in the selection of the appropriate template. Since the spray process usually suitable in the high production in industry, template selection should not only be focused on the controllable charge but also its economic point of view, such as cost-effective without reducing the specific surface area of the host material.

1.4. Cellulose nanofiber as advanced biopolymer in biomedical application

In recent years, the development of the production of cellulose nanofibers (CNF) has gained significant interest in the scientific and technological community[54]. CNF is a cellulose fiber that contained amorphous and crystalline regions in a nanoscale diameter and a length of a few micrometers. Due to these physical characteristics, CNF has many

advantages, such as high specific surfaces, excellent mechanical properties, and ease of being chemically modified. In addition, as cellulose is the most abundant renewable biomass in the world, CNF is a renewable material that is biodegradable and environmentally friendly. Compared to cellulose, CNFs have many unique properties such as high surface area, excellent stiffness, unique barrier, and optical properties, a lightweight, exceptional mechanical properties (high specific strength and modulus), high aspect ratio, environmental benefits, low coefficient of thermal expansion, and lowcost [55]. No wonder, CNF offered a massive versatility in many applications such as biomedical, environmental sciences, production of packaging, paper, electronics, and plastic composites.

The CNF production process consists of two steps, namely pretreatment and fibrillation. The pretreatment process can be based on chemical or enzymatic processes such as TEMPO-mediated oxidation, enzymatic hydrolysis, mechanical purification, acid hydrolysis, and carboxymethylation. Differences pretreatment processes generate differences in characteristics such as the morphology of generated CNF, mechanical properties, and optical properties. Thus, the expected characteristics can be adapted to various applications. From the CNF-pretreatments mentioned above, TEMPO-mediated oxidation is gaining interest due to their large specific surface, excellent mechanical properties, low weight, and the wide range of applications they can be used.

1.4.1 TEMPO Oxidized Cellulose Nanofiber (TOCN)

TEMPO-oxidized cellulose nanofibers (TOCN) was developed by Saito et al. [56,57]. They developed the system of oxidation of CNF with 2,2,6,6-tetramethylpiperidine -1-oxyl radical (TEMPO), hypochlorite, and bromide to convert the C6 primary hydroxyl group to a carboxylate group (**Figure 1.6 a**). As a result, TOCN possesses rich carboxylate groups without changing the original crystallinity or crystal width of wood celluloses. After the size reduction process, TOCN has a homogeneous shape with a width of 3-4 nm, and length 300 nm ~ ≥1μm (**Figure 1.6b**). Because TOCN has potential as an environmentally based raw nanomaterial, TOCN has attracted many researchers in the last decade (**Figure 1.7**).

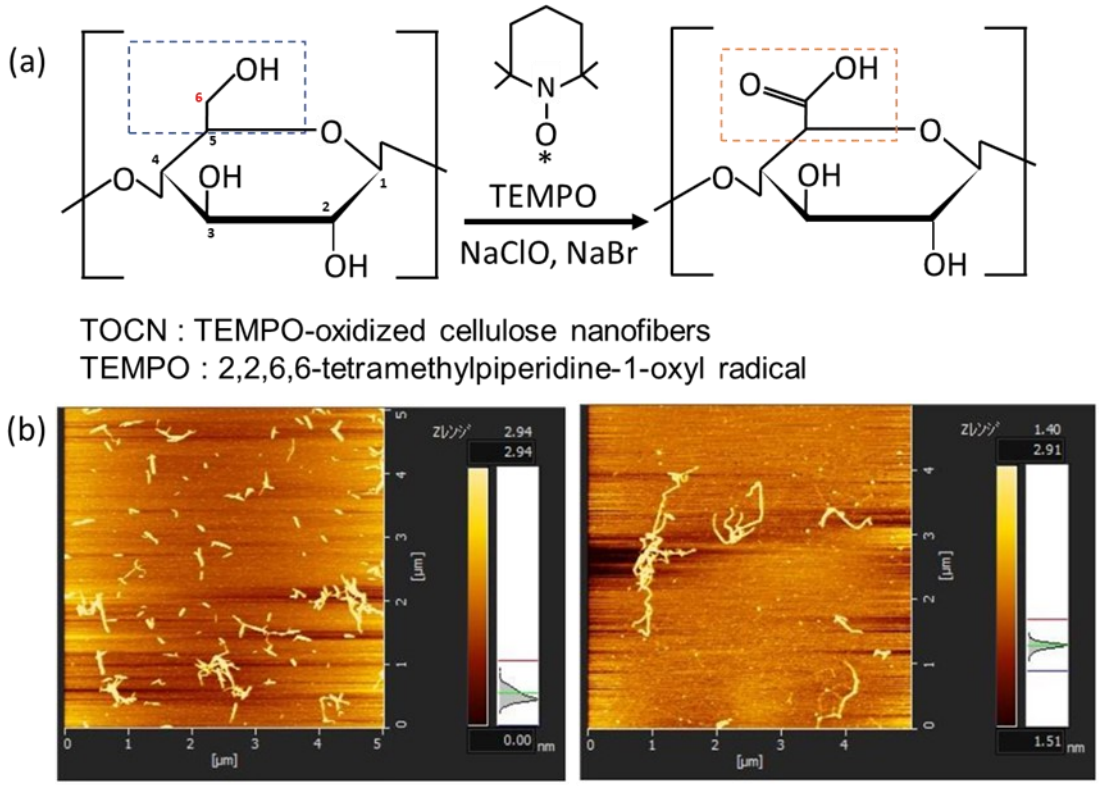

Figure 1.6 *(a) Synthesis of TOCN by oxidation of C6 primary hydroxyls to carboxylate groups and (b) Dynamic force microscopy image of CNF*

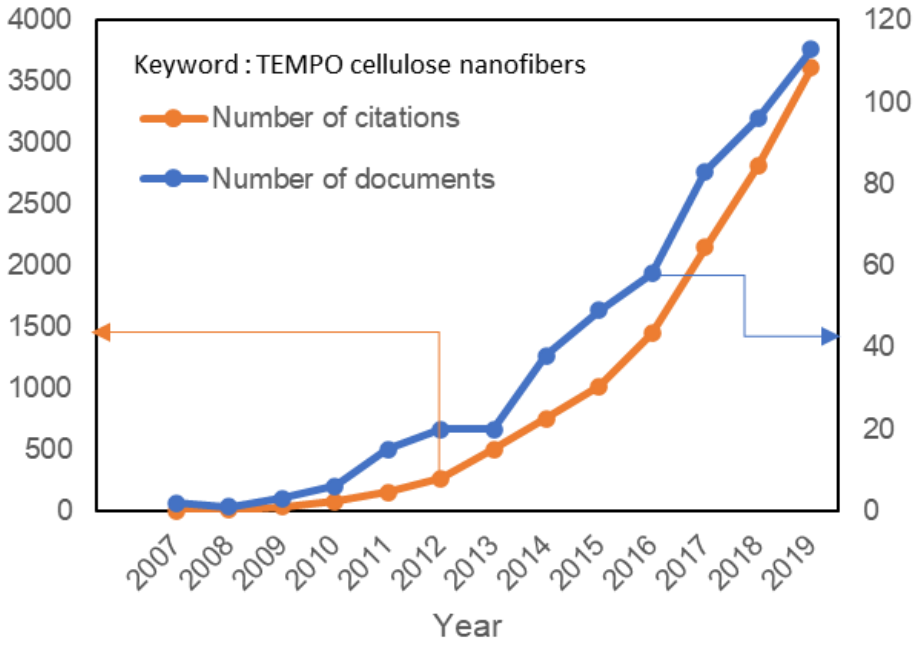

Figure 1.7*. The number of published and cited papers after the discovery of TOCN*

1.4.2 TEMPO Oxidized Cellulose Nanofiber (TOCN): Advantages and challenges

TOCN possesses rich carboxylate that resulted in electrostatic repulsion and osmotic effects working between anionically-charged TOCN in water. The zeta-potentials of which are approximately -75 mV in water, cause the formation of entirely individualized TOCN dispersed in water. The sizeable specific surface area of well-dispersed TOCN is 180 - 800 m^2/g depends on its width diameter[58,59]. With the abundant amount of carboxylate groups, TOCN is expected to exhibit a high affinity toward positively-charged compounds. Previous studies on TOCN showed significantly high adsorption for heavy metal ions, dye, and organic solvent (**Table 1.2**). The TOCN surface has carboxyl and hydroxyl groups that can coordinate effectively and capture heavy metal cations (Cu (II), Fe (II), Zn (II), As (III)), or different organic pollutants. However, in its practical application, TOCN faced some challenges: (1) If directly used as an individual TOCN in the adsorption process, then it will be difficult to be collected. (2) If used as nanostructures material or as composites, it is difficult to maintain its adequate dispersion.

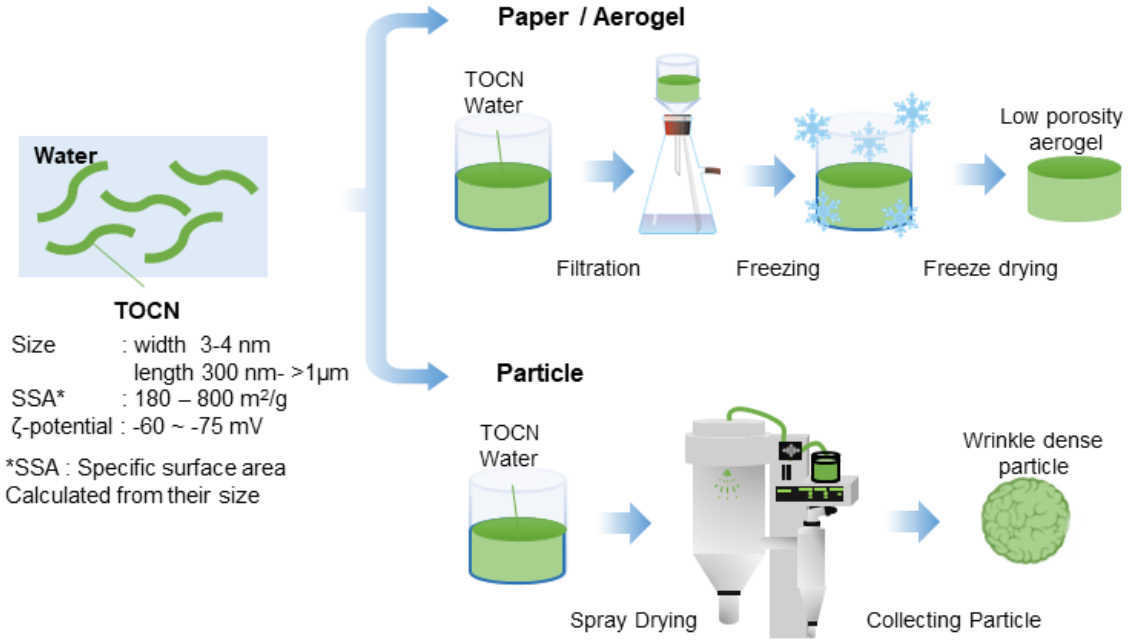

Figure 1.8 *Synthesis method of TOCN-based material.*

In the wet-state of TOCN, TOCN is completely individualized dispersed in water. Due to its great dispersibility, its specific surface area can reach 180 – 800 m^2/g depending on the width and length. However, in the preparation of nanostructure TOCN or its composite materials, it is difficult to maintain its adequate dispersion. Previously, several studies have been developed to fabricate TOCN-based materials, as illustrated in **Figure 1.8.**

As a result, TOCN is easily integrated and aggregated, which leads to dense structure, low specific surface area, low pore volume, and small pore size. The aggregation of TOCN occurred through losing repulsive forces *via* ionization of carboxyl groups or capillary effect shrinkage in a drying process at elevated temperatures. Therefore, although TOCN has a high possibility as a super adsorbent polymer, TOCN based material has limited to aerogel or nanofiber form (**Table 1.2**). In the preparation of TOCN-based aerogel, at first, the TOCN solution was prepared by dispersing in the water. The TOCN hydrogel was then prepared by filtering the solution using a Buchner funnel to remove excessed water, or adding the crosslinking agent such as polyamide (PEI) and $CaCl_2$ to increase their mechanical strength in acid condition [60]. TOCNs begin to lose their electric repulsion forces and combine each other in an acidic environment because the protonation of the carboxyl group initiated the formation of hydrogen bonds and integration between nanofibers. After that, the hydrogel was frozen and followed by freeze-drying to obtain aerogel [61].

So far, there is no research regarding the utilization of TOCN, especially in the particle form, as a protein adsorbent material. The manufacture of TOCN particles itself so far has only been utilized for hydrophobic coating materials by Zheng et al. (2019)[62]. They prepared a dried-state TOCN particle using a spray drying technique with the results show that a large amount of TOCN aggregates towards the droplet core with shrinkage during the rapid drying process, which leads to a dense morphology and wrinkle surface. Aggregation between CNF occurs through diffusion forces and hydrogen bond formation [63].

In summary, the particles and the aerogel based on TOCN materials were obtained with a specific surface area less than 20 m^2/g with pore size is less than 5 nm. This small pore size is certainly suitable for adsorption of ions and dye molecules, which usually have a size of <2 nm but will be a drawback for protein adsorption, which generally has a size > 4 nm and other macromolecules which have a larger size. In addition, unlike the other anionic polymers, TOCN has a very large molecular weight and insoluble in solvents such as water, although in acidic conditions. It certainly makes a significant challenge in the decoration of substrate material because its utilization is depending on the surface of the substrate.

Beyond the application as adsorbent materials, the utilization of TOCN in the biomedical field itself is just starting to be explored in 2015 by Weishaupt et al. [64]. They explained that TOCN has an interesting structure because it is easily recognized by the body.

At physiological pH, 90% by weight of TOCN can be easily removed from the body by dissolving in body fluids for 21 days. In 2017, Shefa et al. developed TOCN-silk fibroin scaffolds for wound healing application. The result revealed that TOCN-silk fibroin has good cell proliferation and attachment of L929 primary fibroblast cells. In vivo evaluation with rat skin showed that the TOCN-silk fibroin scaffolds promoted wound healing in the presence of biological markers [65]. In addition, TOCN also shows that they have long-term biocompatibility profile compared to CNC and CNF[66]. Due to these advantages, TOCN is believed to be a promising material as an effective adsorbent to specific protein considering their high content of carboxylate groups, negative charge, and good biocompatible.

***Table 1.2**. Application of TOCN as adsorbent*

TOCN as adsorbent			
Form	**Adsorbate**	**Remarks or composite with**	**Ref.**
Nanofiber	Cu (II), Zn (II), and.Paraquat cations	-	[67,68]
Carbon-aerogel	Oil and organic solvent	Carbonized TOCN aerogel	[69]
Hydrogel	Oil, As(III) and methylene blue (MB)	Composite to cationic guar gum or nanochitin	[69,70]
Aerogel	Phenol, Cu (II), As(III) and MB	Composite to PAE[a] TMPTAP[b] , PEI [c]. , and nanochitin as crosslinker	[60,70–72]
Paper filter	Cu (II) and brilliant blue dye	Composite with CNF and TiO_2	[73,74]

a Polyamide-epichlorohydrin
b Poly(hydroxyethylmethacyrlate-co-glycidylmethacryalte)
c Trimethylolpropane-tris-(2-methyl-1-aziridine) propionate

1.5. Objectives and outline of the dissertation

Bearing in mind the many applications that require particles for the process of protein adsorption, we aimed to synthesis of advanced adsorbent particles with the following features:

(1) Good mass transfer
(2) Excellent adsorption capacity
(3) Easy to be handling
(4) Highly biocompatible
(5) Highly reusability
(6) Based on sustainable materials

Therefore, in this dissertation, we prepared TOCN décorated macroporous silica particles through a spray process for protein adsorption applications to closely fulfill as mentioned characteristics. At first, the macroporous particle within micrometer-sized was prepared as supporting materials to fulfill the 1st and 3rd criteria. Second, TOCN was used to satisfy the rest characteristics. We expect the combination of macroporous particle and TOCN networks will generate abundant adsorption sites with highly open macro-mesoporous structures for the fast and high adsorption performance. Several parameters in the process of synthesis and adsorption performance have been carried out to investigate the effectiveness of the combination of TOCN and macropore particles on protein adsorption and to understand whether the driving factors in the adsorption process.

At first, we synthesize the micrometer-sized macroporous particles with template selection to get a cost-efficient template without decreases specific surface area, as described later in Chapter 2. Carbon materials were chosen as the host material in the initial process to compare the effectiveness of the polymer particle template. The synthesis of macroporous carbon particles was prepared through poly (methyl methacrylate) (PMMA) templating in the spray pyrolysis process. The concentration and particle size of PMMA were varied to evaluate the formation of porous structures, and its characteristics are then compared with those produced through polystyrene latex (PSL) templating.

Chapter 3 describes the synthesis of TOCN decorated macroporous SiO_2 (TOCN@macroporous SiO_2) particles and their protein adsorption performance. Macroporous silica particles were prepared from colloidal nanoparticles of silica to produce

macro-mesoporous particles via PMMA templating in the spray pyrolysis process. After that, TOCN was loaded on macroporous particles in a different weight ratio to understand how effective the combination of these two components as well as to obtain the optimum conditions for the adsorption.

In Chapter 4, the macropore size of silica particles was adjusted to understand how TOCN depositions decorate the macropore structure. The results show that the pore size corresponding to the length of TOCN can affect the deposition of TOCN either to the external surface or penetrate the pores. In addition, the adsorption kinetics, thermodynamics, and isothermal parameters studied to analyze the mechanism of protein adsorption.

General conclusions of all topics are listed in Chapter 5.

1.6. References

[1] P. Roach, D. Farrar, C.C. Perry, Interpretation of protein adsorption: Surface-induced conformational changes, J. Am. Chem. Soc. 127 (2005) 8168–8173.

[2] Q. Fu, Y. Si, C. Duan, Z. Yan, L. Liu, J. Yu, B. Ding, Highly carboxylated, cellular structured, and underwater superelastic nanofibrous aerogels for efficient protein separation, Adv. Funct. Mater. 29 (2019) 1808234.

[3] A. Jungbauer, Chromatographic media for bioseparation, J. Chromatogr. A. 1065 (2005) 3–12.

[4] K. Nakanishi, N. Tanaka, Sol-gel with phase separation. Hierarchically porous materials optimized for high-performance liquid chromatography separations, Acc. Chem. Res. 40 (2007) 863–873.

[5] G. Ahuja, K. Pathak, Porous carriers for controlled/modulated drug delivery, Indian J. Pharm. Sci. 71 (2009) 599

[6] M. Zhou, L. Shen, X. Lin, Y. Hong, Y. Feng, Design and pharmaceutical applications of porous particles, RSC Adv. 7 (2017) 39490-39501.

[7] S. Li, J.J. Mulloor, L. Wang, Y. Ji, C.J. Mulloor, M. Micic, J. Orbulescu, R.M. Leblanc, Strong and selective adsorption of lysozyme on graphene oxide, ACS Appl. Mater. Interfaces. 6 (2014) 5704–5712.

[8] N.I. Khan, A.G. Maddaus, E. Song, A low-cost inkjet-printed aptamer-based electrochemical biosensor for the selective detection of lysozyme, Biosensors. 8 (2018) 7.

[9] P. Subramanian, A. Lesniewski, I. Kaminska, A. Vlandas, A. Vasilescu, J. Niedziolka-Jonsson, E. Pichonat, H. Happy, R. Boukherroub, S. Szunerits, Lysozyme detection on aptamer functionalized graphene-coated SPR interfaces, Biosens. Bioelectron. 50 (2013) 239–243

[10] H.R. Culver, M.E. Wechsler, N.A. Peppas, Label-free detection of tear biomarkers using hydrogel-coated gold nanoshells in a localized surface plasmon resonance-based biosensor, ACS Nano. 12 (2018) 9342–9354

[11] M. Bonomini, Proteomics and protein adsorption on hemodialysis membranes, Proteomics - Clin. Appl. 11 (2017) 11-12.

[12] P. Łukasiak, J. Błażewicz, M. Miłostan, Some operations research methods for analyzing protein sequences and structures, Ann. Oper. Res. 175 (2010) 9–35.

[13] R. Latour, Biomaterials: Protein–surface interactions, In: Encycl. Biomater. Biomed. Eng. Second Ed. - Four Vol. Set, CRC Press, 2008: pp. 270–284.

[14] C.A. Haynes, W. Norde, Globular proteins at solid/liquid interfaces, Colloids Surfaces B Biointerfaces. 2 (1994) 517–566.

[15] W. Norde, Adsorption of proteins from solution at the solid-liquid interface, Adv. Colloid Interface Sci. 25 (1986) 267–340.

[16] D.R. Lu, S.J. Lee, K. Park, Calculation of solvation interaction energies for protein adsorption on polymer surfaces, J. Biomater. Sci. Polym. Ed. 3 (1992) 127–147.

[17] T. Kawai, K. Saito, W. Lee, Protein binding to polymer brush, based on ion-exchange, hydrophobic, and affinity interactions, J. Chromatogr. B. 790 (2003) 131–142.

[18] S. Patil, A. Sandberg, E. Heckert, W. Self, S. Seal, Protein adsorption and cellular uptake of cerium oxide nanoparticles as a function of zeta potential, Biomaterials. 28 (2007) 4600–4607.

[19] S. V. Patwardhan, F.S. Emami, R.J. Berry, S.E. Jones, R.R. Naik, O. Deschaume, H. Heinz, C.C. Perry, Chemistry of aqueous silica nanoparticle surfaces and the mechanism of selective peptide adsorption, J. Am. Chem. Soc. 134 (2012) 6244–6256.

[20] A. Hezi-Yamit, C. Sullivan, J. Wong, L. David, M. Chen, P. Cheng, D. Shumaker, J.N. Wilcox, K. Udipi, Impact of polymer hydrophilicity on biocompatibility: Implication for DES polymer design, J. Biomed. Mater. Res. Part A. 90A (2009) 133–141.

[21] B. Lee, Y. Kim, H. Lee, J. Yi, Synthesis of functionalized porous silicas via templating method as heavy metal ion adsorbents: The introduction of surface hydrophilicity onto the surface of adsorbents, Microporous Mesoporous Mater. 50 (2001) 77-90.

[22] A.S. Maria Chong, X.S. Zhao, Functionalized nanoporous silicas for the

immobilization of penicillin acylase, Appl. Surf. Sci. 237 (2004) 398–404.

[23] A. Maria Chong, X. Zhao, A.T. Kustedjo, S. Qiao, Functionalization of large-pore mesoporous silicas with organosilanes by direct synthesis, Microporous Mesoporous Mater. 72 (2004) 33–42.

[24] G. Bayramoglu, V.C. Ozalp, M. Yilmaz, U. Guler, B. Salih, M.Y. Arica, Lysozyme specific aptamer immobilized MCM-41 silicate for single-step purification and quartz crystal microbalance (QCM)-based determination of lysozyme from chicken egg white, Microporous Mesoporous Mater. 207 (2015) 95-104.

[25] Z. Yan, S. Tao, J. Yin, G. Li, Mesoporous silicas functionalized with a high density of carboxylate groups as efficient absorbents for the removal of basic dyestuffs, J. Mater. Chem. 16 (2006) 2347-2353.

[26] Z. Feng, Z. Shao, J. Yao, Y. Huang, X. Chen, Protein adsorption and separation with chitosan-based amphoteric membranes, Polymer (Guildf). 50 (2009) 1257–1263.

[27] F. Meder, T. Daberkow, L. Treccani, M. Wilhelm, M. Schowalter, A. Rosenauer, L. Mädler, K. Rezwan, Protein adsorption on colloidal alumina particles functionalized with amino, carboxyl, sulfonate and phosphate groups, Acta Biomater. 8 (2012) 1221–1229.

[28] K.M. Woo, V.J. Chen, P.X. Ma, Nano-fibrous scaffolding architecture selectively enhances protein adsorption contributing to cell attachment, J. Biomed. Mater. Res. 67A (2003) 531–537.

[29] D. Khang, S.Y. Kim, P. Liu-Snyder, G.T.R. Palmore, S.M. Durbin, T.J. Webster, Enhanced fibronectin adsorption on carbon nanotube/poly(carbonate) urethane: Independent role of surface nano-roughness and associated surface energy, Biomaterials. 28 (2007) 4756–4768.

[30] S.D. Puckett, E. Taylor, T. Raimondo, T.J. Webster, The relationship between the nanostructure of titanium surfaces and bacterial attachment, Biomaterials. 31 (2010) 706-713.

[31] A. Barhoum, M. Bechelany, A.S.H. Makhlouf, eds., Handbook of Nanofibers, Springer International Publishing, Cham, 2019.

[32] J.R. Deka, D. Saikia, Y.S. Lai, C.H. Tsai, W.C. Chang, H.M. Kao, Roles of nanostructures and carboxylic acid functionalization of ordered cubic mesoporous silicas in lysozyme immobilization, Microporous Mesoporous Mater. 213 (2015) 150–160.

[33] P.-F. Guo, X.-M. Wang, X.-W. Chen, T. Yang, M.-L. Chen, J.-H. Wang, Nanostructures serve as adsorbents for the selective separation/enrichment of proteins, TrAC Trends Anal. Chem. 120 (2019) 115650.

[34] D. Saikia, J.R. Deka, C.E. Wu, Y.C. Yang, H.M. Kao, pH responsive selective protein

adsorption by carboxylic acid functionalized large pore mesoporous silica nanoparticles SBA-1, Mater. Sci. Eng. C. 94 (2019) 344–356.

[35] S. Lombardo, W. Thielemans, Thermodynamics of adsorption on nanocellulose surfaces, cellulose. 26 (2019) 249–279.

[36] K. Salimi, D.D. Usta, İ. Koçer, E. Çelik, A. Tuncel, Protein A and protein A/G coupled magnetic SiO2 microspheres for affinity purification of immunoglobulin G, Int. J. Biol. Macromol. 111 (2018) 178–185.

[37] S.A. Jadhav, Incredible pace of research on mesoporous silica nanoparticles, Inorg. Chem. Front. 1 (2014) 735–739.

[38] E. Serra, Á. Mayoral, Y. Sakamoto, R.M. Blanco, I. Díaz, Immobilization of lipase in ordered mesoporous materials: Effect of textural and structural parameters, Microporous Mesoporous Mater. 114 (2008) 201–213.

[39] A. Vinu, N. Gokulakrishnan, V. V. Balasubramanian, S. Alam, M.P. Kapoor, K. Ariga, T. Mori, Three-dimensional ultralarge-pore Ia3d mesoporous silica with various pore diameters and their application in biomolecule immobilization, Chem. - A Eur. J. 14 (2008) 11529–11538.

[40] T. Çamli, M. Tuncel, S. Şenel, A. Tuncel, Functional, uniform, and macroporous latex particles: Preparation, electron microscopic characterization, and non-specific protein adsorption properties, J. Appl. Polym. Sci. 84 (2002) 414–429.

[41] Z. Sun, Y. Deng, J. Wei, D. Gu, B. Tu, D. Zhao, Hierarchically ordered macro-/mesoporous silica monolith: Tuning macropore entrance size for size-selective adsorption of proteins, Chem. Mater. 23 (2011) 2176–2184.

[42] Y. Tao, E.X.P. Almodovar, G. Carta, G. Ferreira, D. Robbins, Adsorption kinetics of deamidated antibody variants on macroporous and dextran-grafted cation exchangers. III. Microscopic studies, J. Chromatogr. A. 1218 (2011) 8027-8035.

[43] S.M.L. Santos, J.A. Cecilia, E. Vilarrasa-García, I.J. Silva Junior, E. Rodríguez-Castellón, D.C.S. Azevedo, The effect of structure modifying agents in the SBA-15 for its application in the biomolecules adsorption, Microporous Mesoporous Mater. 232 (2016) 53-64.

[44] H. Hong, J. Liu, H. Huang, C. Atangana Etogo, X. Yang, B. Guan, L. Zhang, Ordered macro–microporous metal–organic framework single crystals and their derivatives for rechargeable aluminum-ion batteries, J. Am. Chem. Soc. 141 (2019) 14764–14771.

[45] R. Balgis, W. Widiyastuti, T. Ogi, K. Okuyama, Enhanced electrocatalytic activity of Pt/3D hierarchical bimodal macroporous carbon nanospheres, ACS Appl. Mater. Interfaces. 9 (2017) 23792–23799.

[46] F. Iskandar, A.B.D. Nandiyanto, K.M. Yun, C.J. Hogan, K. Okuyama, P. Biswas,

Enhanced photocatalytic performance of brookite TiO_2 macroporous particles prepared by spray drying with colloidal templating, Adv. Mater. 19 (2007) 1408–1412.

[47] A.B.D. Nandiyanto, O. Arutanti, T. Ogi, F. Iskandar, T.O. Kim, K. Okuyama, Synthesis of spherical macroporous WO_3 particles and their high photocatalytic performance, Chem. Eng. Sci. 101 (2013) 523–532.

[48] D. Ghosh Dastidar, S. Saha, M. Chowdhury, Porous microspheres: Synthesis, characterisation and applications in pharmaceutical & medical fields, Int. J. Pharm. 548 (2018) 34-48.

[49] B. Yu, T. Xu, H. Cong, Q. Peng, M. Usman, Preparation of porous poly(styrene-divinylbenzene) microspheres and their modification with diazoresin for mix-mode HPLC separations, Materials (Basel). 10 (2017) 440

[50] B. Yu, T. Xue, L. Pang, X. Zhang, Y. Shen, H. Cong, the effect of different porogens on porous PMMA microspheres by seed swelling polymerization and its application in high-performance liquid chromatography, Materials (Basel). 11 (2018) 705.

[51] B. Wang, P. Prinsen, H. Wang, Z. Bai, H. Wang, R. Luque, J. Xuan, Macroporous materials: Microfluidic fabrication, functionalization and applications, Chem. Soc. Rev. 46 (2017) 855-914.

[52] W.J. Duncanson, T. Lin, A.R. Abate, S. Seiffert, R.K. Shah, D.A. Weitz, Microfluidic synthesis of advanced microparticles for encapsulation and controlled release, Lab Chip. 12 (2012) 2135.

[53] R. Balgis, S. Sago, G.M. Anilkumar, T. Ogi, K. Okuyama, Self-Organized Macroporous Carbon Structure Derived from Phenolic Resin via Spray Pyrolysis for High-Performance Electrocatalyst, ACS Appl. Mater. Interfaces. 5 (2013) 11944–11950.

[54] J. Patiño-Masó, F. Serra-Parareda, Q. Tarrés, P. Mutjé, F.X. Espinach, M. Delgado-Aguilar, TEMPO-oxidized cellulose nanofibers: A potential bio-based superabsorbent for diaper production, Nanomaterials. 9 (2019) 1271.

[55] A. Tejado, M.N. Alam, M. Antal, H. Yang, T.G.M. van de Ven, Energy requirements for the disintegration of cellulose fibers into cellulose nanofibers, cellulose. 19 (2012) 831-842.

[56] T. Saito, A. Isogai, TEMPO-mediated oxidation of native cellulose. The effect of oxidation conditions on chemical and crystal structures of the water-insoluble fractions, Biomacromolecules. 5 (2004) 1983–1989.

[57] T. Saito, Y. Nishiyama, J.L. Putaux, M. Vignon, A. Isogai, Homogeneous suspensions of individualized microfibrils from TEMPO-catalyzed oxidation of native cellulose, Biomacromolecules. 7 (2006) 1687–1691.

[58] Y.B. Pottathara, V.N. Narwade, K.A. Bogle, V. Kokol, TEMPO-oxidized cellulose nanofibrils–graphene oxide composite films with improved dye adsorption properties, Polym. Bull. (2019).

[59] P. Liu, K. Oksman, A.P. Mathew, Surface adsorption and self-assembly of Cu(II) ions on TEMPO-oxidized cellulose nanofibers in aqueous media, J. Colloid Interface Sci. 464 (2016) 175–182.

[60] W. Yang, H. Bian, L. Jiao, W. Wu, Y. Deng, H. Dai, High wet-strength, thermally stable and transparent TEMPO-oxidized cellulose nanofibril film via crosslinking with poly-amide epichlorohydrin resin, RSC Adv. 7 (2017) 31567–31573.

[61] L. Qin, X. Zhao, Y. He, H. Wang, H. Wei, Q. Zhu, T. Zhang, Y. Qin, A. Du, Preparation, Characterization, and In Vitro Evaluation of Resveratrol-Loaded Cellulose Aerogel, Materials (Basel). 13 (2020) 1624.

[62] X. Zheng, S. Fu, Reconstructing micro/nano hierarchical structures particle with nanocellulose for superhydrophobic coatings, Colloids Surfaces A Physicochem. Eng. Asp. 560 (2019) 171–179.

[63] Y. Peng, D.J. Gardner, Y. Han, Drying cellulose nanofibrils: in search of a suitable method, cellulose. 19 (2012) 91–102.

[64] R. Weishaupt, G. Siqueira, M. Schubert, P. Tingaut, K. Maniura-Weber, T. Zimmermann, L. Thöny-Meyer, G. Faccio, J. Ihssen, TEMPO-oxidized nanofibrillated cellulose as a high density carrier for bioactive molecules, Biomacromolecules. 16 (2015) 3640–3650.

[65] A.A. Shefa, J. Amirian, H.J. Kang, S.H. Bae, H.-I. Jung, H. Choi, S.Y. Lee, B.-T. Lee, In vitro and in vivo evaluation of effectiveness of a novel TEMPO-oxidized cellulose nanofiber-silk fibroin scaffold in wound healing, Carbohydr. Polym. 177 (2017) 284–296.

[66] H. Van Ho, P. Makkar, A.R. Padalhin, T.T.T. Le, S.Y. Lee, G. Jaegyoung, B.T. Lee, Preliminary studies on the in vivo performance of various kinds of nanocellulose for biomedical applications, J. Biomater. Appl. 34 (2020) 942-951.

[67] M. Li, S.A. Messele, Y. Boluk, M. Gamal El-Din, Isolated cellulose nanofibers for Cu (II) and Zn (II) removal: performance and mechanisms, Carbohydr. Polym. 221 (2019) 231–241.

[68] C.-F. Huang, C.-W. Tu, R.-H. Lee, C.-H. Yang, W.-C. Hung, K.-Y. Andrew Lin, Study of various diameter and functionality of TEMPO-oxidized cellulose nanofibers on paraquat adsorptions, Polym. Degrad. Stab. 161 (2019) 206–212.

[69] L. Dai, T. Cheng, X. Xi, S. Nie, H. Ke, Y. Liu, S. Tong, Z. Chen, A versatile TOCN/CGG self-assembling hydrogel for integrated wastewater treatment, cellulose. 27 (2020) 915–925.

[70] X. Zhang, I. Elsayed, C. Navarathna, G.T. Schueneman, E.B. Hassan, Biohybrid Hydrogel and Aerogel from Self-Assembled Nanocellulose and Nanochitin as a High-Efficiency Adsorbent for Water Purification, ACS Appl. Mater. Interfaces. 11 (2019) 46714–46725.

[71] L. Mo, H. Pang, Y. Tan, S. Zhang, J. Li, 3D multi-wall perforated nanocellulose-based polyethylenimine aerogels for ultrahigh efficient and reversible removal of Cu(II) ions from water, Chem. Eng. J. 378 (2019) 122157.

[72] N. Zhang, G.-L. Zang, C. Shi, H.-Q. Yu, G.-P. Sheng, A novel adsorbent TEMPO-mediated oxidized cellulose nanofibrils modified with PEI: Preparation, characterization, and application for Cu(II) removal, J. Hazard. Mater. 316 (2016) 11–18.

[73] Z.A. Al-Ahmed, A.A. Hassan, S.M. El-Khouly, S.E. El-Shafey, TEMPO-oxidized cellulose nanofibers/TiO_2 nanocomposite as new adsorbent for Brilliant Blue dye removal, Polym. Bull. (2019).

[74] Mautner, Y. Kwaw, K. Weiland, M. Mvubu, A. Botha, M.J. John, A. Mtibe, G. Siqueira, A. Bismarck, Natural fibre-nanocellulose composite filters for the removal of heavy metal ions from water, Ind. Crops Prod. 133 (2019) 325–332.

Chapter 2

Preparation of macroporous particles via PMMA templating in spray pyrolysis

2.1 Introduction

The precise control of porous structures has increasingly attracted the attention of researchers in past decades.[1–3] Porous materials have unique properties that are anticipated to be useful for many applications such as adsorption and separation, electrodes of Li ion batteries, drug delivery, and catalysis.[4–12] The templating method has been widely used for the production of porous particles.[13] This method enables easy control of the pore size and pore structure depending on the characteristics of the used template. However, template selection is a critical factor in the production of porous particles. The chosen template should not only enable the formation of the desired pore structure with ordered porous structure but also be economical and support a green production process.

Our group has reported investigations on the synthesis of porous particles using polystyrene latex (PSL) as the template through a spray pyrolysis process.[14–17] PSL is versatile and has been proven to be effective for the synthesis of various nanostructured particles, especially macroporous and hollow structured particles.[17–20] Although PSL decomposes at elevated temperatures, the removal of PSL by thermal decomposition leaves a residue of approximately 22.4% of its initial weight.[21] This residue is unfavourable for the production of nanostructured particles, as it potentially blocks the formation of micropores and mesopores. The disappearance of micropores and mesopores decreases the surface area, which constricts the performance of macroprous particles in its application. In addition, this residue leads to the drawback of a decrease of the material purity. Therefore, it is highly desirable to synthesize a macroporous particle that is template residue free and has a high surface area with an appropriate template selection.

A promising alternative template is poly(methyl methacrylate) (PMMA). PMMA is as versatile as PSL, with at least two advantages that distinguish it from PSL. First, the decomposition temperature of PSL is higher than that of PMMA, which allows for a complete decomposition of PMMA in a process involving a rapid reaction, such as spray pyrolysis. Second, there is a low residual amount after a complete decomposition. PMMA

can maintain a high surface area because the low amount of residue will not block the micropore and mesopore formation. In addition to these advantages, which are attributed to its chemical characteristics, PMMA offers a significant economic advantage owing to its economical price. PMMA is cost-effective, which will potentially be more profitable on the industrial scale.[22]

Thus, in this chapter, macroporous carbon particles were chosen to be prepared to systemically observe the advantages of another template selection in preparation of ordered macroporous particles. Since macroporous carbon possess high amount of micro-mesoporous structure, the effect of residual template will clearly affect the interconnected channel and surface area of this material. Although PMMA has been used for films, monoliths, and foam materials preparation, there have been no reports on the synthesis of porous particles, especially carbon particles, using PMMA as the template in a spray pyrolysis process.[2,6,7,12,21,23,24]. Hence, we aimed the production of ordered macroporous structure of carbon particles with relative-exceptionally high surface area using PMMA as the template through a one-pot facile spray pyrolysis process. In addition, energy consumption for template decomposition and the properties of macoporous carbon particle obtained using a PMMA template was compared to that using PSL template with same carbon precursor, that is, a phenolic resin.

2.2 Experimental

2.2.1. Synthesis of Macroporous Carbon Particles.

Macroporous carbon particles were produced by an aqueous precursor solution containing phenolic resin (PR, 50 wt.%, Sumitomo Bakelite Co., Ltd., Tokyo, Japan) as the carbon source, polymethyl methacrylate (PMMA, Sekisui Plastics Co., Ltd., Tokyo, Japan) as the template and ultrapure water as the dispersant media. The concentration of PR in the precursor was set as high as 0.25 wt.%. Three sizes of PMMA particles (PMMA (A): 108 nm, PMMA (B): 306 nm, and PMMA (C): 503 nm) were used in this study. PMMA was used in various weight ratios of 6, 7, and 8 to PR. The aqueous precursor was then sonicated by an ultrasonic device (IKA, T 10 basic ULTRA-TURRAX S004) with a speed rotation of 25 600 rpm for 1 h to ensure dispersion of PMMA. Then, the precursor was put into an ultrasonic nebulizer (0.8 MHz, NE-U17, Omron Healthcare Co., Ltd., Kyoto, Japan) with a circulation system. The precursor was sprayed through a tubular furnace with four stacked temperature zones set to 150, 350, 1000, and 1000 °C. The produced particles were collected by filter paper that was placed on the top of the furnace using N_2 gas (0.8 L/min). The filter

was maintained at 150 °C to avoid water condensation. Details of the spray pyrolysis experiment setup is shown in **Figure 2.1**.

2.2.2. Characterization.

Scanning electron microscopy (SEM) (S-5000, Hitachi Ltd., Tokyo, Japan) and transmission electron microscopy (TEM; JEM-2010, 200 kV, JEOL, Tokyo, Japan) were used to investigate the morphologies of the products. Dynamic light scattering (DLS) with a ZS nanoanalyzer (Malvern Instrument Inc., London, U.K.) was used to examine the size distribution and zeta (ζ) potential of the PMMA particles. Thermogravimetric analysis (TGA-50/50H, Shimadzu Corp., Kyoto, Japan) was used to determine the temperature for the PMMA removal. The surface areas were determined quantitatively by N_2 adsorption-desorption (BELSORP-max, BEL Japan, Osaka, Japan) using the Brunauer-Emmett-Teller (BET) method, the pore distribution was determined by the Barrett-Joyner Halenda (BJH) method, and the size of micropore was determined by the Horvath-Kawazoe method.

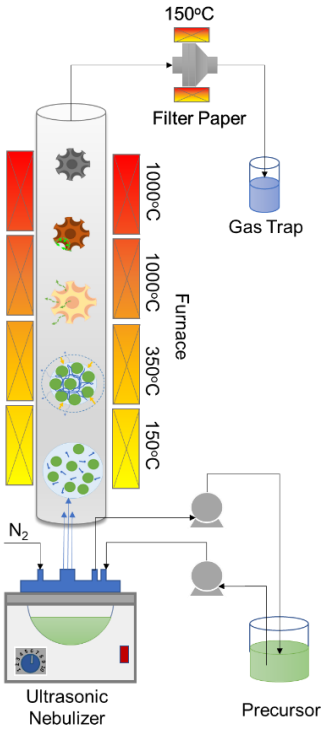

***Figure 2.1**. Schematic diagram of experimental apparatus*

2.3 Results and Discussion

2.3.1 Synthesis of macroporous carbon particles using PMMA template particles

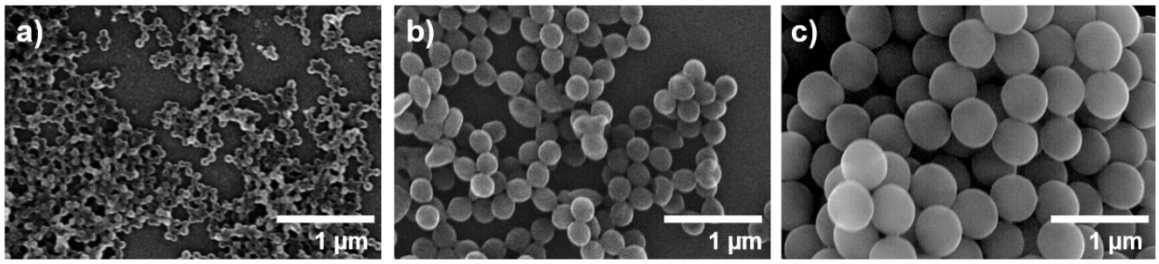

Figure 2.2. *SEM image of a) PMMA (A); b) PMMA (B); and c) PMMA (C)*

Figure 2.2 shows SEM images of the three sizes of PMMA particles used in this study. All PMMA particles exhibited a spherical shape. The sizes and ζ potentials of the PMMA particles are shown in **Table 2.1**. The average sizes of the PMMA particles were 108, 305, and 503 nm for PMMA(A), PMMA(B), and PMMA(C), respectively. As shown in **Table 2.1**, the deviation percentage (σ) of the particle size was below 5%, which meant a uniform size. Considering that the pore size of the final carbon product is highly dependent on the template size, the uniformity of PMMA becomes important. The uniform size of PMMA particles also indicated a good dispersion in the precursor system. PMMA(A), PMMA(B), and PMMA(C) each had a negative charge, that is, -34, -24, and -39 mV, respectively. As reported previously,[14,15] a negatively charged template will produce porous carbon particles in a spray pyrolysis system with PR as the carbon source. The negative charge of the precursors causes both sets of particles to repel each other and leads them to be independently distributed in the droplet.[16]

Table 2.1. *Size and zeta potential of the PMMA particles and PR*

Precursor Name	Diameter (nm) ± σ (%)	Zeta Potential (mV)
PMMA (A)	108 ± 4.2	-34
PMMA (B)	306 ± 3.4	-24
PMMA (C)	503 ± 1.9	-39
PR	-	-40

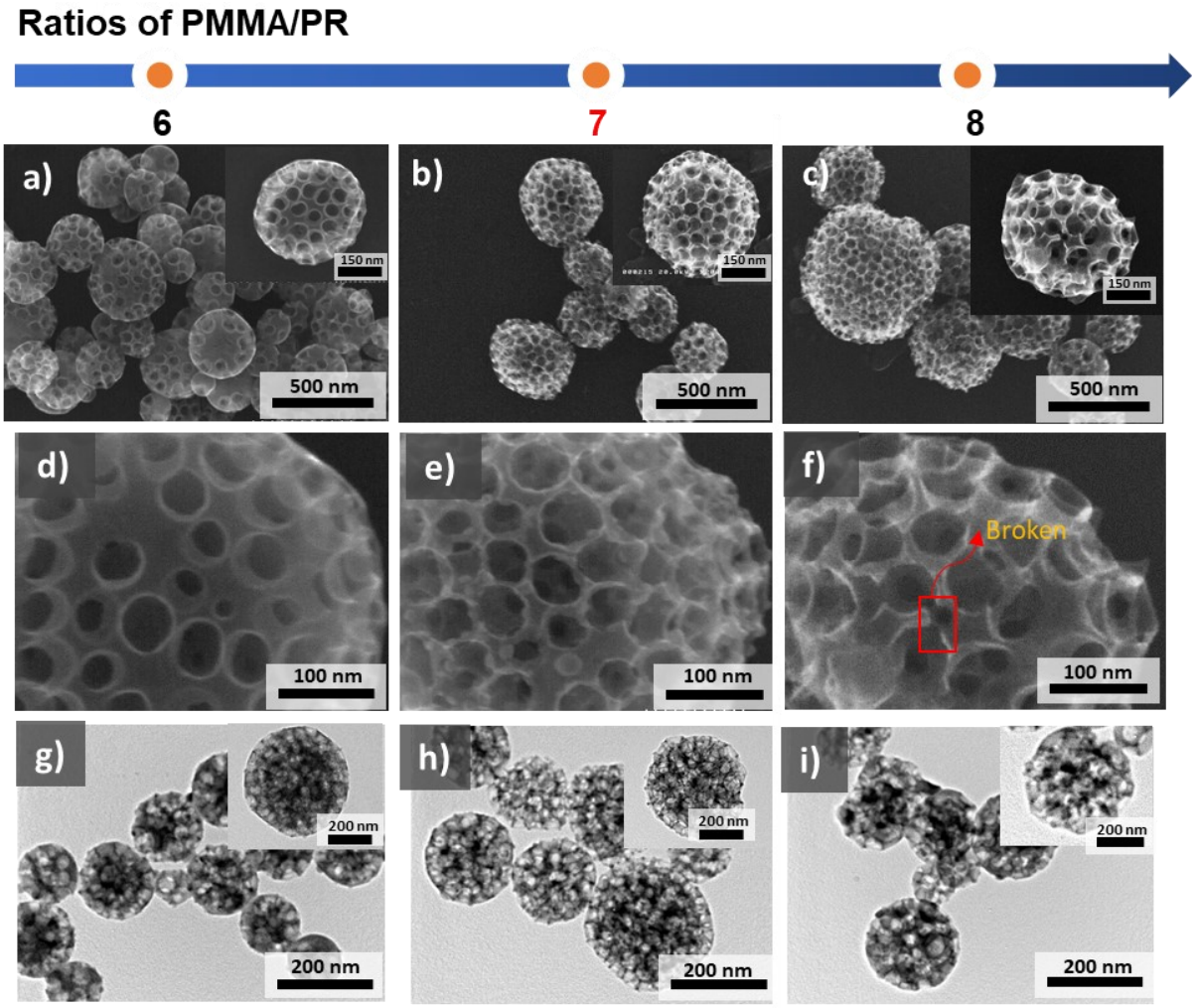

Figure 2.3. *SEM analysis of porous carbon particles with various ratios of PMMA/PR: a, d) 6; b, e) 7; c, f) 8; TEM images of carbon particles prepared using various ratios of PMMA/PR: g) 6; h) 7; i) 8;*

At first, the ratio of PMMA/PR was varied to control the porous structure (**Figure 2.3**). The morphology results of the PMMA/ PR ratios of 6-8 are shown in **Figure 2.3a-f**. By increasing the PMMA/PR ratio, the structures of carbon particles gradually changed, as shown in detail in **Figure 2.3d-f**. At a low PMMA/PR ratio, the pores formed only on the surface of the particle (**Figure 2.3d**). Increasing the PMMA concentration increased the number of templates in the droplet which later transformed into pores. The pores were not only present on the surface, but also inside the particle (**Figure 2.3e and f**). This phenomenon was caused by the self-assembly of the precursor in the droplet. When the droplets shrank isotropically, the temperature gradient between the droplet center and surface during droplet evaporation triggered the PMMA particles to move toward the droplet surface and be stabilized thereon.[25] Therefore, PMMA particles tended to assemble only on the surface at a low PMMA concentration. When the PMMA concentration was increased, the number

of PMMA particles in the droplets increased. Owing to the space constraint on the surface, some of the PMMA particles filled the inner layer toward the droplet core. The TEM images in **Figure 2.3g-i** confirmed that the addition of PMMA led to the formation of highly ordered porous structures inside the porous carbon particle. In addition to increasing the number of pores, the skeleton size decreased. When the number of templates in the droplet was above some critical value, the space between template particles became frustrated, which led to a collapse. In this research, the porous carbon particle started to collapse when the mass ratio of PMMA/PR reached 8 and was entirely broken when the ratio was further increased to 16.

After that, PMMA/PR ratio 6 was chosen as the condition to investigate the effect of different size of PMMA particles **(Figure 2.4a-c)**. Overall, the carbon particle was spherical in shape with a porous morphology. The TEM and SEM images revealed the porous structure on the surface of and inside the carbon particle. This morphology was similar to the results from our previous works which used PSL particles as the template.[10,14–16] Increasing the size of the template increased the pore size but decreased the number of pores. Even so, as indicated in **Figure 2.4**, the average pore sizes were different from the sizes of the PMMA particles. The average pore sizes using PMMA(A), PMMA(B), and PMMA(C) were 55, 194, and 370 nm, which implied a shrinkage from the initial size of PMMA by 45, 35, and 26%, respectively.

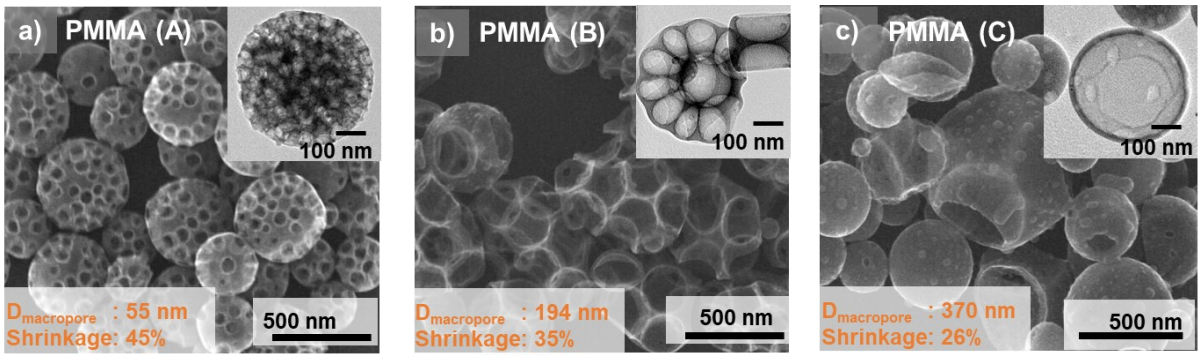

Figure 2.4. *SEM and TEM images of porous carbon particles prepared using a) PMMA (A); b) PMMA (B); c) PMMA (C) at ratio of PMMA/PR is 6 with same mass concentration of PR and PMMA. d) Average pore size of porous carbon particles by different size of PMMA.*

2.3.2 Comparison of macroporous carbon particles via PMMA and PSL templating

PMMA particles were used in this study due to their earlier decomposition compared to PSL. Thus, to investigate the characteristics of PMMA and to determine the reaction temperature of the furnace in the pyrolysis process, thermogravimetric analysis (TGA) was conducted on the samples of PR, PMMA, and the PR-PMMA blend with a mass ratio of 1:6 (**Figure 2.5a**). The starting material for the TG analysis, of which the result is provided in

Figure 2.5a, was prepared via spray drying in 180 °C to promote self-assembly. Therefore, the results of TG analysis could closely represent the actual condition in the spray pyrolysis process. In the PR curve, the PR lost its weight owing to the decomposition which released various gases (CO, CO_2, CH_4, H_2 and H_2O)[26] as shown in the steep slope in the temperature range 20-500 °C. After that, the weight of PR became relatively stable, as shown by the gentle slope, because carbonization had already started.[10]

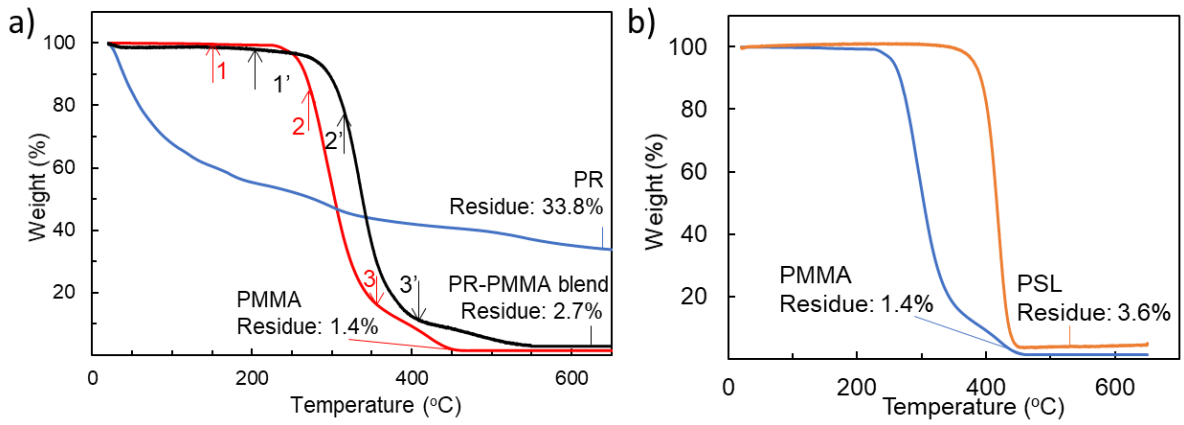

Figure 2.5. *a) TGA thermogram of PR; PMMA; and PR-PMMA blend in N_2 atmosphere with heating rate 10°C/min. b) TGA thermogram of PMMA and PSL*

Previously, Malhotra et al. explained that longer PMMA chains depolymerize first at low temperatures, followed by the shorter chains at higher temperature.[27] Recent research has divided the decomposition of PMMA into steps. According to the TGA curve of PMMA samples (**Figure 2.5a**, red curve), there are three steps in the weight loss. The weight loss trend of pure PMMA was similar to that reported previously.[28] The first step was a gradual weight loss below 220 °C (number 1 in **Figure 2.5a**) arising from the initiation of radical transfer to the unsaturated chain ends. The second step was a weight loss of PMMA in the temperature range from 220 to 340 °C, marked as number 2 in **Figure 2.5a**. In this temperature range, the PMMA became thermally unstable, which increased the decomposition rate. The weight loss in this step was the result of main chain scission arising from H-H bonds and radical transfer to unsaturated ends. Decomposition of the main chain scission reaction is generally expected as a first-order reaction. The last step was homolytic scission of a methoxycarbonyl side group at temperatures of 340 °C and above, which resulted in a small weight loss indicated by number 3 in **Figure 2.5a**. This was a zero-order reaction to form low molecular weight compounds.[29] The decomposition process was completed at 450 °C, which was indicated by the constant weight. The remaining weight was less than 2%, or half of the residue from the PSL decomposition at the same heating rate

(**Figure 2.5b**). In the case of PSL, the decomposition occurred in one step, which was a first-order reaction.[30,31] Meanwhile, the PMMA decomposition was a combination of first- and zero-order reactions. The combination with a zero-order reaction makes the overall activation energy of PMMA lower than that of PSL.[29,32] Furthermore, a PMMA particle has a lower decomposition temperature. The lower activation energy and lower decomposition temperature increased the opportunity for complete decomposition in a process where the temperature is elevated within a short residence time. These characteristics indicated that PMMA could be a good template for particle synthesis using spray pyrolysis. Comparison of the thermograms between the PR-PMMA blend and pure PMMA revealed that the starting temperature of the PR-PMMA blend decomposition was significantly shifted from that of pure PMMA. This shift indicated a self-organization between PMMA and the PR network.

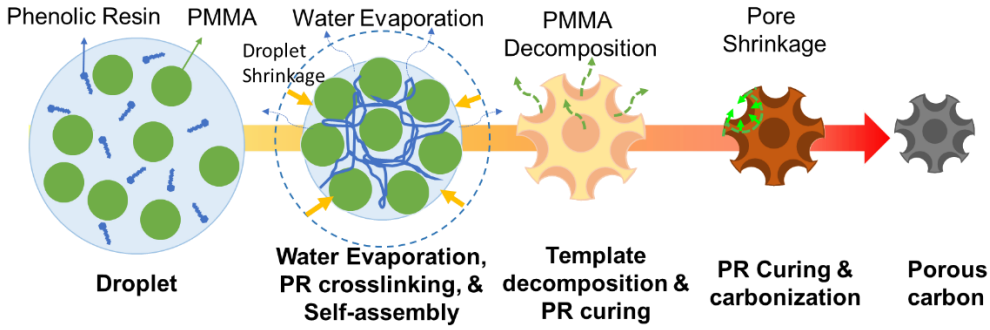

Figure 2.6. *Porous particle formation mechanism using PMMA template.*

Many factors affect the resultant particle morphology in spray pyrolysis. They include thermodynamic stabilities, hydrodynamic stabilities, and the self-assembly of the precursors in the droplet.[27,28] Based on the similar morphology of the produced porous carbon particle,[10] we predicted the particle formation mechanism using the PMMA and PSL templates to be approximately the same. As described in **Figure 2.6,** porous carbon particles were formed through four steps: (i) water evaporation, (ii) PR cross-linking and self-assembly, (iii) PMMA template decomposition and PR curing, and (iv) carbonization. The self-assembly step involved water evaporation simultaneously with the colloidal assembly of PR- PMMA in the droplet. The droplet shrank owing to the evaporation of water. An attractive force among the solid PMMA particles was then initiated because of the water evaporation. However, they remained independently distributed because of the stabilization by the repulsive force from negatively charged PR, which filled the space between PMMA particles, and from other PMMA particles. Then, phenol oligomers were cross-linked as the

water was continuously evaporated. Along with a temperature increment, PMMA decomposition took place simultaneously with the curing process. However, unlike PSL decomposition, which is complete after the curing process, the PMMA decomposition was completed earlier than the curing process. Completion of the curing process and PMMA decomposition transformed the droplet into a porous PR particle. As the curing process continued, the pores left by PMMA particles shrank along with the particle shrinkage. This implied that the presence of the pore in the curing process increased the possibility of pore size shrinkage in the final product. Therefore, when the small size of PMMA was used as the template, the parts of the skeleton that contained many pores experienced a higher shrinkage in the curing process, which resulted in greater pore shrinkage as shown in **Figure 2.4**. The pore size further shrank after the carbonization process by elevating the temperature under a nitrogen atmosphere.

Table 2.2. *Energy consumption in decomposition process*

	Sensible Heat (kJ/kg)	**Activation Energy (kJ/mol)**	**Total (kJ/mol)**
PMMA	277	129	406
PSL	390	212	602

From the commercial perspective, there was a considerable impetus to develop the porous carbon particle with an economical production process. Considering that the energy consumption determines the economy of production, **Table 2.2** compares the energy consumption of PSL and PMMA decomposition. The energy consumption was calculated based on TGA data (**Figure 2.5b**). In the decomposition process, the total energy consumption was approximated by two parameters, that is, sensible heat and activation energy of the decomposition process. The sensible heat was calculated by Newton's law of heating, within the temperature ranges of 25-220 °C and 25-345 °C for PMMA and PSL, respectively. The activation energy for the decomposition was calculated using Arrhenius's law by assuming the decomposition as a first-order reaction. As shown in **Table 2.2**, the results showed that the sensible heat of PMMA was lower than that of PSL because of the lower decomposition temperature. The activation energy of PMMA was also lower than that of PSL. This result is in good agreement with previous work by Cheng et al.,[31] which implied that the decomposition of PMMA occurred earlier than that of PSL. Overall, the energy required for PMMA decomposition was 32% lower than that for PSL.

The specific surface area values calculated using the BET equation for the dense and porous carbon particles using PMMA(A) and PMMA(B) are 361, 172, and 142 m^2/g,

respectively. The high surface area of the dense carbon is contributed by the micropores present in the carbon structure, as evidenced by the type II isotherm and form no hysteresis (**Figure 2.7a**), showing a high adsorption capacity at a relative pressure lower than 0.1P/Po. At low relative pressures (<0.1), dense carbon particles adsorbed a higher quantity of gas (N_2) compared to those of porous carbons of PMMA(A) and PMMA(B). The results implied that increasing the size of PMMA decreased the formation of micropore in the skeleton.

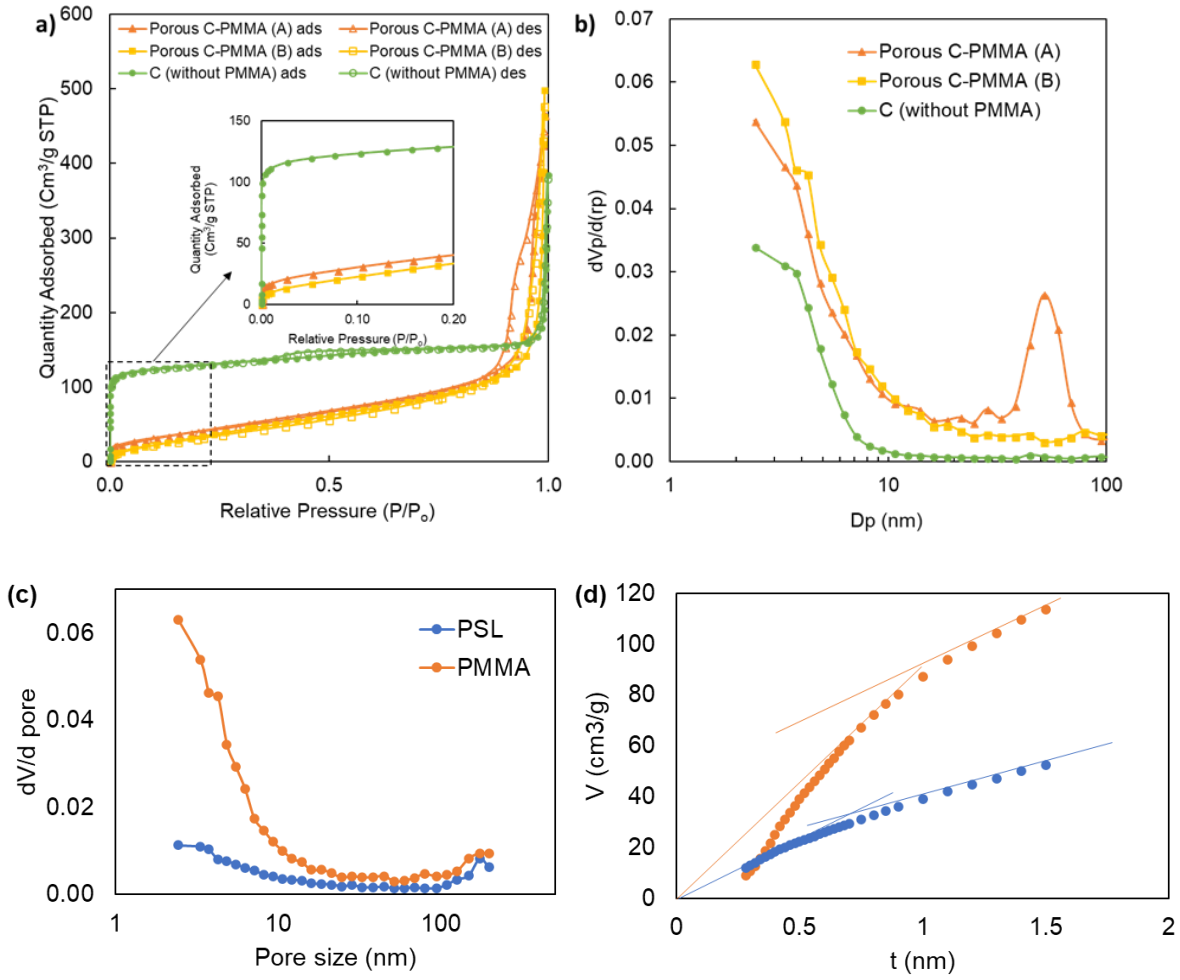

Figure 2.7. *a) N_2 -adsorption-desorption. b) Pore size distribution from Barrett-Joyner-Halenda (BJH) desorption analysis of carbon particles. c) Pore size distribution and d) t-plot measumenet of porous carbon using PMMA and PSL template*

Table 2.3 *Specific surface area of macroporous carbon particles*

Template	SSA_{BET} (m^2/g)	S_{micro} (m^2/g)	S_{meso} (m^2/g)	S_{macro} (m^2/g)
PMMA	172	41.9	58.8	71.3
PSL	70	2.7	27.1	40.2

A steep slope was observed in the region of high relative pressure (>0.9P/Po) in the adsorbed nitrogen volume of porous carbon particle, which indicated the existence of a high volume of macropores. Porous carbon particle shows that type IV isotherm with N_2 loop hysteresis above P/Po ~ 0.9 arose from the presence of mesopores. Utilization PMMA(A) shows type H2 hysteresis which means disordered and wide size distribution of pores, and PMMA(B) shows type H3 hysteresis which indicates slit-shaped pores or a lot of space between parallel plates was detected. These results indicated that the porous carbon particle using PMMA(A) and PMMA(B) contained a micropore, mesopore, and macropore. The distribution of pore size from 2 to 100 nm was calculated using the Barrett-Joyner-Halenda method, as shown in **Figure 2.7b**. The average sizes of the macropores are 55 nm for PMMA(A) and 194 nm for PMMA(B) derived porous carbon. The mesopore size was approximately 2.4 nm for all types of carbon particles. The number of mesopores increased along with the increase in size of PMMA. The formation of mesopores is attributed to the release of gas during PMMA decomposition and phenolic resin carbonization. Meanwhile, the average sizes of the micropore were 0.6 and 0.8 nm for dense and porous carbon particles, respectively, as calculated by the Horvath-Kawazoe method. However, the specific surface area of porous carbon particle in this research was higher than that from our previous research in the production of a porous carbon particle using PSL,[15] in which the specific surface area (SSA_{BET}) was 70 m^2/g with the dominating mesopore size of 2.8 nm (**Figure 2.7c**). The high surface area arose from the presence of a lower size of the micropore and mesopore and had a higher intensity than that using PSL (**Table 2.3**). In the pyrolysis process using PMMA as the template, the decomposition process of PMMA occurred earlier than that with PSL. Because the decomposition of PMMA coincided with the curing of PR, the curing stabilized the small pores formed by the released volatile gas. We determined that the micropore surface area was 94 (m^2/g) from the t-plot method, which was 57.3% of the total BET surface area. This indicated that the micropore donated a significant portion of the surface area.

2.4 Conclusion

Porous carbon particles have been synthesized from PR by spray pyrolysis using PMMA as the template. The low decomposition temperature (300 °C) and low residue left by PMMA in the decomposition process renders them effective as a template for particle synthesis using spray pyrolysis. The size of the PMMA particle affected the thickness of the porous carbon particle skeleton because of the different PR-PMMA interaction force during

self-assembly. Increasing the mass ratio of PMMA to PR had little effect on the size of porous carbon particle. The morphologies of the resultant carbon particles were the same as those obtained using the PSL template. Despite having the same morphology, the PMMA template produced a higher number of micropores and mesopores with sizes of 0.8 and 2.4 nm, respectively. These small pores contributed to a specific surface area of 172 m^2/g, which was double that of the carbon particles produced from the same carbon precursor using a PSL template. The low decomposition energy of PMMA, which was 32% lower than that for PSL, suggests a large potential for the use of PMMA in the scaled-up production of a porous material.

2.5 References

[1] L. Yu, N. Brun, K. Sakaushi, J. Eckert, M.M. Titirici, Hydrothermal nanocasting: Synthesis of hierarchically porous carbon monoliths and their application in lithium-sulfur batteries, Carbon N. Y. 61 (2013) 245–253.

[2] T. Hyodo, E. Fujii, K. Ishida, T. Ueda, Y. Shimizu, Microstructural control of porous In_2O_3powders prepared by ultrasonic-spray pyrolysis employing self-synthesized polymethylmethacrylate microspheres as a template and their NO_2-sensing properties, Sensors Actuators, B Chem. 244 (2017) 992–1003.

[3] J. Lee, Y.A. Lee, C.Y. Yoo, J.J. Yoo, R. Gwak, W.K. Cho, B. Kim, H. Yoon, Self-templated synthesis of interconnected porous carbon nanosheets with controllable pore size: Mechanism and electrochemical capacitor application, Microporous Mesoporous Mater. 261 (2018) 119–125.

[4] X. Du, C. Zhao, M. Zhou, T. Ma, H. Huang, M. Jaroniec, X. Zhang, S.Z. Qiao, Hollow carbon nanospheres with tunable hierarchical pores for drug, gene, and photothermal synergistic treatment, Small. 13 (2017) 1–11.

[5] J. Lee, J. Kim, T. Hyeon, Recent progress in the synthesis of porous carbon materials, Adv. Mater. 18 (2006) 2073–2094. doi:10.1002/adma.200501576.

[6] A.D. Roberts, X. Li, H. Zhang, Porous carbon spheres and monoliths: morphology control, pore size tuning and their applications as Li-ion battery anode materials, Chem. Soc. Rev. 43 (2014) 4341–4356.

[7] T. Mori, S. Iwamura, I. Ogino, S.R. Mukai, Optimization of practical activation depth for effective CO_2 activation using PMMA-templated carbons with a tailorable pore system of meso- and macropores, J. Porous Mater. 24 (2017) 1497–1506.

[8] C. Liang, Z. Li, S. Dai, Mesoporous carbon materials: Synthesis and modification, Angew. Chemie - Int. Ed. 47 (2008) 3696–3717.

[9] M. Inagaki, H. Konno, O. Tanaike, Carbon materials for electrochemical capacitors, J. Power Sources. 195 (2010) 7880–7903.

[10] R. Balgis, S. Sago, G.M. Anilkumar, T. Ogi, K. Okuyama, Self-Organized Macroporous Carbon Structure Derived from Phenolic Resin via Spray Pyrolysis for High-Performance Electrocatalyst, ACS Appl. Mater. Interfaces. 5 (2013) 11944–11950.

[11] W. Ng, Y. Yang, K. van der Veen, G. Rothenberg, N. Yan, Enhancing the performance of 3D porous N-doped carbon in oxygen reduction reaction and supercapacitor via boosting the meso-macropore interconnectivity using the "exsolved" dual-template, Carbon N. Y. 129 (2017) 293–300.

[12] J. Seo, H. Park, K. Shin, S.H. Baeck, Y. Rhym, S.E. Shim, Lignin-derived macroporous carbon foams prepared by using poly(methyl methacrylate) particles as the template, Carbon N. Y. 76 (2014) 357–367.

[13] K. Waldron, Z. Wu, D. Zhao, X.D. Chen, C. Selomulya, On Spray Drying of Uniform Mesoporous Silica Microparticles, Mater. Today Proc. 3 (2016) 646–651.

[14] R. Balgis, T. Ogi, W.-N. Wang, G.M. Anilkumar, S. Sago, K. Okuyama, Aerosol Synthesis of Self-Organized Nanostructured Hollow and Porous Carbon Particles Using a Dual Polymer System, Langmuir. 30 (2014) 11257–11262.

[15] R. Balgis, T. Ogi, A.F. Arif, G.M. Anilkumar, T. Mori, K. Okuyama, Morphology control of hierarchical porous carbon particles from phenolic resin and polystyrene latex template via aerosol process, Carbon N. Y. 84 (2015) 281–289.

[16] A.F. Arif, R. Balgis, T. Ogi, T. Mori, K. Okuyama, Experimental and theoretical approach to evaluation of nanostructured carbon particles derived from phenolic resin via spray pyrolysis, Chem. Eng. J. 271 (2015) 79–86.

[17] T. Ogi, A.B.D. Nandiyanto, K. Okuyama, Nanostructuring strategies in functional fine-particle synthesis towards resource and energy saving applications, Adv. Powder Technol. 25 (2014) 3–17.

[18] F. Iskandar, L. Gradon, K. Okuyama, Control of the morphology of nanostructured particles prepared by the spray drying of a nanoparticle sol, J. Colloid Interface Sci. 265 (2003) 296–303.

[19] F. Iskandar, Mikrajuddin, K. Okuyama, In Situ Production of Spherical Silica Particles Containing Self-Organized Mesopores, Nano Lett. 1 (2001) 231–234.

[20] F. Iskandar, Mikrajuddin, K. Okuyama, Controllability of Pore Size and Porosity on Self-Organized Porous Silica Particles, Nano Lett. 2 (2002) 389–392.

[21] K. Sasahara, T. Hyodo, Y. Shimizu, M. Egashira, Macroporous and nanosized ceramic films prepared by modified sol-gel method with PMMA microsphere templates, J. Eur. Ceram. Soc. 24 (2004) 1961–1967.

[22] L. Gammelgaard, J.M. Caridad, A. Cagliani, D.M.A. MacKenzie, D.H. Petersen, T.J. Booth, P. Bøggild, Graphene transport properties upon exposure to PMMA processing and heat treatments, 2D Mater. 1 (2014). doi:10.1088/2053-1583/1/3/035005.

[23] K. Zhang, L. Zheng, X. Zhang, X. Chen, B. Yang, Silica-PMMA core-shell and hollow nanospheres, Colloids Surfaces A Physicochem. Eng. Asp. 277 (2006) 145–150.

[24] Y.B. Jiang, L.H. Wei, Y.Z. Yu, T. Zhao, Preparation of porous carbon particle with shell/core structure, Express Polym. Lett. 1 (2007) 292–298.

[25] D. Sen, S. Mazumder, J.S. Melo, A. Khan, S. Bhattyacharya, S.F. D'Souza, Evaporation driven self-assembly of a colloidal dispersion during spray drying: Volume fraction dependent morphological transition, Langmuir. 25 (2009) 6690–6695.

[26] Y.J. Kim, M. Il Kim, C.H. Yun, J.Y. Chang, C.R. Park, M. Inagaki, Comparative study of carbon dioxide and nitrogen atmospheric effects on the chemical structure changes during pyrolysis of phenol-formaldehyde spheres, J. Colloid Interface Sci. 274 (2004) 555–562.

[27] S.L. Malhotra, L. Minh, L.P. Blanchard, Thermal Decomposition and Glass Transition Temperature of Poly(Ethyl Methacrylate) and Poly(N-Butyl Methacrylate), J. Macromol. Sci. Part A - Chem. 19 (1983) 559–578.

[28] M. Ferriol, Gentilhomme, M. Cochez, Thermal degradation of poly (methyl methacrylate)(PMMA): modelling of DTG and TG curves, Polym. Degrad. 79 (2003) 271–281.

[29] T.L. Tsai, C.C. Lin, G.L. Guo, T.C. Chu, Chemical kinetics of polymethyl methacrylate (PMMA) decomposition assessed by a microwave-assisted digestion system, Ind. Eng. Chem. Res. 47 (2008) 2554–2560.

[30] J.D. Peterson, S. Vyazovkin, C.A. Wight, Kinetics of the thermal and thermo-oxidative degradation of polystyrene, polyethylene and poly(propylene), Macromol. Chem. Phys. 202 (2001) 775–784.

[31] J. Cheng, Y. Pan, J. Yao, X. Wang, F. Pan, J. Jiang, Mechanisms and kinetics studies on the thermal decomposition of micron Poly (methyl methacrylate) and polystyrene, J. Loss Prev. Process Ind. 40 (2016) 139–146.

[32] G.N. Eyler, C. Minellono, G. Barreto, A. Cañizo, G.E. Morales, A. Brandolin, M. Asteasuain, Thermal decomposition reaction of pinacolone diperoxide: its use as radical initiator in the styrene polymerization, Polym. Bull. 74 (2017) 3545–3556.

Chapter 3

TOCN decorated macroporous silica particles: Synthesis, characterization, and protein adsorption performance

3.1 Introduction

Research on protein adsorption has attracted considerable attention in recent years due to promising developments in diverse biomedical applications, such as separation, purification, biosensor analysis, immobilization of protein and biomolecules delivery [1–3]. The mechanism of protein adsorption on the solid surface of an adsorbent is driven by the combinative forces of electrostatic, chemical interactions, and van der Waals interaction [4–6]. The choice of the adsorbent material is the most important in controlling protein adsorption properties.

Cellulose nanofiber (CNF) is a commonly used material in membrane chromatography and filtration for being chemically resistant and inexpensive and possessing a high surface area, and good non-specific binding properties [7–9]. However, to enhance affinity toward specific protein, cellulose must be modified to exhibit acidic functional groups via the oxidation of the hydroxyl group of cellulose. Saito et al. [10,11] had developed the system of oxidation of cellulose with 2,2,6,6-tetramethylpiperidine -1-oxyl radical (TEMPO) with hypochlorite and bromide to convert the C6 primary hydroxyl group to a carboxylate group. TEMPO-oxidized cellulose nanofibers (TOCN) are a promising nanomaterial because of various advantages. First, TOCN has a homogeneous width of ~3 nm and a high aspect ratio (>150). Second, TOCN contains rich carboxyl that leads to a highly-negative charge [12–14]. The negative charge of TOCN in water causes electrostatic repulsion between TOCN, which leads to good dispersion in the wet state. In addition, with the carboxylate groups, TOCN is expected to exhibit a high affinity toward positively-charged compounds. Previous studies on TOCN showed significantly high adsorption for heavy metal ions [15,16]. Even so, there is no research regarding the utilization of TOCN, especially in the particle form as a protein adsorbent material. TOCN is believed to be an effective adsorbent to specific protein considering their high content of carboxylate groups and negative charge.

For use as an adsorbent, highly-dispersed TOCN would be desired even in the dried state. However, TOCN is easily aggregated in a drying process at elevated temperature. Aggregation between CNF occurs through diffusion forces and hydrogen bond formation [17]. Zheng et al. (2019) prepared a dried-state TOCN particle using a spray drying technique for hydrophobic materials [18]. A large amount of TOCN aggregates towards the droplet core with shrinkage during the rapid drying process, which leads to a dense morphology. This dense morphology decreases the surface area and porosity and significantly degrades the performance of adsorption capacity. Therefore, the preparation of TOCN particles that maintain their high surface area is challenging. Hence, in this chapter, we focus on low TOCN loading on a macroporous SiO_2 particle, which is predicted to prevent aggregation and shrinkage of TOCN in the drying process and maintain the pore site between negatively-charged TOCN.

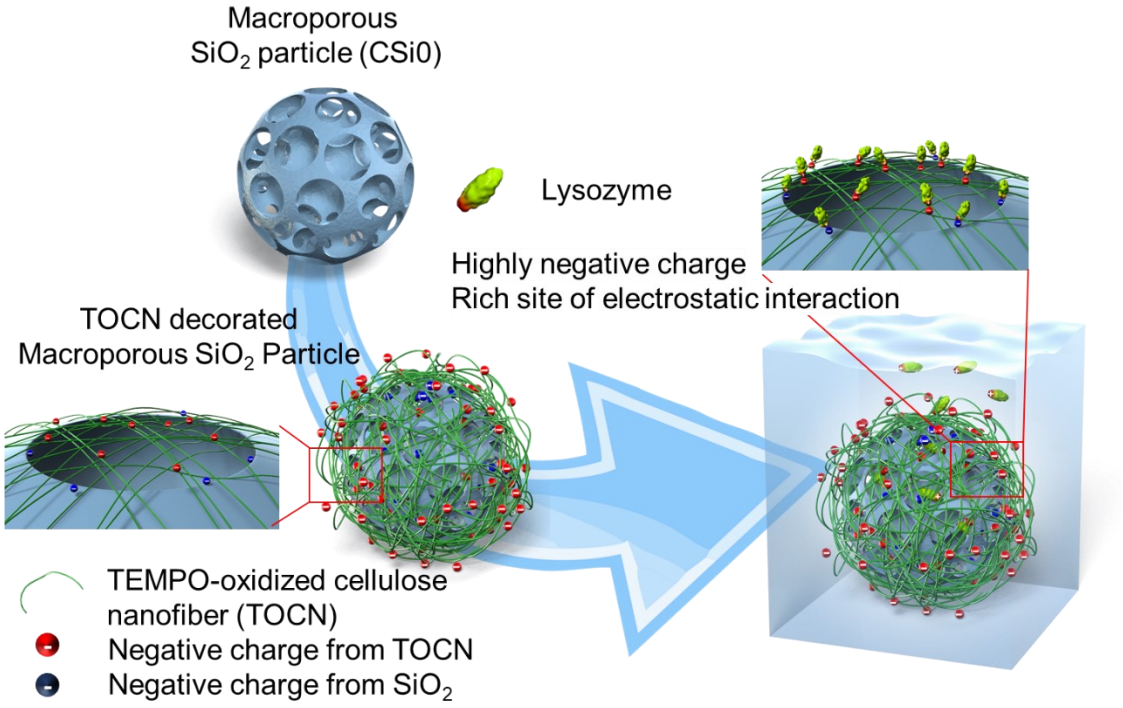

Figure 3.1. *Schematic illustration of a TOCN-decorated macroporous SiO_2 particle*

Figure 3.1 shows the concept of this research. Another important aspect of the proposed concept in this study is the utilization of a macroporous structure of SiO_2 particles as a support particle for loading TOCN. Classified as a "generally regarded as safe" (GRAS) agent by the U.S. Food And Drug Administration (FDA), silica is an ideal candidate material for biomedical fields [19]. The macroporous structure gives a promising superiority compared to the mesoporous structure such as better permeability, better mass transfer

diffusion, better intraparticle effective diffusivity, lower column back pressure, and more regular flow regime in static bed column [20–22]. Therefore, in this study, we prepared TOCN decorated macroporous SiO_2 (TOCN@macroporous SiO_2) particles, as shown in **Figure 3.1**. We expect the presence of macroporous SiO_2 prevent aggregation of TOCN and facilitate penetration of fluid to contact TOCN by passing through the interconnected pores, which leads to an improvement of adsorption performance.

The adsorption performance was examined by evaluating the interactions between TOCN@macroporous SiO_2 particles and lysozyme. Lysozyme was used as a model adsorption protein due to its beneficial use in alcoholic fermentation, as a fining agent to remove excess tannins, classified as a hidden allergen, and availability in body fluids or food matrices [23,24]. Their adsorption performance was compared with the pure TOCN particle and commercial cellulose beads.

3.2 Experimental

3.2.1. Preparation of the TOCN@macroporous SiO_2 particles.

The preparation of TOCN@macroporous SiO_2 particles consists of two steps as shown schematically in **Figure 3.2**. Preparation of the macroporous SiO_2 particles (CSi0). Macroporous silica particles were produced in accordance with previous chapter using silica nanoparticles (Nissan Chemical Ind. Ltd., particle size around 5 nm) and 503-nm diameter polymethyl methacrylate (PMMA, Sekisui Plastics Co., Ltd., Tokyo, Japan) as the template. An aqueous silica solution containing 12 wt.% silica nanoparticles were added to the PMMA particles at a mass ratio of 1:2 (silica:PMMA). The silica concentration in the precursor was adjusted to as high as 2 wt.% by adding ultrapure water; the solution was then sonicated for 1 hour. The precursor was sprayed using an ultrasonic nebulizer with N_2 (1 mL/min) as the carrier gas through a tubular furnace with four stacked temperature zones set to 150, 350, 500, and 500°C. CSi0 was collected using a paper filter that was maintained at 150°C to prevent water condensation.

The synthesis of TOCN decorated CSi0 particles was started with the surface modification of CSi0 using poly(diallyldimethylammonium chloride) (PDDA, 20 wt.% in water, MW = 100.000-200.000, Sigma–Aldrich) to change the surface charge from negative to positive. 50 mg CSi0 was dispersed in 100 mL of a 1 wt.% PDDA solution by stirring for 30 minutes at room temperature, followed by centrifugation at 8000 rpm for 5 minutes. The positively charged CSi0 (CSi0M) was washed twice with ultrapure water to remove excess PDDA. In other hand, an aqueous solution of TOCN was prepared through a dispersion of 2

wt.% TOCN (DKS Co., Ltd., Japan) in ultrapure water to reach 0.1 wt.% under 5 minutes of pre-stirring for at room temperature, then followed by stirring and heating at 80°C for 5 minutes in a microwave. CSi0M was poured into an aqueous solution of TOCN in different mass ratios (TOCN/SiO_2 = 0 4) and stirred for 2 hours at 50°C and 800 rpm. The TOCN-CSi0M solution was dried using spray drying at 180°C.

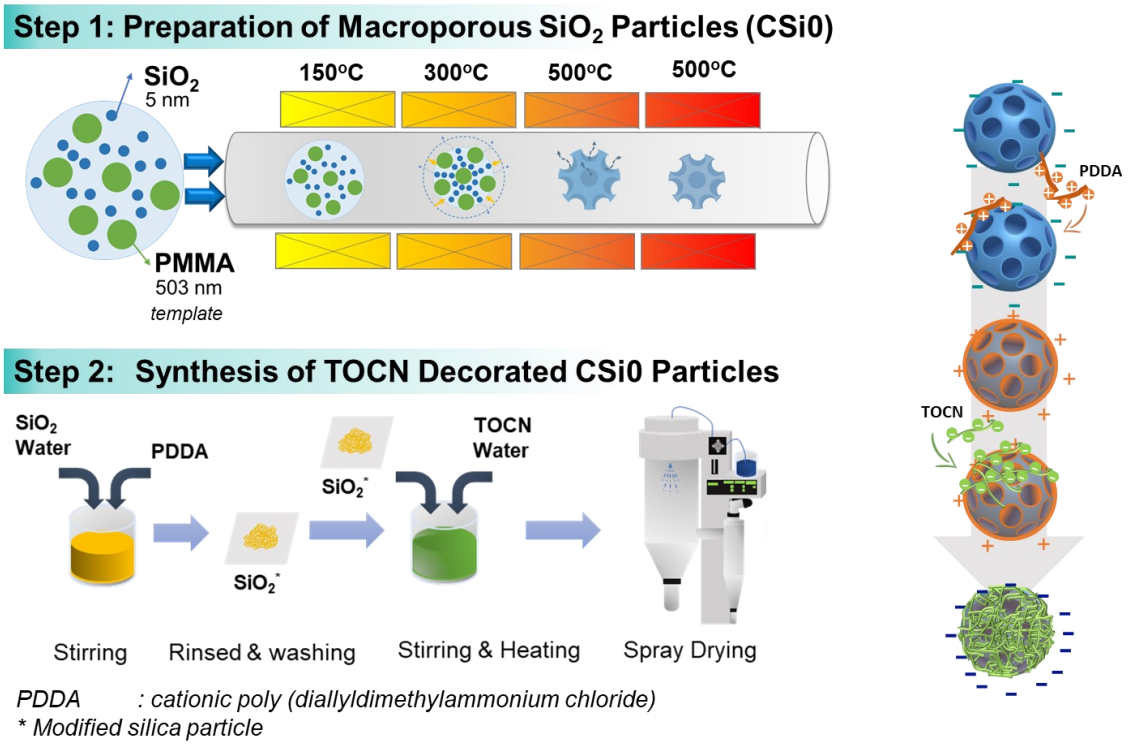

Figure 3.2. *Schematic of the synthesis of TOCN@macroporous SiO_2 particles*

Pure TOCN particle and commercial cellulose beads (Cfine, Cellufine^{TM}, JNC Corporation, Tokyo, Japan) were used as reference materials for performance comparison. Each pure TOCN and the Cfine material was diluted in ultrapure water then sprayed using spray drying in the same condition as the other samples.

3.2.2 Characterization of the TOCN@macroporous SiO_2 particles

The particle morphology was observed using scanning electron microscopy (SEM) (S-5000, Hitachi Ltd., Tokyo, Japan) at 3.0–20 kV, under a nitrogen atmosphere. The particles were prepared by dispersing in ethanol before being pipetted dropwise onto an aluminum plate and subjected to heating at 40 °C. Thereafter, the dispersed particles were covered by a thin layer of sputtered platinum. The particle size distribution and ζ- potential value were obtained by dynamic light scattering using a ZS nano analyzer (Malvern Instrument Inc., London, U.K.) after dispersing 1 w/v% particles in the water for 30 min.

Thermogravimetric analysis (TGA-50/50H, Shimadzu Corp, Kyoto, Japan) was used to determine the loading amount of TOCN in the TOCN@macroporous SiO_2 particle. The N_2 adsorption/desorption isotherms (BELSORP-max, BEL Japan, Osaka, Japan) were measured after preheating the samples at 180 °C for 3 hr. The SSA was determined quantitatively using the Brunauer-Emmett-Teller model. The pore size distribution was established using the Barrett-Joyner-Halenda model.

3.2.3 Adsorption capacity of TOCN@macroporous SiO_2 particles

To investigate the adsorption capacity of the prepared adsorbent, lysozyme (MP Biomedicals) was employed as model molecule. Aqueous lysozyme (with an isoelectric point of 10.5) solutions with a concentration of 0.4 mg mL^{-1} and a pH value of 7 were prepared using phosphate buffer. To test the static adsorption performance, 10 mg of the as-prepared adsorbents were immersed in 50 mL of the lysozyme aqueous solution. The mixed solution was then stirred at room temperature for 2 hours. An approximately 5 mL sample was withdrawn periodically then subjected to centrifugation (8000 rpm). The absorbance intensity change of the supernatant was measured at 281 nm using a UV-Vis spectrophotometer (UV-3150, Shimadzu, Japan) from 240 to 400 nm at room temperature.

The adsorption capacities of the all adsorbents were calculated by equation (3.1):

$$\mathrm{Q_e} = \frac{(\mathrm{C_0} - \mathrm{C_1})}{\mathrm{m}}.\mathrm{V} \tag{3.1}$$

where Q_e (mg/g) is the equilibrium adsorption capacity for lysozyme, C_0 and C_1 (mg/mL) refer to the concentration of lysozyme before and after adsorption, respectively, V (50 mL) is the volume of the solution, and m is the mass (0.005 g) of the adsorbent.

3.2.4 Reusability studies of the TOCN@macroporous SiO_2 particles

Reusability studies were conducted by chemically releasing the lysozyme from the surface of the particle, as shown for 1 cycle in **Figure 3.3**. Lysozyme and the 5 mL buffer solution were put in a flask, and 1 mg of a TOCN@macroporous SiO_2 particle was added followed by stirring for 5 minutes. After centrifugation, the supernatant solution was measured using UV-Vis at a wavelength of 281 nm for percentage adsorbed lysozyme (%C) using following equation:

$$\%C_{ads} = \frac{(C_0 - C_1)}{C_0}.100\% \tag{3.2}$$

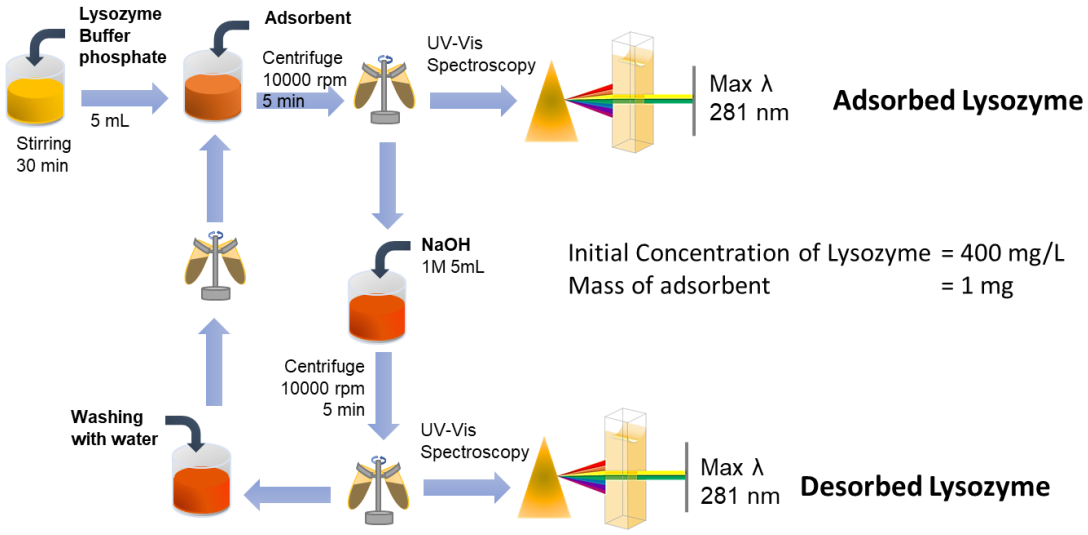

Figure 3.3. *One cycle of adsorption-desorption capacity analysis procedure.*

The desorption process was performed by adding 5 mL of NaOH (pH 11.5) to disperse the precipitates again. After centrifugation, the supernatant was measured again to get the concentration after desorption (C2). Percentage of desorption lysozyme was calculated using following equation:

$$\%C_{des} = \frac{(C_x - C_2)}{C_x}.100\% \tag{3.3}$$

Where Cx is the concentration of lysozyme on the adsorbent $(C_0 - C_1)$

All of the experiments, including spray pyrolysis, adsorption performance, and reusability test, were conducted three times. The average value was taken from three separate sets of data. After centrifugation, remove 3 mL of the supernatant solution and measured using UV-Vis at wavelength 281 nm

3.3 Results and Discussion

3.3.1 Characteristics of TOCN@macroporous SiO_2 particles

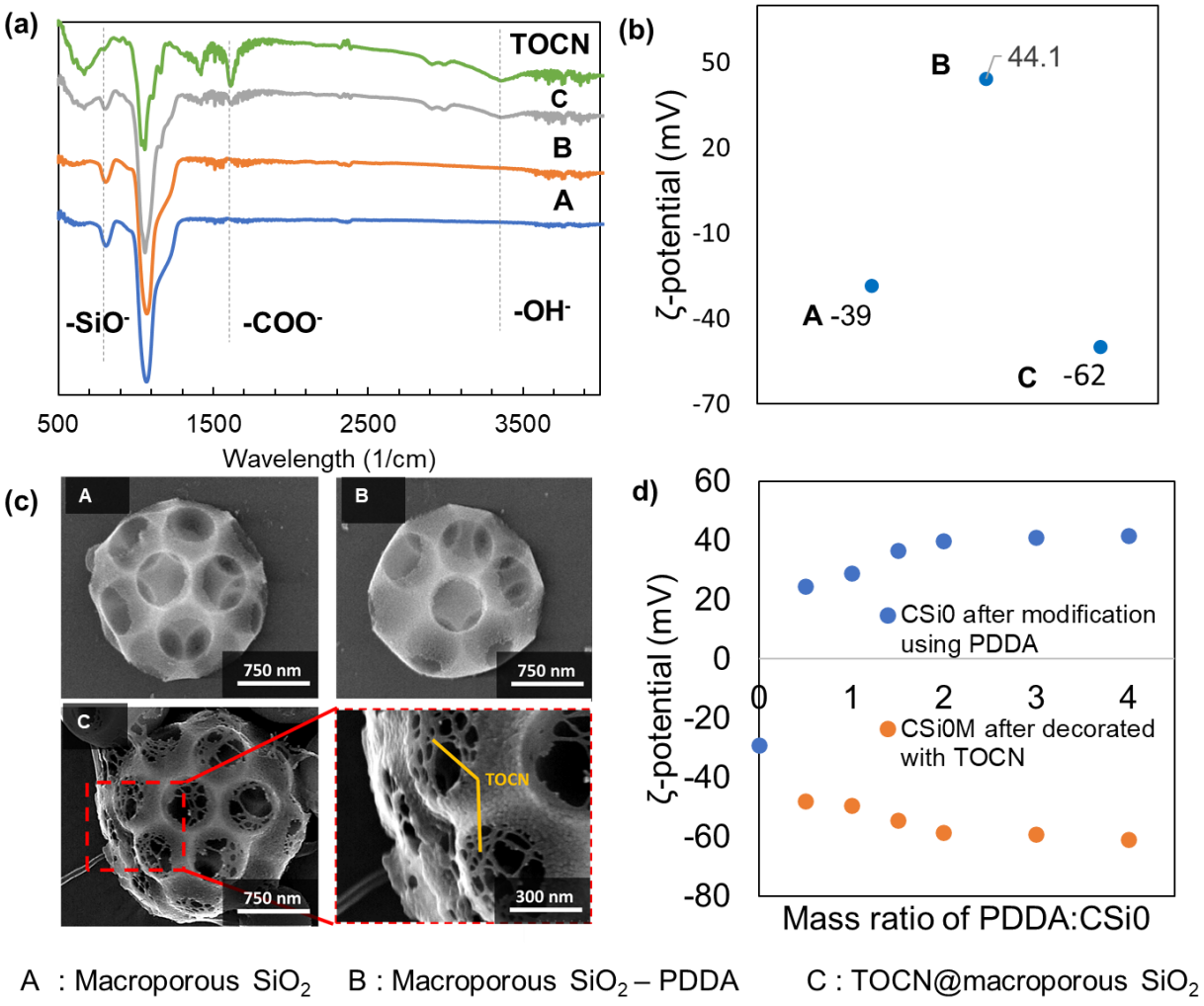

Figure 3.4. *(a) FT- IR spectra of the step-wise preparation of the TOCN@macroporous SiO_2 particles. (b) Change of ζ-potential before and after TOCN decoration. c) SEM images of A) CSi0, B) CSi0M, and C) TOCN@CSi0M with 30% concentration of TOCN. d)Zeta potential of CSi0 and CSi0M in effect of PDDA concentration.*

TOCN decoration of the macroporous silica particle surface was confirmed by FTIR spectral analysis and SEM images as shown in **Figure 3.4**. **Figure 3.4a** summarizes the FTIR spectra of the CSi0, CSi0M, TOCN@CSi0M, and TOCN. CSi0 has three intense and dominant peaks at 802, 968, and 1097 cm^{-1} assigned to Si–O bending, Si–OH stretching, and Si–O-Si stretching, respectively [25]. The FTIR features of CSi0M confirmed the emergence of new, low-intensity peaks at 1472 cm^{-1} ($-CH_2$) and 1568 cm^{-1} (C=C and C=N in-plane vibration) that belonged to the characteristic bands of PDDA [26]. Even so, the morphology of CSi0M was no different than CSi0 (**Figure 3.4c**) which also showed sphere particles with

porous structure. However, the ζ-potential changed from -39 ± 3 mV (CSi0) to +40 ± 4 mV (CSi0M). The change of surface charge of silica indicated the presence of PDDA on the surface of silica (**Figure 3.4b**). The amount of PDDA loading was optimized through the variation of PDDA/silica particle mass ratio(**Figure 3.4d**). The optimum condition reached at the mass ratio of PDDA/silica particle is 2 with the mass loading of PDDA is 0.025 mg PDDA/mg CSi0M. Since CSi0 has negative charge and PDDA has positive charge of polyelectrolyte, PDDA can encase the CSi0 surface by electrostatic force and finally reverse the surface charge [27]. After modification, TOCN successfully decorated the surfaces of the CSi0M with low loading and good dispersion **(Figure 3.4c**). Decoration of TOCN occurred through the electrostatic interaction between positively charged PDDA and carboxyl group-TOCN. Since there are a big gap of surface charge of positively-charged CSi0M (40 mV) and the negatively-charged TOCN (-63 mV, dispersed TOCN in the water), we suspect there is strong anion-cation interaction between them in TOCN@CSi0M. TOCN@CSi0M indicates that the Si-O- band at 968 cm^{-1} was reduced in intensity and the characteristic bands of PDDA at 1472 cm^{-1} and 1568 cm^{-1} were disappeared due to the decoration of the TOCN. In addition, new absorption bands belonging to TOCN emerged. The wide range of 669 and 3352 cm^{-1} was assigned to the stretching vibration of hydroxyl (-OH) groups. Characteristic bands at 1034 cm^{-1} correspond to C-O-C pyranose ring stretching vibration in cellulose. The particular characteristic band of TOCN at 1606 cm^{-1} confirms the presence of the carboxylate group [28]. These strong characteristic bands and the SEM image of TOCN@CSi0M indicate that TOCN successfully decorated the surface of silica, and the FTIR results suggest that TOCN@CSi0M exhibits similar characteristic peaks for TOCN.

Table 3.1. *Sample name of the TOCN@macroporous SiO_2 particles*

Sample Name	**Mass conc. in particle (%)**		**ζ-potential (mV)**	**Size (µm)***
	SiO_2	TOCN		
CSi0	100	-	-39	1.51
CSi30	70	30	-55	1.67
CSi50	50	50	-58	1.82
CSi80	40	80	-62	2.08
CSi100	-	100	-60	2.27

*) Dynamic Light Scattering

The TOCN@macroporous SiO_2 particle was prepared with various TOCN mass concentrations. The TOCN@macroporous SiO_2 particle containing 30% TOCN was named CSi30, and so on for 50%, 80%, and 100% TOCN as listed in **Table 3.1**. The effect of the TOCN concentration on the ζ-potential, particle size, and morphology were investigated. The ζ-potential data of all prepared samples were negative. CSi0 has the smallest particle size and lowest negative ζ-potential. The negative charge of CSi0 is owing to the silanol group. TOCN has a highly-negative charge due to the carboxylic group. Increasing the TOCN concentration increases the particle size slightly and increases the negative value of ζ-potential significantly closer to that of pure TOCN, indicating that a slight increase in particle size was caused by higher loading of TOCN on the surface so that the ζ-potential is closer to pure TOCN. Despite the TOCN loading of up to half of the pure TOCN concentration, the ζ-potential is highly negative. Interestingly, the CSi80 exhibited the most negative charges among the samples. The negative charge of CSi80 could be attributed to the presence of carboxyl and silanol groups (**Figure 3.5**).

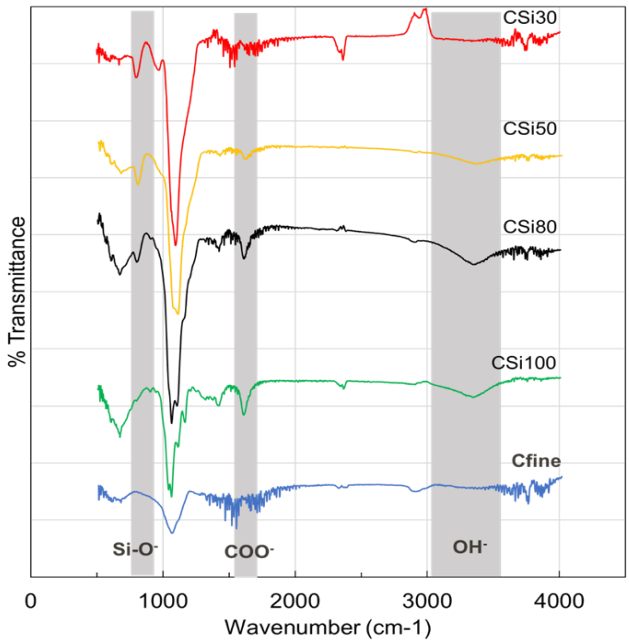

Figure 3.5. *FTIR spectra of CSi30, CSi50, CSi80, CSi100, and Cfine.*

The morphologies of the TOCN@macroporous SiO_2 particles in various concentrations were observed by SEM, as shown in **Figure 3.6**. From **Figure 3.6a**, CSi0 was sphere particles with 500 nm diameter of surface macropores. The addition of TOCN causes the surface of the macroporous particles to be covered by a thin layer of fibers, as shown in **Figure 3.6b.** Increasing the amount of TOCN loading increases the thickness of the fibers, reduces the site of the open silica macropores (**Figure 3.6b-d)**, and increases the particle size

(**Table 3.1**). In contrast to the TOCN@macroporous SiO_2 particle with low loading of TOCN, CSi80 particles had a rougher surface structure (**Figure 3.6d inset**). The rough structure was due to well-packed TOCN that produced dense grooves and a wrinkled surface. This morphology is similar to CSi100, which had a rough surface but more wrinkles (**Figure 3.6e**). CSi100 consisted of an irregular sphere with a concave and wrinkled morphology due to rearranging of TOCN inside the droplet, then rapid shrinking with the drying process. The TOCN@macroporous SiO_2 particle maintained their round shape because porous silica prevents TOCN from undergoing reconstruction during the evaporation process. The commercial cellulose bead (Cfine) had a spherical form (**Figure 3.6f**) with particle size greater than 30 μm and a ζ-potential of -56 mV.

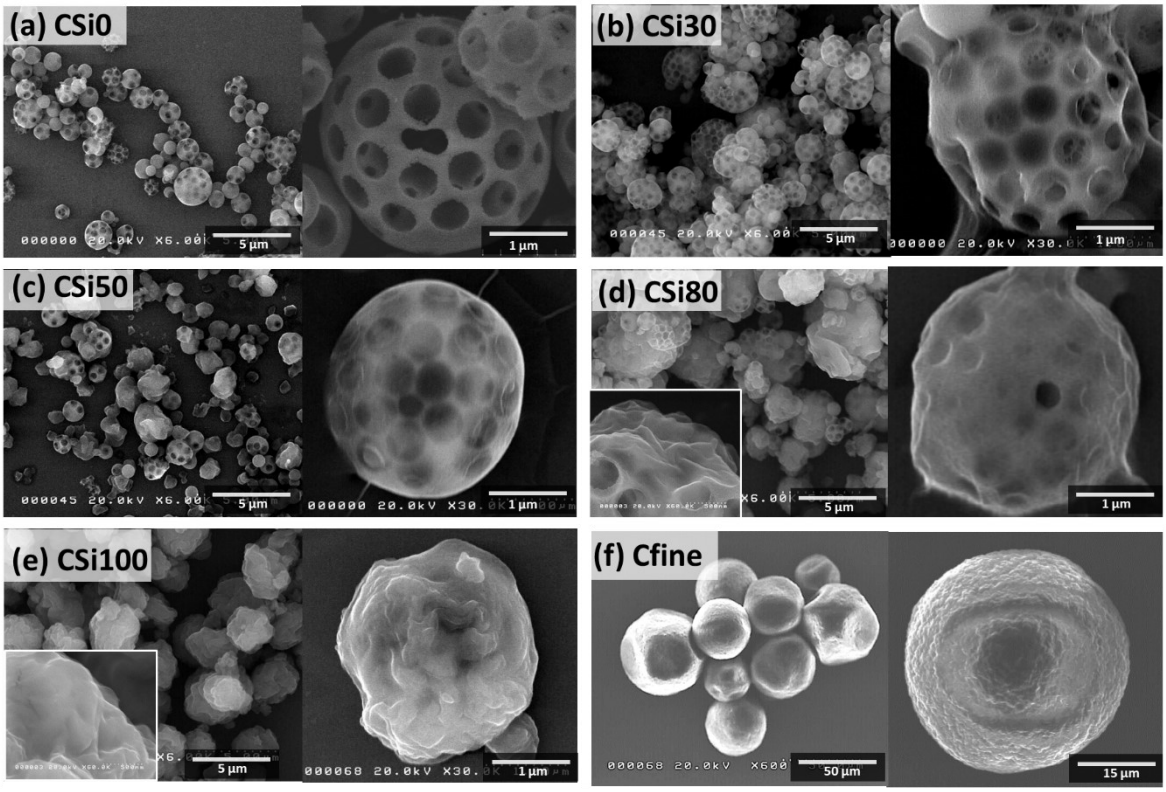

Figure 3.6. *SEM images of the TOCN@macroporous SiO_2 particles in various concentrations of TOCN; (a) CSi0, (b) CSi30, (c) CSi50, (d) CSi80, and (e) CSi100. (f) Commercial cellulose Cfine bead as a comparison sample.*

3.3.2 Protein adsorption performances of TOCN@macroporous SiO_2 particles

A highly-negative zeta potential makes TOCN@macroporous SiO_2 particles a suitable agent to interact with positively-charged groups of compounds or materials. Here, we used lysozyme as a model protein to investigate the adsorption properties of TOCN@macroporous SiO_2 particles for positive proteins. The isoelectric point (pI) of the

lysozyme used in this study was 10.5, indicating it was positively charged at pH < 10.5. Thus, adsorption (ion-exchange) of lysozyme to the TOCN@macroporous SiO_2 particle is possible by electrostatic interaction. In addition, there are possibilities of chemical interactions between carboxyl groups of the TOCN@macroporous SiO_2 particle with the functional amino acid group of lysozymes through amide binding [29].

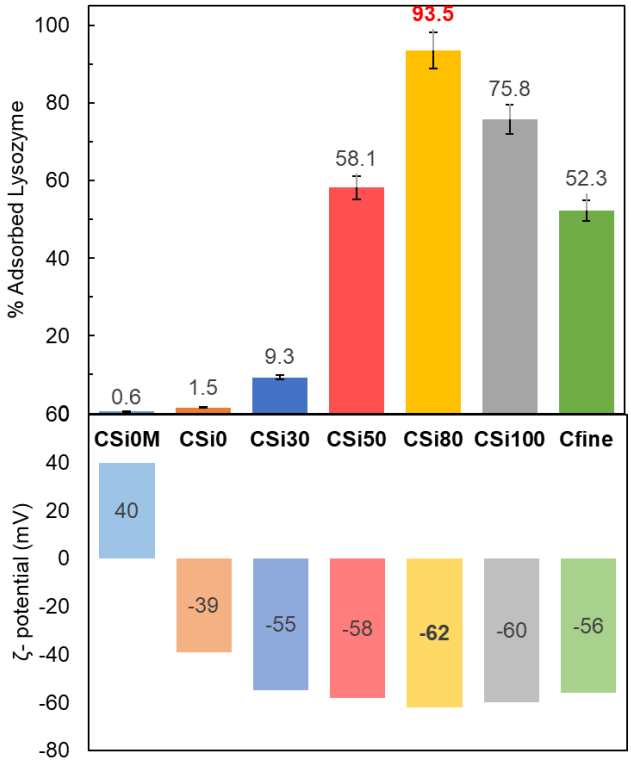

Figure 3.7 *Adsorption capacities for lysozyme at 2 h and ζ-potential of the samples at pH 7 and room temperature (23-25°C)*

Figure 3.7 shows the lysozyme adsorption capacity with different TOCN@macroporous SiO_2 particles and Cfine as adsorbent at an initial lysozyme concentration of 0.4 mg mL^{-1}. The adsorbent concentration was 0.2 mg mL^{-1}. The maximum amount of lysozyme adsorbed at the equilibrium of the TOCN@macroporous SiO_2 particles reached 93.5% using CSi80, and the minimum amount reached 0.6% using CSi0M as the adsorbent. The adsorption capacities of lysozyme decrease sharply with decreasing concentration of TOCN. It is suggested that at lower TOCN concentrations, the interactions between TOCN@macroporous SiO_2 particle and lysozyme is not very strong. The maximum amount of lysozyme adsorbed at the equilibrium of Cfine was 1046 mg g^{-1}, which is less than CSi50 (1170 mg g^{-1}). Despite Cfine consisting of rich carboxymethyl groups [30], the negative ζ-potential of Cfine (-56 mV) is less than CSi50 (-58 mV). The better adsorption

capacity of CSi80 is in exceptionally good agreement with existing ζ-potential results. As comparison, CSi0M that has positive charge has the lowest adsorption capacities of lysozyme. The value of zeta potential plays a central role in effectively seizing the positively charged of lysozyme to negatively charged TOCN-Silica. In this case, the electrostatic interaction may play the most important role in enhancing the protein adsorption capacity of appropriate functional groups.

The mechanism of adsorption of lysozyme by the TOCN@macroporous SiO_2 particle was confirmed using adsorption kinetic fitting, as shown in **Table 3.2.** To understand the rate-controlling processes, pseudo-first-order (PFO) and pseudo-second-order (PSO) kinetic models were adapted to fit the experimental data and to investigate the adsorption kinetics of lysozyme onto the as-prepared adsorbents in this work. The PFO and PSO models are expressed below[31]:

i. PFO

$$\mathrm{Q_t} = \mathrm{Q_{e1}}\left(1 - \mathrm{e^{-k_1 t}}\right) \tag{3. 4}$$

The linear equation of equation (3.2) becomes:

$$ln(Q_e - Q_t) = \ln(Q_{e1}) - k_1 t \tag{3. 5}$$

ii. PSO

$$Q_t = \frac{\mathrm{k_2 Q_{e2}^2 t}}{1 + \mathrm{k_2 Q_{e2} t}} \tag{3. 6}$$

The linear equation of equation (3.4) becomes:

$$\frac{t}{Q_t} = \frac{1}{\mathrm{k_2 Q_{e2}^2}} + \frac{t}{\mathrm{Q_{e2}}} \tag{3. 7}$$

where *Qt* (mg/g) is the adsorption uptake as a function of time. From plotting ln (*Qe*−*Qt*) vs *t* for PFO, the value of Qe_1 (equilibrium adsorption capacity of the PFO model, mg/g) can be calculated from the intercept, and k_1 (PFO rate constant, min^{-1}) can be calculated from the slope value. For PSO, the Qe_2 parameter (equilibrium adsorption capacity of the PSO model, mg/g) and k_2 (PSO rate constant models, g/mg·min) can be calculated from plotting *t*/*Qt* vs *t*.

Pseudo-first-order (PFO) and pseudo-second-order (PSO) kinetic models were adapted to fit the experimental data and investigate the adsorption kinetics of molecular

protein on the TOCN@macroporous SiO_2 particle synthesized in this work. The Q_{e2} values determined with the PSO model agreed very well with the experimental adsorption capacity values, i.e., Qe_{exp}, with the correlation coefficient R^2 values were also closer to unity as listed in **Table 3.2**.

Table 3.2. *PFO and PSO kinetic parameters for lysozyme adsorption*

Sample	Qe_{exp} (mg/g)	PFO		PSO	
		Qe_1 (mg/g)	R^2	Qe_2 (mg/g)	R^2
CSi0M	12.4	13.8	0.24	12.9	0.89
CSi0	27.8	10.5	0.53	32.0	0.85
CSi30	191.8	3.8	0.89	185.2	0.99
CSi50	1170.1	599.7	0.91	1250.0	0.99
CSi80	1872.6	68.9	0.33	2000.0	1.00
CSi100	1524.0	391.4	0.87	1428.6	0.99
Cfine	1045.9	641.1	0.96	1111.1	0.99

This result suggests that the chemisorption was more related as rate-determining step of adsorption process [32,33]. Therefore, the observation result of adsorption capacity in the effect of contacting time was shown in **Figure 3.8** with PSO model as the fitting line. Interestingly, though CSi100 has the highest loading of TOCN among all samples, its adsorption capacity is less than CSi80. As can be seen from **Figure 3.8**, the adsorption of lysozyme by CSi80 exceeded 90% of the initial amount of lysozyme in less than 5 minutes, with no significant increase with more adsorption time. Alternatively, the rates for CSi100 and commercial beads were initially slow, continuing to increase for the next 2 hours slightly. We expect the high adsorption of CSi80 particles were contributed by the higher specific surface area of CSi80 compared to CSi100 particles.

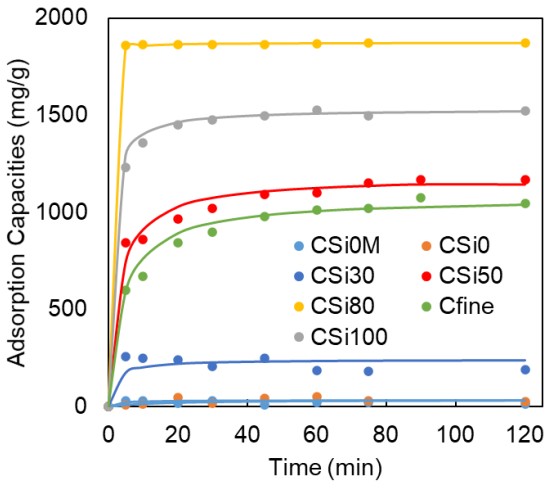

Figure 3.8. *Adsorption rates for lysozyme of the samples*

Table 3.3. *Surface area and pore volume of Cfine, CSi100, and CSi80*

Sample Name	S_{BET} (m^2/g)	$V_{Mesopore}$ (cm^3/g)	$V_{Micropore}$ (cm^3/g)
CSi80	30.8	9.01E-02	1.66E-02
CSi100	2.6	1.38E-02	1.48E-03

Considering the dimension of lysozyme is 4.5 x 3.0 x 3.0 nm^3 [34], the relevant pore size and the surface area become another factor in enhancing the adsorption performance. **Figure 3.8** shows the N_2 adsorption-desorption isotherms and pore size distribution curve of CSi80 and CSi100 to confirm the effect of the TOCN network on the macroporous of the TOCN@macroporous SiO_2 particle on the textural properties. Generally, the N_2 isotherms of all samples showed a type IV adsorption isotherm behavior with a hysteresis loop, which was accompanied by a capillary (IUPAC classification)[35]. The geometry of each prepared adsorbent was predicted based on the shape of the hysteresis loop. This type of H4 hysteresis loop usually indicates the existence of micropores due to aggregation that produces slit-shaped pores [36]. Therefore, it is predicted that slit pores exist between the parallel bundles of cellulose fibers. The slit pore size of CSi100 was observed as 2 peaks of the mesopore size distribution with radii of 2 and 12 nm (**Figure 3.9b**). Alternatively, CSi80 shows an H2 hysteresis loop above P/Po ~ 0.5 (**Figure 3.9a)**. Hysteresis loops of type H2 have more complex pore structures in which network effects are important [37]. The hysteresis loop related to capillary condensation and evaporation of N_2 was observed in a lower relative pressure range of $0.5 < P/Po < 0.9$. This was attributed to capillary condensation of nitrogen

in the mesopores and multilayer adsorption on the mesopores and macropores. The pore size distribution of CSi80 shows the wider distribution and higher intensity with the pore size peaks at 3, 4, and 16 nm. The pore volume calculation shows that CSi80 has the highest pore volume compared with CSi100. The larger pore size, broad pore size distribution, and large pore volume of CSi80 comparison to CSi100 were beneficial for lysozyme adsorption as lysozyme could easily penetrate the TOCN network into the free electrostatic site.

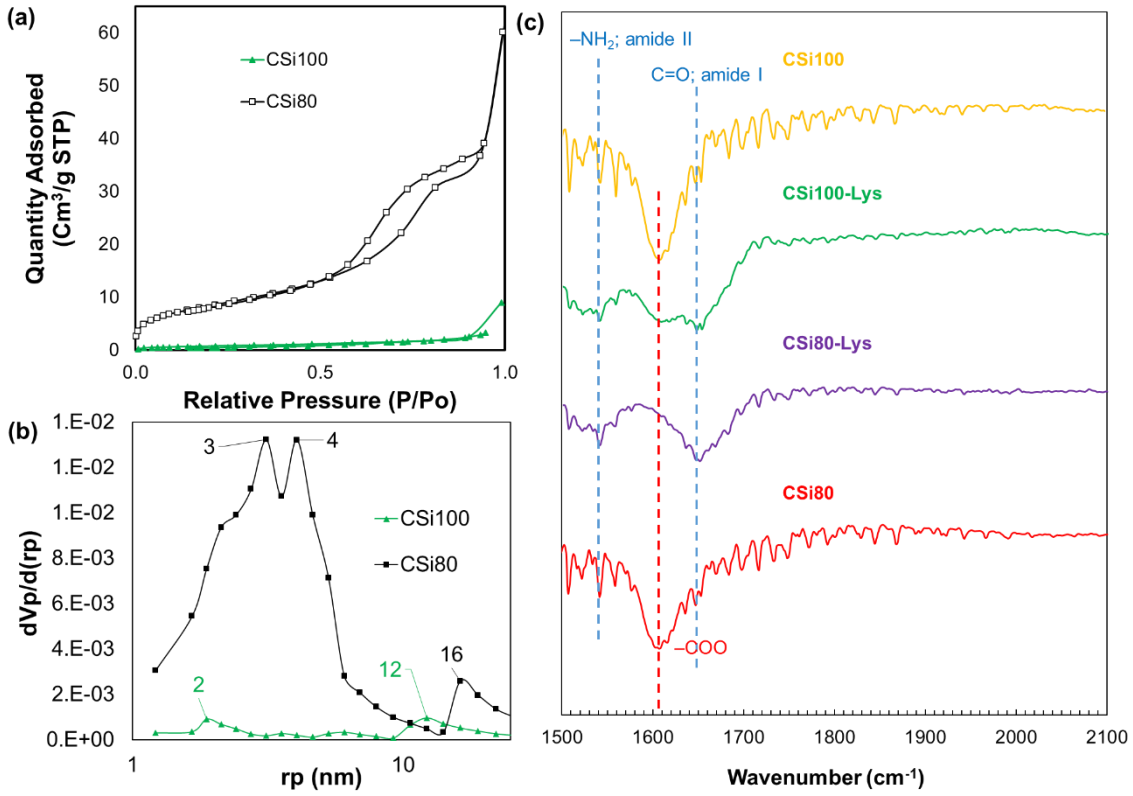

***Figure 3.9**. a) N_2 adsorption-desorption isotherms. b) Pore size distribution of CSi100, and CSi80. c) FT- IR spectra of CSi100 and CSi80 before and after adsorption.*

The FTIR spectra of CSi80 and CSi100 before and after lysozyme adsorption confirmed the effective utilization of the carboxylate site (**Figure 3.9c**). After the adsorption process, both CSi80 and CSi100 contained new peaks of amide I and II owing to lysozyme. Despite that, the carboxylate peak of CSi80 at 1606 cm^{-1} completely disappeared, while the carboxylate peak of CSi100 was reduced suggesting that there are unutilized anionic sites of CSi100 due to the dense structure of CSi100. It shows that the TOCN network on the macroporous of CSi80 enhanced adsorption capacity of adsorption through a richer site of electrostatic interaction.

In summary, the new architecture of the TOCN@macroporous SiO_2 particle increased the specific surface area, increased porous structure, required less TOCN but possessed highly-negative charge. These characteristics enhance the active sites, which leads to a relatively high and rapid protein adsorption capacity. In addition, macroporous silica could be substituted with another material that is promising for wide application such as in protein adsorption, drug delivery, and biosensors.

3.3.4 Reusability of the TOCN@macroporous SiO_2 particle

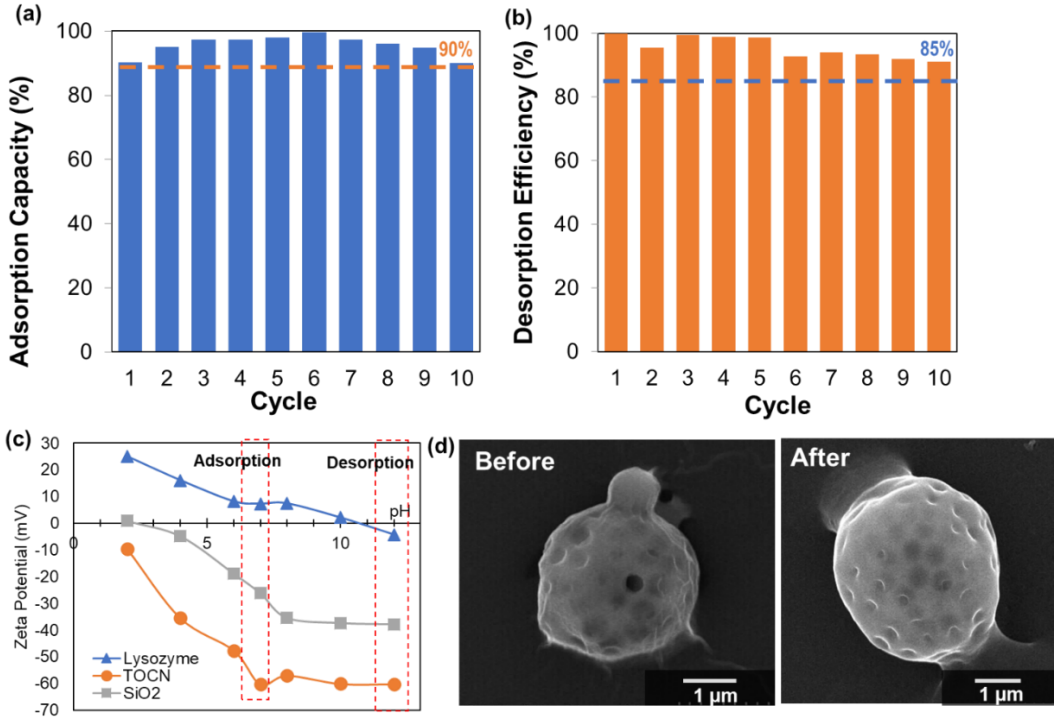

Figure 3.10. *Reusability of CSi80 on lysozyme a) adsorption capacity and b) desorption efficiency, c) Isoelectric point of lysozyme, TOCN, and the SiO_2 porous particles and d) Morphology of particle before and after reusability test*

The reusability of the TOCN@macroporous SiO_2 particle was observed via adsorption-desorption-resorption of lysozyme on CSi80, as shown in **Figure 3.10a&b**. The adsorption process was observed in pH 7 when particle has negative charge while protein has positive charge (**Figure 3.10c**). The desorption process was observed in pH 11.5 where particle and protein have negative charge. Based on the graph, the reused CSi80 increased the adsorption capacity of lysozyme after 1 cycle then slightly decrease to cycle 10 (**Figure 3.10a**). CSi80 can be used for 10 cycles with the adsorption capability of lysozyme maintained above 90%. The adsorbed lysozyme was desorbed in the base condition using

NaOH. Desorption of lysozyme was maintained above 95% and 85% after 5 and 10 cycles, respectively. Therefore, the prepared CSi80 had good reusability for lysozyme adsorption-desorption, which could be used for effective protein adsorption or drug delivery.

Table 3.4. *Comparison of different adsorbents for lysozyme adsorption*

Particle adsorbent material	**Amount of adsorbent (mg/mL)**	**C_0 (mg/mL)**	**Q_e**			
			mg/g	**%**	**Reusability**	**Ref.**
Alginate/graphene oxide	3.33	1	275	92	Good (5 cycles)	[38]
Fe_3O_4/Au-MBISA*	2	0.8	346	87	Good (7 cycles)	[39]
Porous carbon nanotube/carbon			47	32		
Activated carbon	0.67	0.1	7	5	n/a	[40]
Macroporous resin			13.3	9		
Heparin doped $CaCO_3$	20	3	88.1	59	Good (4 cycles)	[41]
Lyz-MMIPs**	1	0.4	102.4	26	Good (6 cycles)	[32]
Graphene Oxide	0.1	0.143	715	95	n/a	[24]
Mesoporous silica SBA-15	15	10	300	20	Good (6 cycles)	[42]
R-SBA-15	4	0.5	260	52	n/a	[43]
Alginate-guar gum	0.164	10	2.4	83	n/a	[44]
Chitosan/hydroxyapatite	n/a	n/a	204	94	Good (4 cycle)	[45]
MCM-41 silica particles	2	1	37	61	Good (20 cycle)	[46]
Sulphated magnetic NPs	3.3	1.5	476	90	n/a	[47]
TOCN/Silica (CSi80)	**0.2**	**0.4**	**1865**	**93**	**Good (10 cycles)**	**This Study**

* 2-mercapto-5-benzimidazolesulfonic acid

** lysozyme-based magnetic molecularly imprinted polymers

Table 3.4 summarizes the adsorption properties of several types of adsorbents in the lysozyme adsorption process. Alginate/graphene oxide is a good candidate due to their high adsorption capacity and good reusability. The adsorption capacity of a reported carbon nanotube/carbon composite is also more effective than activated carbon and resin. On the other hand, among the adsorbents, the adsorption capacity of CSi80 was much greater than previous adsorbents. CSi80 has the highest adsorption capacity with the amount of lysozyme is two times higher than adsorbent. The outstanding performances of CSi80 could be attributed to the electrostatic interaction by exchange or sharing of electron between the silanol and carboxyl functional groups of CSi80 and cationic lysozyme. In addition, CSi80 has a higher cycle of reusability than the previous adsorbent. In the application of separation, adsorption, and other works in the fluid system, the reusability is extremely important in order to reduce the maintenance and compensate for their manufacturing expense.

3.4 Conclusion

TOCN@macroporous SiO_2 particles were synthesized by loading TOCN on the surface of a porous silica particle. The highly-negative charge and rich carboxyl groups of TOCN render the particles effective as a protein adsorbent. The loading amount of TOCN was varied to observe property trends. Pure TOCN, pure porous silica, and commercial cellulose beads were used for adsorption comparison. The TOCN@macroporous SiO_2 particle had a similar functional group, similar zeta potential, yet higher surface area than that of pure TOCN. As a result, the TOCN@macroporous SiO_2 particle had high adsorption capacity, rapid adsorption, good reusability, and good release of the adsorbate. The results suggest the potential for TOCN@macroporous SiO_2 particles in drug delivery, protein adsorption, and other applications in the biomedical field.

3.5 References

[1] F.P. Roudsari, M.R. Mehrnia, H. Kaghazian, Towards rational design of porous nanostructured biopolymeric microparticles for biomacromolecules separation: A case study of intraparticle diffusion facilitation and BSA adsorption on agarose microspheres, Mater. Sci. Eng. C. 93 (2018) 518–528.

[2] S. Mei, P. Han, H. Wu, J. Shi, L. Tang, Z. Jiang, One-pot fabrication of chitin-shellac composite microspheres for efficient enzyme immobilization, J. Biotechnol. 266 (2018) 1–8.

[3] G. Bayramoglu, C. Ozalp, M. Oztekin, U. Guler, B. Salih, M.Y. Arica, Design of an aptamer-based magnetic adsorbent and biosensor systems for selective and sensitive separation and detection of thrombin, Talanta. 191 (2019) 59–66.

[4] T. Kawai, K. Saito, W. Lee, Protein binding to polymer brush, based on ion-exchange, hydrophobic, and affinity interactions, J. Chromatogr. B Anal. Technol. Biomed. Life Sci. 790 (2003) 131–142.

[5] S. Patil, A. Sandberg, E. Heckert, W. Self, S. Seal, Protein adsorption and cellular uptake of cerium oxide nanoparticles as a function of zeta potential, Biomaterials. 28 (2007) 4600–4607.

[6] S. V. Patwardhan, F.S. Emami, R.J. Berry, S.E. Jones, R.R. Naik, O. Deschaume, H. Heinz, C.C. Perry, Chemistry of aqueous silica nanoparticle surfaces and the mechanism of selective peptide adsorption, J. Am. Chem. Soc. 134 (2012) 6244–6256.

[7] X. Zeng, E. Ruckenstein, Membrane chromatography : preparation and applications to protein separation, Biotechnol. Prog. 15 (1999) 1003–1019.

[8] S.R. Dods, O. Hardick, B. Stevens, D.G. Bracewell, Fabricating electrospun cellulose nanofibre adsorbents for ion-exchange chromatography, J. Chromatogr. A. 1376 (2015) 74–83.

[9] R. Balgis, H. Murata, Y. Goi, T. Ogi, K. Okuyama, L. Bao, Synthesis of dual-size cellulose-polyvinylpyrrolidone nanofiber composites via one-step electrospinning method for high-performance air filter, Langmuir. 33 (2017) 6127–6234.

[10] T. Saito, A. Isogai, TEMPO-mediated oxidation of native cellulose. The effect of oxidation conditions on chemical and crystal structures of the water-insoluble fractions, Biomacromolecules. 5 (2004) 1983–1989.

[11] T. Saito, Y. Nishiyama, J.L. Putaux, M. Vignon, A. Isogai, Homogeneous suspensions of individualized microfibrils from TEMPO-catalyzed oxidation of native cellulose, Biomacromolecules. 7 (2006) 1687–1691.

[12] T. Saito, S. Kimura, Y. Nishiyama, A. Isogai, Cellulose nanofibers prepared by TEMPO-mediated oxidation of native cellulose, Biomacromolecules. 8 (2007) 2485–2491.

[13] R. Ning, M. Takeuchi, J.M. Lin, T. Saito, A. Isogai, Influence of the morphology of zinc oxide nanoparticles on the properties of zinc oxide/nanocellulose composite films, React. Funct. Polym. 131 (2018) 293–298.

[14] Y. Zhou, T. Saito, L. Bergström, A. Isogai, Acid-free preparation of cellulose nanocrystals by TEMPO oxidation and subsequent cavitation, Biomacromolecules. 19 (2018) 633–639.

[15] N. Isobe, X. Chen, U.J. Kim, S. Kimura, M. Wada, T. Saito, A. Isogai, TEMPO-oxidized cellulose hydrogel as a high-capacity and reusable heavy metal ion adsorbent, J. Hazard. Mater. 260 (2013) 195–201.

[16] H. Ma, B.S. Hsiao, B. Chu, Ultrafine cellulose nanofibers as efficient adsorbents for removal of UO_2^{2+} in water, ACS Macro Lett. 1 (2012) 213–216.

[17] Y. Peng, D.J. Gardner, Y. Han, Drying cellulose nanofibrils: in search of a suitable method, Cellulose. 19 (2012) 91–102.

[18] X. Zheng, S. Fu, Reconstructing micro/nano hierarchical structures particle with nanocellulose for superhydrophobic coatings, Colloids Surfaces A Physicochem. Eng. Asp. 560 (2019) 171–179.

[19] GRN No. 321, (n.d.). https://www.accessdata.fda.gov/scripts/fdcc/index.cfm?set=GrASNotices&id=321 (accessed January 7, 2019).

[20] T. Çamli, M. Tuncel, S. Şenel, A. Tuncel, Functional, uniform, and macroporous latex particles: Preparation, electron microscopic characterization, and nonspecific protein adsorption properties, J. Appl. Polym. Sci. 84 (2002) 414-429.

[21] Z. Sun, Y. Deng, J. Wei, D. Gu, B. Tu, D. Zhao, Hierarchically ordered macro-/mesoporous silica monolith: Tuning macropore entrance size for size-selective adsorption of proteins, Chem. Mater. 23 (2011) 2176–2184.

[22] Y. Tao, E.X.P. Almodovar, G. Carta, G. Ferreira, D. Robbins, Adsorption kinetics of deamidated antibody variants on macroporous and dextran-grafted cation exchangers. III. Microscopic studies, J. Chromatogr. A. 1218 (2011) 8027-8035.

[23] M.C. Giuffrida, G. Cigliana, G. Spoto, Ultrasensitive detection of lysozyme in droplet-based microfluidic devices, Biosens. Bioelectron. 104 (2018) 8–14.

[24] S. Li, J.J. Mulloor, L. Wang, Y. Ji, C.J. Mulloor, M. Micic, J. Orbulescu, R.M. Leblanc, Strong and selective adsorption of lysozyme on graphene oxide, ACS Appl. Mater. Interfaces. 6 (2014) 5704–5712.

[25] J.Y. Lin, B.X. Wang, Room-temperature voltage stressing effects on resistive switching of conductive-bridging RAM cells with Cu-doped SiO_2 films, Adv. Mater. Sci. Eng. 2014 (2014) 1–6.

[26] H. Chen, Y. Wang, Y. Wang, S. Dong, E. Wang, One-step preparation and characterization of PDDA-protected gold nanoparticles, Polymer (Guildf). 47 (2006) 763–766.

[27] B.H.X. Che, S.P. Yeap, A.L. Ahmad, J.K. Lim, Layer-by-layer assembly of iron oxide magnetic nanoparticles decorated silica colloid for water remediation, Chem. Eng. J. 243 (2014) 68-78.

[28] B. Soni, E.B. Hassan, B. Mahmoud, Chemical isolation and characterization of different cellulose nanofibers from cotton stalks, Carbohydr. Polym. 134 (2015) 581–589.

[29] A. Bernkop-Schnürch, S. Krist, M. Vehabovic, C. Valenta, Synthesis and evaluation of lysozyme derivatives exhibiting an enhanced antimicrobial action, Eur. J. Pharm. Sci. 6 (1998) 301–306.

[30] CellufineTM MAX CM, (n.d.). https://www.jnc-corp.co.jp/fine/jp/cellufine/guide/pdf/ion_max/INST_MAX-CM_IN041_V3_1_EN_20170524.pdf (accessed January 17, 2019).

[31] H.-J. Kang, J.-H. Kim, Adsorption Kinetics, Mechanism, Isotherm, and Thermodynamic Analysis of Paclitaxel from Extracts of Taxus chinensis Cell Cultures onto Sylopute, Biotechnol. Bioprocess Eng. 24 (2019) 513–521.

[32] Z. Zhang, H. Wang, H. Wang, C. Wu, M. Li, L. Li, Fabrication and evaluation of molecularly imprinted magnetic nanoparticles for selective recognition and magnetic separation of lysozyme in human urine, Analyst. 143 (2018) 5849–5856.

[33] D. Saikia, J.R. Deka, C.E. Wu, Y.C. Yang, H.M. Kao, pH responsive selective protein adsorption by carboxylic acid functionalized large pore mesoporous silica nanoparticles SBA-1, Mater. Sci. Eng. C. 94 (2019) 344–356.

[34] J.R. Deka, D. Saikia, Y.S. Lai, C.H. Tsai, W.C. Chang, H.M. Kao, Roles of

nanostructures and carboxylic acid functionalization of ordered cubic mesoporous silicas in lysozyme immobilization, Microporous Mesoporous Mater. 213 (2015) 150–160.

[35] T. Sing, K. S. W.; Everett, D. H.; Haul, R. A. W.; Moscou, L.; Pierotti, R. A.; Rouquerol, J.; Siemieniewska, Reporting physisorption data for gas/solid systems with special reference to the determination of surface area and porosity, Pure Appl. Chem. 57 (1985) 603–619.

[36] K.S.W. Sing, R.T. Williams, Physisorption hysteresis loops and the characterization of nanoporous materials, Adsorpt. Sci. Technol. 22 (2004) 773–782.

[37] F. Rouquerol, J. Rouquerol, K. Sing, Adsorption by powders and porous solids: principles, methodology and applications, Academic Press, London, 1999.

[38] J. Li, J. Ma, S. Chen, Y. Huang, J. He, Adsorption of lysozyme by alginate/graphene oxide composite beads with enhanced stability and mechanical property, Mater. Sci. Eng. C. 89 (2018) 25–32.

[39] X. Zhu, L. Zhang, A. Fu, H. Yuan, Efficient purification of lysozyme from egg white by 2-mercapto-5-benzimidazolesulfonic acid modified Fe_3O_4 /Au nanoparticles, Mater. Sci. Eng. C. 59 (2016) 213–217.

[40] J. Bai, Y. Huang, Q. Gong, X. Liu, Y. Li, J. Gan, M. Zhao, Y. Shao, D. Zhuang, J. Liang, Preparation of porous carbon nanotube/carbon composite spheres and their adsorption properties, Carbon N. Y. 137 (2018) 493–501.

[41] P. Shi, J. Qin, J. Hu, Y. Bai, X. Zan, Insight into the mechanism and factors on encapsulating basic model protein, lysozyme, into heparin doped $CaCO_3$, Colloids Surfaces B Biointerfaces. 175 (2019) 184–194.

[42] W. Chen, S.J. Park, F. Kong, X. Li, H. Yang, J.Y.Y. Heng, High protein-loading silica template for heterogeneous protein crystallization, Cryst. Growth Des. 20 (2020) 866-873.

[43] S. Sun, S. Wang, P. Wang, Q. Wu, S. Fang, Ultrasound assisted morphological control of mesoporous silica with improved lysozyme adsorption, Ultrason. Sonochem. 23 (2015) 21-25.

[44] M.E. Brassesco, N. Woitovich Valetti, G. Picó, Molecular mechanism of lysozyme

adsorption onto chemically modified alginate guar gum matrix, Int. J. Biol. Macromol. 96 (2017) 111–117.

[45] J. Sun, L. Wu, J. Chen, Efficient lysozyme adsorption on chitosan/hydroxyapatite hybrid membrane via in situ synthesis, Cellulose. 23 (2016) 3861-3874.

[46] G. Bayramoglu, V.C. Ozalp, M. Yilmaz, U. Guler, B. Salih, M.Y. Arica, Lysozyme specific aptamer immobilized MCM-41 silicate for single-step purification and quartz crystal microbalance (QCM)-based determination of lysozyme from chicken egg white, Microporous Mesoporous Mater. 207 (2015) 95-104.

[47] J. Chen, Y. Lin, L. Jia, Preparation of anionic polyelectrolyte modified magnetic nanoparticles for rapid and efficient separation of lysozyme from egg white, J. Chromatogr. A. 1388 (2015) 43-51.

Chapter 4

Effect of silica macropore size fitted with the length of TOCN on protein adsorption

4.1 Introduction

In the chapter 3, we successfully demonstrated for the first time TEMPO-oxidized cellulose nanofibers (TOCN) as an anionic polymer decorated macroporous silica (TOCN@macroporous SiO_2) particles for protein adsorption [1]. Combined advantages of fast adsorption equilibrium from TOCN and a high degree of accessibility, derived from the macroporous silica, resulted in a unique structure exhibiting outstanding adsorption performance and excellent reusability with high adsorption and desorption capacities. However, the exact mechanism underlying how TOCN is decorated on porous structures and the resulting performance from interface interaction with protein still requires circumventing.

Different from other polymers, TOCN exhibits a high aspect ratio and not soluble in water or most of the organic solvents. So that, the loading process is dependent on the pore size of the substrate. TOCN is well individually dispersed in water (wet-state) due to high negative charged [2,3] that we expect that TOCN can independently penetrate the appropriate pore size and finally form a network in the drying process. Therefore, tuning the silica macropore size in the presence of TOCN *via* smart and rational design is highly desired. In this chapter, macroporous silica particles of varying pore sizes were used to obtain the optimum macropore size for the desired TOCN loading and concomitantly, to understand how protein diffusion reaching the active sites is influenced. Since the highly negative zeta potential, surface area and pore size distribution are important factor in the adsorption process, in this chapter we observed the aforementioned characteristics on TOCN@macroporous SiO_2 particles.

In addition, an adequate description of the adsorption driving forces of protein on TOCN@macroporous SiO_2 particles is still lacking. Gaining a better understanding of the interactions driving the adsorption is fundamental to produce improved adsorbents for ion-exchange applications and other biomedical application. In the previous research, the driving forces towards cellulose based materials have been carried out using thermodynamics of adsorption. However, mostly of them focused on the removal of heavy metal ions and organic pollutants [4,5]. In particular, the thermodynamics of adsorption gives information

about the spontaneity, the driving force, and the direction of the process, as well as an indication on the strength of the interactions. Therefore, this chapter allowed elucidation of adsorption kinetics, thermodynamics, and isotherm parameters to understand the driving force of lysozyme adsorption on TOCN@macroporous SiO_2 particles as a function of the host structure.

4.2 Experimental

4.2.1. Synthesis of TOCN-decorated macroporous silica (TOCN-MPS) particles

Herein, three types of TOCN-MPS particles—TOCN-MPS-X (*X* = macropore size of 100, 300, or 500 nm)—were prepared *via* a spray pyrolysis method followed by a TOCN loading process. As a comparison, cellulose nanofiber-loaded dense silica (TOCN-DS) particles were also prepared to clarify the effectiveness of the macroporous structure. **Figure 4.1** shows the process diagram for the preparation of TOCN-MPS particles. First, macroporous silica (MPS) particles were prepared from tetraethyl ortho-silicate (TEOS, 99.9%, Sigma-Aldrich, St. Louis, MO, USA) as the silica source. Nitric acid (HNO_3, 60%, 0.1 M, Kanto Chemical Co, Inc., Japan) was used as the catalyst, and polymethyl methacrylate (PMMA, Sekisui Plastics Co., Ltd., Tokyo, Japan) particles functioned as the template for macroporous formation. Deionized water was used as the solvent. Dense silica (DS) particles were prepared with the same condition as MPS particles but without PMMA particles. Detailed precursor conditions and characteristics of DS and MPS particles are indicated in **Table 4.1**. The precursors were sprayed using an ultrasonic nebulizer as an atomizer through a tubular furnace with four stacked temperature zones using N_2 as the carrier gas. A detailed spray pyrolysis experimental set-up was similar to that previously described [6–9]. The surface charge of the collected MPS particles were thereafter adjusted from negative to positive (**Figure 4.1**) by stirring in a 1 wt.% poly(diallyldimethylammonium chloride) (PDDA, MW = 100,000–200,000, Sigma-Aldrich) solution having a MPS/PDDA mass ratio of 1/2. After stirring for 30 min at room temperature and washing two times, the positively-charged MPS particles were obtained as indicated in **Table 4.1**. Thereafter, as illustrated in **Figure 4.1**, the TOCN was loaded onto the MPS particles by dispersing the positively-charged MPS particles in a 0.1 wt.% TOCN (TEMPO-oxidized cellulose nanofiber, DKS Co., Ltd., Japan) aqueous solution with a TOCN/MPS mass ratio of 3/2. The TOCN dimensions used in this research are 100–300 nm (length) and 3–4 nm (width) with a corresponding zeta potential value of −59 ± 2 mV. The

mixing solution was stirred for 2 hr at 800 rpm and 50 °C. Next, the TOCN-MPS particles were collected following a spray-drying process at 180 °C.

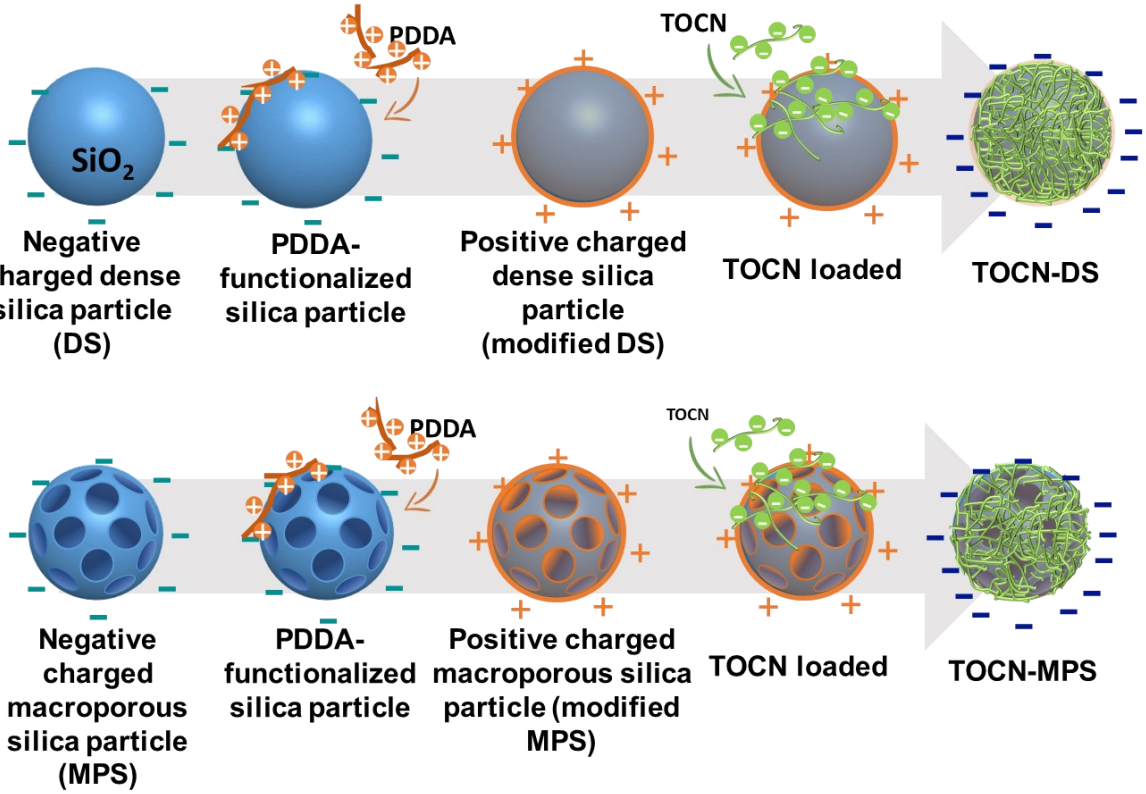

***Figure 4.1**. (a) Process diagram that illustrates the preparation of cellulose nanofiber-loaded macroporous silica (TOCN-MPS).*

4.2.2 Lysozyme adsorption properties

All adsorption performances were investigated using lysozyme (MP Biomedicals, Solon, OH) as the targeted model molecule. Regarding the measurement of adsorbed lysozyme under equilibrium conditions (Qe, mg/g), 10 mg lysozyme was dispersed in 49 mL of water to which 1 mL of a buffer phosphate solution, pH 7, was added. Thereafter, 5 mg of TOCN-MPS particles were added and stirred for 2 hr prior to being centrifuged at 15,000 rpm for 5 min. The supernatant analyzed using a UV Vis spectrophotometer (UV-3150, Shimadzu, Japan) with a wavelength from 240–400 nm at room temperature. The absorbance intensity, which indicates lysozyme concentration, was measured at 281 nm.

To understand the adsorption process mechanism of the TOCN-MPS particles, kinetic, isothermal, and thermodynamic parameter calculations were employed. The feasibility and the diffusion rate of the adsorption process were evaluated using pseudo-first-

order (PFO), pseudo-second-order (PSO), and the Weber-Morris model. The calculation was obtained by measuring the adsorption capacities at equilibrium (*Qe*, mg/g) and at time t (*Qt*, mg/g) from 0–2 hr. The thermodynamic parameters were observed to predict the spontaneous adsorption process by varying the adsorption temperature. The temperature was variated between 25, 30, 40, and 50 °C, with the lysozyme concentration, C_0 = 200 mg/L, at pH 7 and 2 hr contact time. To explore the interaction between lysozyme and TOCN-MPS, isothermal parameters (Langmuir, Freundlich, Temkin, Redlich-Peterson (R-P), Sips, Koble-Corrigan (K-C), and Toth models) were calculated by varying C_0 (C_0 = 20, 50, 100, 200, 400, and 800 mg/L). The adsorptions were conducted at 25°C, pH 7, and at an adsorbent dosage of 100 mg/L. The optimum adsorption model was determined by the error of analysis value (R^2). All the adsorption performances and characteristics were performed at least three times and averaged.

4.2.3. Characterization.

Scanning electron microscopy (SEM) (S-5000, Hitachi Ltd., Tokyo, Japan) was used to investigate the morphology of the products. Dynamic light scattering (DLS) with a ZS nano analyzer (Malvern Instrument Inc., London, U.K.) was used to examine the size distribution and ζ- potential of the particles. Characterization of the functional groups was determined using FT-IR spectroscopy (IRAffinity-1S, Shimadzu). Thermogravimetric analysis (TGA-50/50H, Shimadzu Corp., Kyoto, Japan) was used to determine the loading amount of PDDA and TOCN. The surface area was determined quantitatively by N_2 adsorption-desorption (BELSORP-max, BEL Japan, Osaka, Japan) using the Brunauer–Emmett–Teller (BET) method. The pores distribution was determined by the Barrett–Joyner–Halenda (BJH) method.

Table 4.1. *Synthesis of macroporous SiO_2 particles via spray pyrolysis.*

Sample name	Precursor for spray pyrolysis[a]				MPS			Modified MPS	
	TEOS (M)	PMMA (wt.%)	Template size (nm)	Total solution (mL)	Particle size (μm)[b]	Pore size (nm)[c]	ζ-potential (mV)[b]	PDDA loading amount (mg/mg)[d]	ζ-potential (mV)[b]
DS	0.4	-	-	100	1.2	-	−36.7	0.025	36.9
MPS 100	0.4	10	100	100	1.4	75 ± 3	−37.2	0.089	30.2
MPS 300	0.4	10	300	100	1.0	237 ± 7	−38.6	0.067	32.7
MPS 500	0.4	10	500	100	1.1	436 ± 11	−37.7	0.045	34.2

Table 4.2*. Synthesis of cellulose nanofiber-loaded macroporous SiO_2 (TOCN-MPS) particles*

Sample name	Precursor			Product			
	Modified DS or MPS (wt.%)	TOCN (wt.%)	Total solution (mL)	TOCN loading amount[d] (mg/mg)	ζ-potential[b] (mV)	SSA_{BET}[e] (m^2/g)	Total pore volume[e] (cm^3/g)
TOCN-DS	0.06	0.1	100	0.583	−59.6	2.86	0.042
TOCN-MPS 100	0.06	0.1	100	0.583	−59.7	6.67	0.043
TOCN-MPS 300	0.06	0.1	100	0.554	−59.4	9.12	0.087
TOCN-MPS 500	0.06	0.1	100	0.572	−59.8	4.55	0.023
TOCN	-	0.1	100	1.000	−59.0	3.29	0.017

a) Spray pyrolysis conditions:
Furnace temperature : four stacked temperature zones set to 150, 350, 500, and 500 °C
Atomizer : ultrasonic nebulizer, 0.8 MHz
Carrier gas : N_2 (1 mL/min)

b) Calculated by DLS analysis.

c) Estimated by calculation of 200 pore sizes in SEM images.

d) Calculated by weight loss in TG analysis

e) SSA_{BET} and total pore volume are calculated by the BET method

4.3 Results and Discussion

4.3.1 Characteristics of silica/TOCN particles

The representative SEM micrographs of the MPS and TOCN-MPS particles are shown in **Figure 4.2 a–d**. Initially, prior to the addition of TOCN, all DS and MPS particles (**Figure 4.2 a0–d0**) exhibit a spherical form with a dense or macroporous structure following the size of the templates (100, 300, and 500 nm). However, the average final macropore size of the silica is not the same as the template size as a result of shrinkage during the drying and template removal processes [10,11].

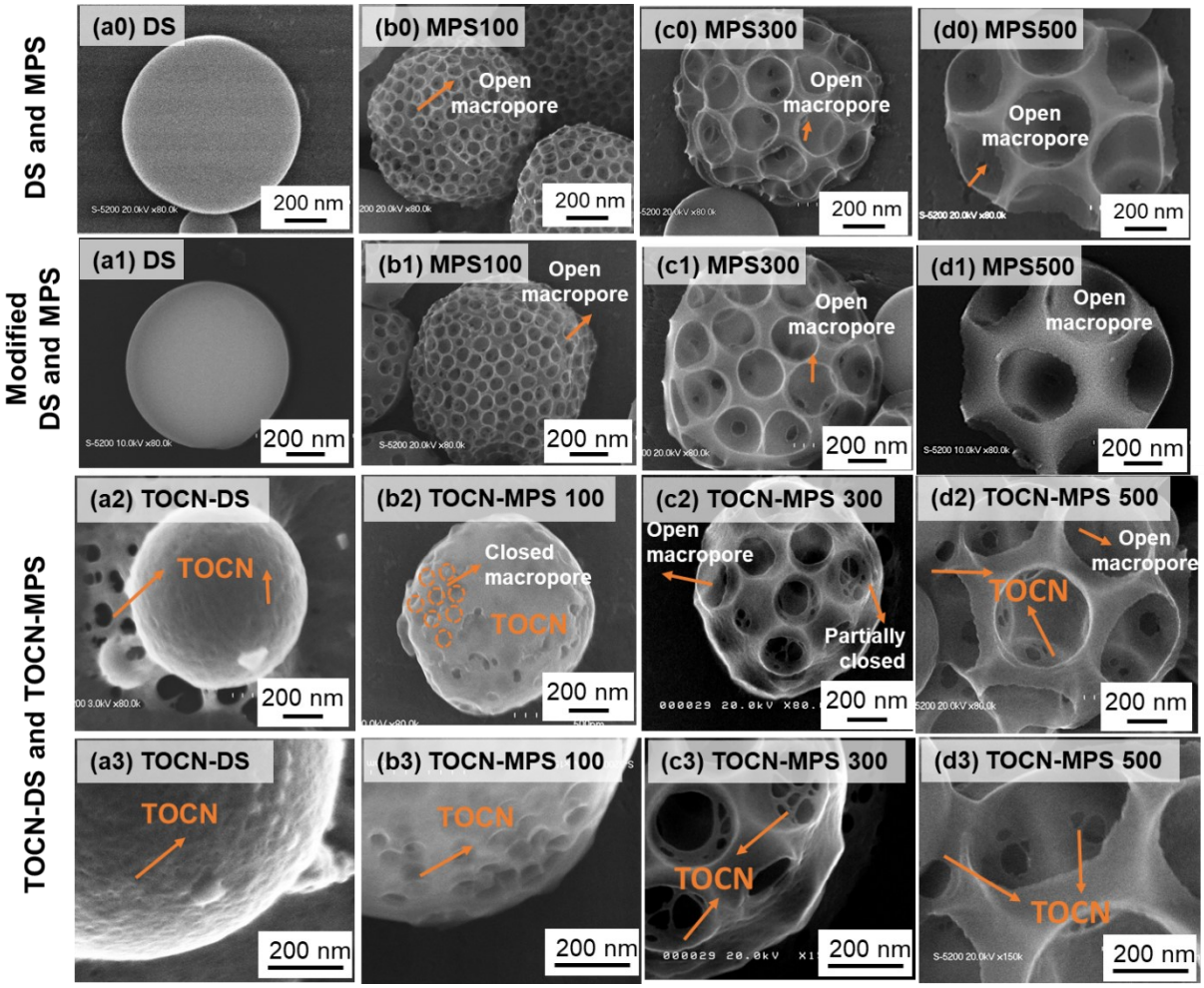

Figure 4.2. *SEM images of DS and MPS particles before (a0–d0) and after modification (a1–d1). SEM micrographs of TOCN-DS and TOCN-MPS particles (a2–d2) and high magnification images (a3–d3).*

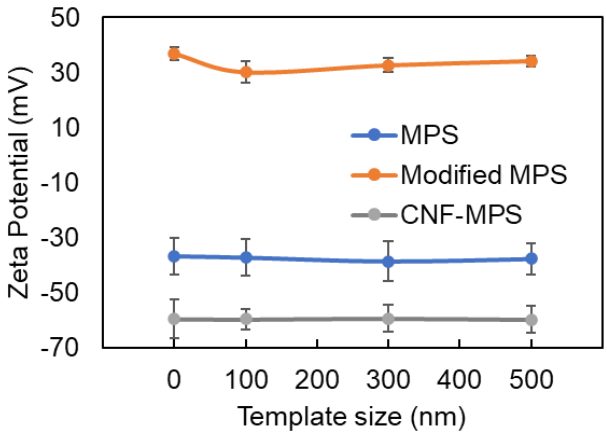

Figure 4.3 *(a) Zeta potential of MPS, modified MPS, and TOCN-MPS particles. The template size 0 nm indicates DS particles.*

The final macropore size of the 'MPS 100' particles are 75 nm, which is smaller than the TOCN length. The 'MPS 300' particles have a final pore size of 237 nm, which is a similar size as the TOCN length. While the 'MPS 500' particles have a pore size of 436 nm, that is larger than the TOCN length. After PDDA deposition (**Figure 4.2 a1–d1**), the modified DS and MPS particles exhibited the same morphology as observed prior to the modification; that is, the particles still retained a spherical form with dense and open macroporous structures. Even so, the change of zeta potential from negative (−37~−38 mV) to positive (30~34 mV) was confirmed for all of the samples, as indicated in **Figure 4.3a** and **Table 4.1**. The morphology of the DS and MPS particles changed after TOCN loading. In the TOCN-DS particles, the DS particle surface was observed to be covered with a tight TOCN network (**Figure 4.2 a2–a3**). From **Figure 4.2 a2–d2**, the TOCN network appeared to become thinner as a function of increasing macropore size. The 'MPS 100' particles, which initially exhibited numerous open macropores, became almost closed after TOCN loading (**Figure 4.2b**). Conversely, the macropore size of the 'MPS 300' particles were only partially covered by TOCN (**Figure 4.2c**), while the macropores of the 'MPS 500' particles were not covered at all (**Figure 4.2d**). Although, the TOCN network is observed to be stretched across the surface of the interconnected channels (**Figure 4.2d3**). However, all particles have a similar TOCN loading amount (**Table 4.2**) and possess a high negative charge (−59.4~−59.8 mV) similar to the zeta potential of TOCN.

4.3.2. TOCN deposition on macroporous structure

The SSA of the MPS and DS particles were measured before and after the addition of TOCN (**Figure 4.4**). Interestingly, the 'TOCN-MPS 300' particles exhibit the highest SSA. Whereas, prior to the TOCN loading, the 'MPS 100' particles displayed the highest SSA.

These results indicate that the MPS macropore size influenced the characteristics of the TOCN-MPS particles.

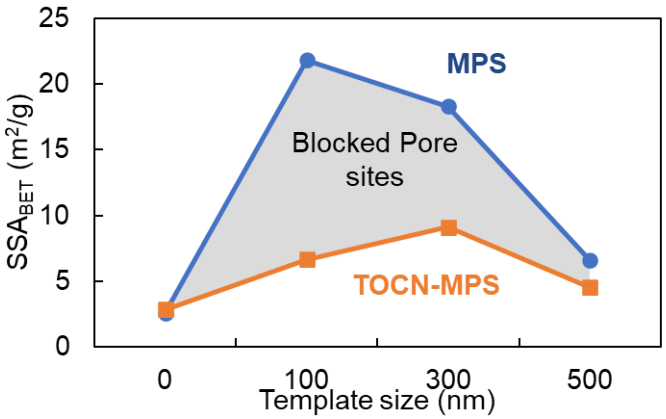

Figure 4.4 *SSA of MPS and TOCN-MPS particles. The template size 0 nm indicates DS particles.*

The mechanism of the TOCN deposition is suggested to depend on the macropore size of the MPS particles, as shown in **Figure 4.5a**. TOCN has a high aspect ratio (>30) and it is insoluble in water. Hence, the loading process of TOCN onto the particles requires a surface to attach to. Once the particles come into contact with TOCN in the system, the surface of the particle skeleton is the outer surface that interacts with TOCN. For TOCN-DS, the silica possesses a dense morphology, which means that the entire surface can be used to attach TOCN. Thus, a tight TOCN network is formed on the surface of the dense silica, as shown in **Figure 4.2 (a2–a3) a**s illustrated in **Figure 4.5a.** A similar phenomenon also occurred in the 'TOCN-MPS 100' particles. The macropores of the 'MPS 100' particles that were initially opened became almost closed after TOCN loading (**Figure 4.2 b2–b3**), as a result of the 'MPS 100' macropore size being smaller than the TOCN length. Hence, the addition of TOCN attaches to the skeleton surface between the macropores, which eventually closed the macropore, as illustrated in **Figure 4.5a**. Initially, the 'MPS 100' particles possess the highest SSA comprising numerous macropores between 68–78 nm and several mesopores, which may derive from the interconnected channel size. However, this closed macropore results in hindered access to the interconnected channels inside of the porous particles, indicated by the significantly decreasing surface area, as shown in **Figure 4.4**.

Different phenomena are observed for the 'TOCN-MPS 300' particles. Only the partially open macroporous structure was covered by the TOCN networks (**Figure 4.2 c2–c3**). Because the size of the macropore (273 nm) is within the range of the TOCN length (100~300 nm), open macropores with some fibers attached inside the macroporous surface are observed. When the TOCN is larger, the attachment is to the skeleton surface between

the macropores, which induces a TOCN network across the macroporous external surface. While the smaller TOCN can insert and become attached to the inner surface of the macropores. In the 'TOCN-MPS 500' case, since the length of the TOCN is smaller than the pore size of 'TOCN-MPS 500', besides being loaded onto the skeleton, the majority of the TOCN is also contained inside the macropores. The TOCN location is evidenced by the presence of a TOCN network stretched at interconnecting pore channels, as shown in **Figure 4.2 d3**.

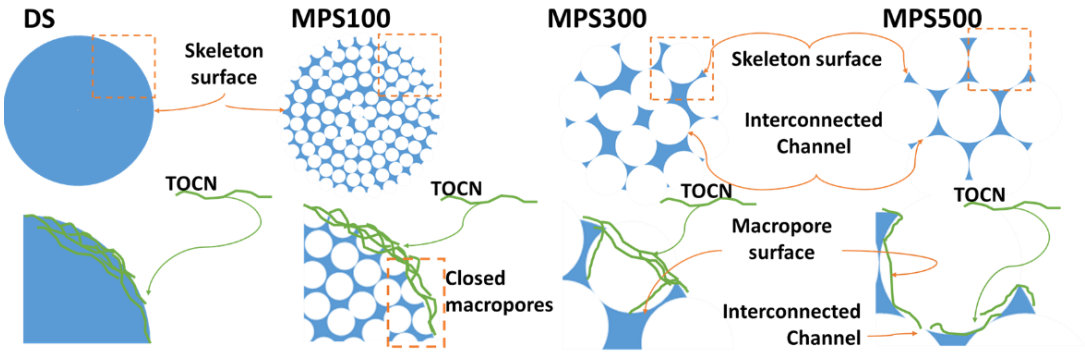

Figure 4.5. *The mechanism of the TOCN deposition.*

4.3.3. Protein adsorption performance: Thermodynamic analyses

It has been known that zeta potential plays an essential role in the adsorption process because of the electrostatic force that attracts selective molecules to the adsorbent surface.[12–14] However, if engineered porous materials can be developed by coordinating meso-macroporous particles and functionalized polymers, the adsorption process is expected to be significantly enhanced. By considering this strategy, a TOCN-MPS particle for protein adsorption was proposed having the following optimized adsorbent criteria: (1) a high degree of surface-functionalized carboxylation groups that are highly negatively-charged for effective adsorption; (2) high surface area and high pore volume with a large number of mesopores for efficient adsorption; and (3) open and interconnected macroporous channels within a desired particle size range to allow efficient ingress of both small and large molecules.

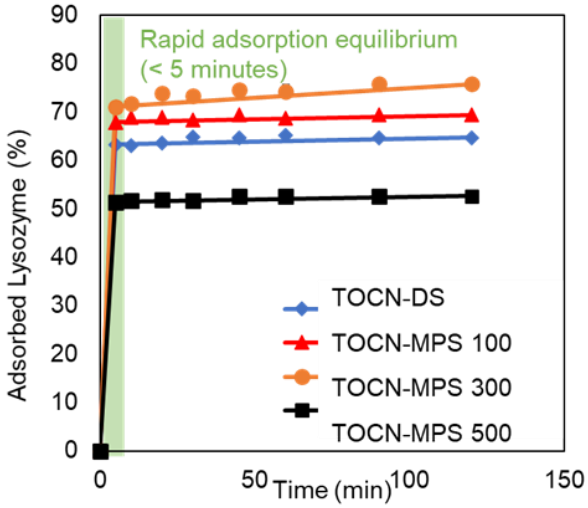

Figure 4.6. *Adsorption ratio of lysozyme as a function of time with the following conditions: initial lysozyme concentration: 200 mg/L; dosage of adsorbent: 100 mg/L; pH: 7; and equilibrium time: 2 hr.*

The first criteria can be satisfied by selecting a TEMPO-oxidized cellulose nanofiber as the functionalized polymer surface because of the high degree of carboxylate groups and negative zeta potential. As a result, all TOCN-MPS particles used in this study exhibit high negative zeta potentials that resemble the actual TOCN charge, which suggests an effective adsorption process. As proven in **Figure 4.6** and **Table 4.2**, all particles can adsorb lysozyme in significant quantities (>1,000 mg/g) within 5 min. Undeniably, these results demonstrate the potential of the TOCN-MPS particles as an up-and-coming system for adsorbing large molecules over a short period of time. The data suggest that TOCN-MPS contains abundant and accessible binding sites that lead to a high adsorption rate of lysozyme over a short period of time.

The thermodynamic parameters such as the changes in free energy (ΔG°), enthalpy (ΔH°), and entropy (ΔS°) were calculated by the Van't Hoff equation to understand the forces behind self-organization and co-organization of the TOCN-MPS particles with lysozyme.

$$\Delta_{ads}G^0 = \Delta_{ads}H^0 - T\Delta_{ads}S^0 \quad 4.8$$

$$K = \frac{Q_e}{C_e} \quad 4.9$$

The linear Van't Hoff plot:

$$lnK = \frac{\Delta_{ads}S^0}{R} - \frac{\Delta_{ads}H^0}{RT} \quad 4.10$$

where *K is the equilibrium constant, $\Delta_{ads}H°$ (kJ/mol) is the enthalpy change, $\Delta_{ads}S°$ (J/mol·K) is the entropy change, $\Delta_{ads}G°$ (kJ/mol) is the Gibbs free energy, R* is the ideal gas constant 8.314 (J mol^{-1} K^{-1}) and T is the temperature (K). From plotting ln *K vs 1/T,* the value of *$\Delta_{ads}S°$ can be calculated from the intercept, and $\Delta_{ads}H°$ from the slope of equation 4.3. The value of $\Delta_{ads}G°$ can be calculated from equation 4.1.* In order for the protein adsorption to occur spontaneously, *$\Delta_{ads}G°$* must be a negative number. Therefore, the *$\Delta_{ads}H°$ must be a small value or $\Delta_{ads}S°$ is big value.*

Table 4.3 *Thermodynamic parameter comparisons of various lysozyme adsorbents.*

	(°C)	**Δ*S*°**	**Δ*H*°**	**Δ*G*°**	***Qe* (mg/g)**	**t_e[a] (min)**	**Ref.**
TOCN-MPS 300	25	0.25	−64.63	−140.61	1,516	5	This study
PGMA-Heparin	25	54.27	−1.0	−17.18	654	240	[16]
Colloidal silica particle	70	1.24	448	22.5	n/a	n/a	[17]
Polyacrylamide cryogel	35	2.24	−12.6	−14.9	363	n/a	[18]
Mesostructured cellular Foam (MCF) silica	25	−0.043	−48.6	−35.9	226	n/a	[19]
Gold NPs	25	12.5	−57.8	−63.6	n/a	n/a	[20]

a Time needed to reach equilibrium adsorption

The thermodynamic values, as presented in **Table 4.3**, show an exothermic enthalpy and a positive change in entropy upon adsorption. The favorable exothermic enthalpy is mostly attributed to chemisorption process. The physical adsorption could be observed in the enthalpy range between -20 to -40 kJ/ mol, while the chemisorption is between -400 and -80 kJ/mol. The chemisorption could be occurred trough the formation of electrostatic interaction and hydrogen bonds and aromatic stacking interactions on the hydrophobic face of crystalline cellulose.[15] The positive entropy suggests a dominance of the entropic contribution, which can be explained by considering the loss of preferential polar interactions,

which causes the release of the water molecules structured around the TOCN [5] Generally, this combination indicates that the process is spontaneous at any temperature, as proven by the ΔG° values, and was observed to be negative at any temperature. Compared with other adsorbents, the results show that 'TOCN-MPS 300' has the highest negative value of Gibbs energy. Therefore, there is no surprise in TOCN-MPS adsorbing lysozyme in large quantities over a short period of time.

4.3.4. Protein adsorption performance: Kinetic analyses

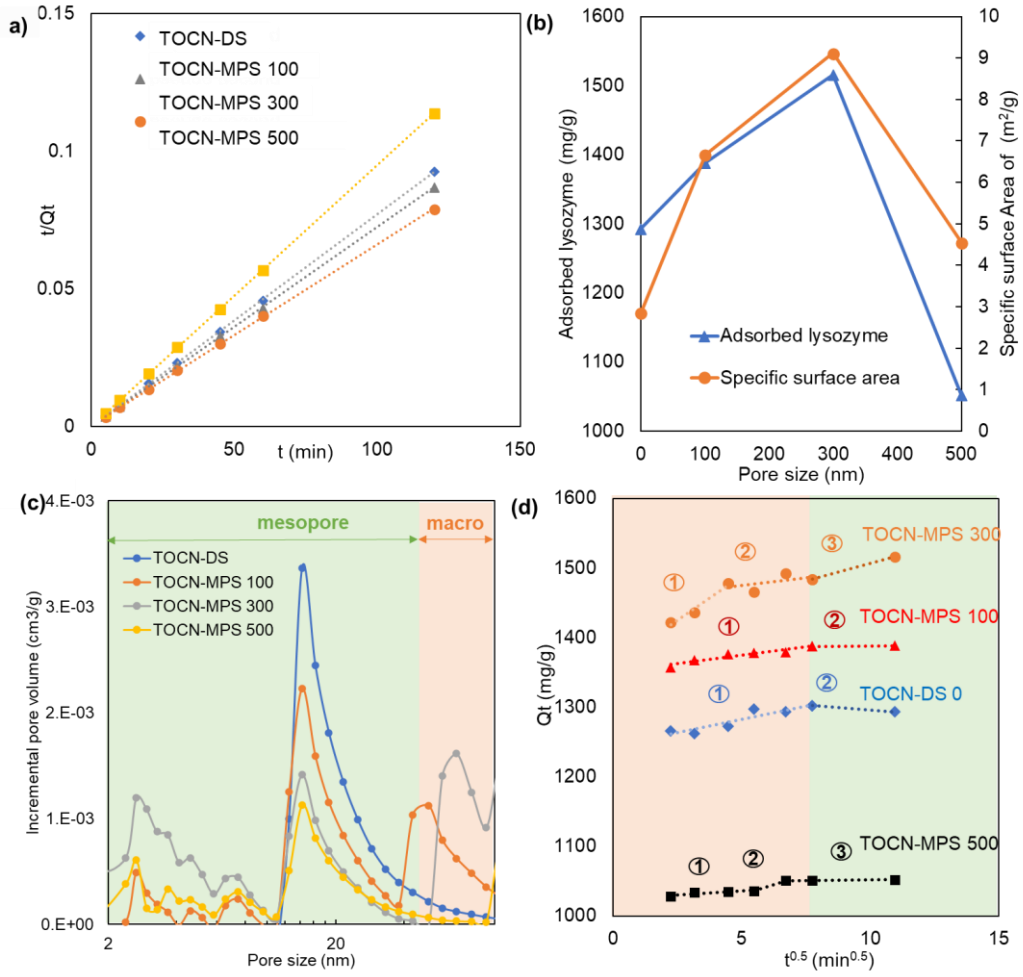

Figure 4.7*. (a) PSO fitting plot (b) Influence of macropore size on the SSA and TOCN-MPS adsorption capacity (c) Pore size distribution plots: mesopore-macropore (2–200 nm) calculated by the Barrett-Joyner-Halenda model, micropore (<2 nm) derived from HK calculations. (d) Weber and Morris intraparticle diffusion plots.*

Even though all particles have almost identical zeta potential values, there is a clear difference in the adsorption capacity of each particle (**Table 4.3**). This highlights that effective and efficient adsorption not only depends on the electrostatic interaction acting as a driving force, but also that the optimum particle structure plays a role in enhancing fluid diffusion to reach the binding

site. Interestingly, 'TOCN-MPS 300' exhibits the highest adsorbance capacity of all particles (1,516 mg/g). The higher adsorption capacity of 'TOCN-MPS 300' is considered as a result of possessing an optimized structure having the following three properties: (i) a large SSA and pore volume; (ii) optimal pore size and a broad size distribution; and (iii) open macropores with a desired TOCN distribution on the skeleton and inside the macroporous.

PFO and PSO models were calculated to understand the rate of adsorption (detailed calculations in chapter 3) and the results are presented in **Table 4.3**. From the value of the correlation coefficient (R^2), the PSO rate was observed to be the dominant kinetic process because the R^2 value of PSO was ~1 (0.999) and the R^2 value of PFO was <0.8. Proper fitting of the PSO model (**Figure 4.7a**) supports the assumption that the rate of adsorption on the active sites is highly influential and that the rate-limiting adsorption step is likely to be chemisorption.[21,22]. In other words, chemisorption process such as electrostatic forces and hydrogen bonding were observed to play a significant role in the binding reaction in the system.[23]

Table 4.4 *Kinetic parameters for lysozyme adsorption onto TOCN-MPS.*

	TOCN-DS	**TOCN-MPS**		
		100	**300**	**500**
Q_e **(mg/g)**	1293	1388	1516	1052
Kinetics Parameters				
PFO Model				
Q_1 (mg/g)	30.81	0.45	80.16	29.89
R^2	0.39	0.12	0.56	0.74
PSO Model				
Q_2 (mg/g)	1297	1378	1520	1054
R^2	1.00	1.00	1.00	1.00

Compared with the TOCN-DS and TOCN particles, which possess a dense core, the TOCN-MPS particles exhibit a higher SSA with a broader macro-mesopore pore size distribution. These results indicate that the macroporous structure successfully increased the accessibility of the binding sites by preventing TOCN aggregation and by providing interconnected channels inside the TOCN-MPS particles. The adsorption capacity correlates well with SSA and pore volume, **Figure 4.7b** and **Table 4.2**. Since the TCON-MPS particles have similar zeta potential, the results show that a better mass transfer process increases the number of readily active sites to adsorb protein. 'TOCN-MPS 300', which exhibits the highest surface area also displays the highest adsorption capacity, contributed by the high

pore volume derived from the mesopores. Considering that the dimensions of lysozyme are 4.5 × 3.0 × 3.0 nm^3,[24] the large surface area combined with an abundance of ordered mesopores becomes an essential factor to enhance the adsorption performance. The origin of the mesopores derives from the space between the TOCN network and the interconnected MPS pore channels. The observed peak in the pore size distribution plot, with the range of 20–50 nm, results from the void between the TOCN network, confirmed by the same peak (pore size range of 20–50 nm) attributed to the TOCN particle. However, the pore size within the range of 2–20 nm derives from the interconnected channels between the macropores proven by the same peak within the pore size distribution plot of MPS.

As shown in **Figure 4.7c**, the 'TOCN-MPS 300' particles exhibit a broad pore size distribution within the meso-macropore range with a more evenly distributed pore volume indicating that 'TOCN-MPS 300' possesses highly interconnected channels with open macropores across a 50–200 nm size range. Thereafter, TOCN deposition induces an abundance of accessible binding sites that enhances the capacity for protein adsorption. In short, the 'TOCN-MPS 300' particles fulfill the second and third criteria, where this material exhibits the highest SSA combined with an abundance of mesopores and interconnected channels whilst maintaining open macropores.

The Weber-Morris function was calculated, and the results plotted in **Figure 4.7d**, which show the intraparticle diffusion model for solid/solution interfaces. The TOCN-DS and 'TOCN-MPS 100' particles showed two linear lines in the Weber Morris plot, while 'TOCN-MPS 300' and 'TOCN-MPS 500' show three linear lines. Overall, the kinetics data exhibit multi-linear lines, that means a multi-step diffusion process controlled the adsorption process.[25] Hence, from the aforementioned explanation and the Weber-Morris calculation (**Figure 4.7d**), a schematic of the lysozyme adsorption process is proposed as shown in **Figure 4.8**.

As illustrated in **Figure 4.8**, for TOCN-DS, initially lysozyme is adsorbed onto the solid TOCN surface, and thereafter, is followed by slow diffusion inside the TOCN layer, which is composed of mesopores. Subsequently, since TOCN-DS has a dense core, the equilibrium is quickly achieved after lysozyme is adsorbed onto the outer surface of the particles. The 'TOCN-MPS 100' particles also show a two-step diffusion process. However, the 'TOCN-MPS 100' particles exhibit a higher initial adsorption capacity when compared with the TOCN-DS particles. Hence, the first diffusion step is not only as a result of the adsorption on the outer solid surface but also by penetration through the macroporous

structure. Additionally, because the 'TOCN-MPS 100' particles have a porous core, a slow second diffusion is considered to be presented inside the TOCN layer through the mesoporous structure.

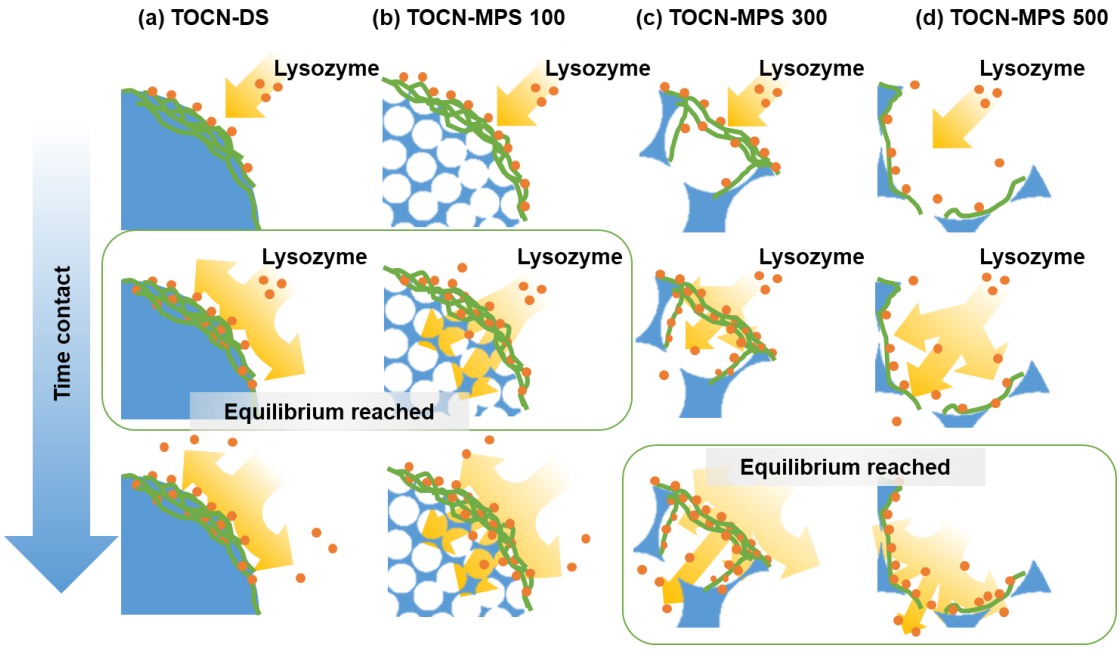

Figure 4.8. *Lysozyme adsorption mechanism. (a) Lysozyme only adsorbed on the surface of TOCN-DS particles. (b) Most of lysozyme adsorbed on the outer surface of TOCN-MPS 100 particles because the open macropores almost completely closed by TOCN. (c) Lysozyme could be partially adsorbed into porous structure by penetration through open macroporous with size of ~100 nm or >200 nm. (d) In contrast, almost all macropores were open and lysozyme could be adsorbed into interior macropores of TOCN-MPS 500 particles.*

For the 'TOCN-MPS 300' particles, the Weber Morris plot shows three linear lines that indicate a three-step diffusion process. As illustrated in **Figure 4.8,** lysozyme first penetrates through the macropores and is transferred across the external surface. Thereafter, the second linear line derives from mesopore diffusion where the fluid contains non-adsorbed lysozyme that diffuses into the macroporous structure and is adsorbed onto the binding sites dispersed within the macropores. The third linear line indicates that the molecules diffuse further into the smaller mesopore and micropore regions to the binding sites. The 'TOCN-MPS 500' particles also show a three-step diffusion process, however, at lower adsorption capacities. The macropore size of 'TOCN-MPS 500' particles were significantly larger compared with the lysozyme dimensions which allows better diffusion transport thoroughly

into the binding sites. However, large macroporous somewhat causes less ordered porous structure. It was indicated by the lowest total pore volumes (**Table 4.2**) and lower number of mesopores compared to other particles (**Figure 4.7c**). Hence, equilibrium is quickly achieved at low capacities. In summarizing, and taking into consideration the previous explanation, when the MPS size is within range of the TOCN length, the optimum size to realize an effective and efficient adsorption process is achieved.

4.3.5. Protein adsorption performance: Isothermal analyses

To better understand the protein adsorption mechanisms for different pore-engineered TOCN-MPS materials that have a complex heterogeneous porous structure and poorly understood adsorbents, adsorption isotherm models that describe the amount of protein adsorbed on the adsorbent as a function of protein concentration was conducted. Isotherm parameters were obtained through a nonlinear fit of experimental data with seven model isotherm equations, as calculated by the equation in **Table 4.5**. **Figure 4.9a** and **Table 4.6** shows the overall results of R^2.

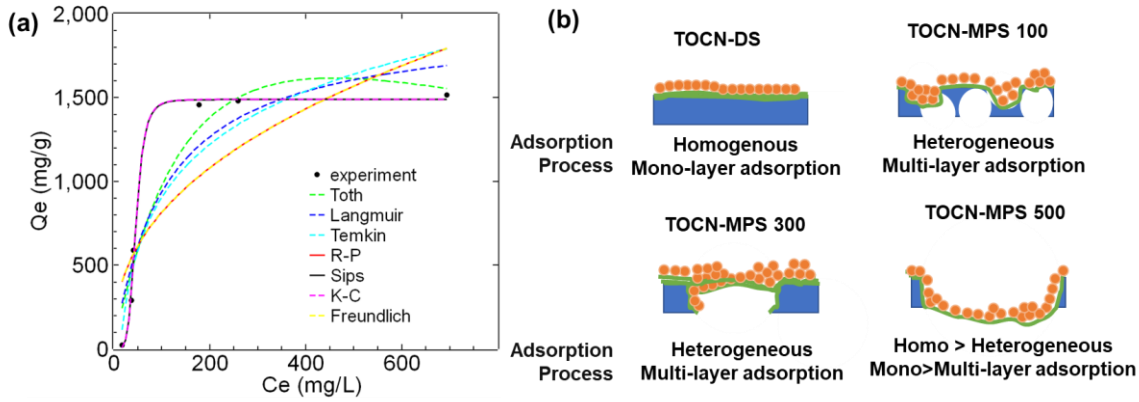

Figure 4.9. *(a) Adsorption isotherm fitting of lysozyme onto 'TOCN-MPS 300'. (b) Illustrated adsorption process of TOCN-MPS particles based on Sips and Toth models*

***Table 4.5**. Adsorption isothermal models.*

Isotherm models	Nonlinear equation	Linear equation	Ref.
Two-parameter isotherms			
Langmuir	$Q_e = \frac{Q_{max} k_L C_e}{1+k_L C_e}$	$\frac{1}{Q_e} = \frac{1}{K_L Q_{max} C_e} + \frac{1}{Q_{max}}$	[26]
Freundlich	$Q_e = k_F {C_e}^{\frac{1}{n}}$	$\log Q_e = \log k_F + \left(\frac{1}{n}\right) log C_e$	[27]
Temkin	$Q_e = \frac{RT}{b_T} ln A_T C_e$	$Q_e = \frac{RT}{b_T} \ln A_T - \frac{RT}{b_T} ln\ C_e$	[28]
Three-parameter isotherms			
Redlich-Peterson	$Q_e = \frac{k_R C_e}{1+a_R {C_e}^g}$	$\ln\left(k_R \frac{C_e}{Q_e} - 1\right) = g \ln C_e + ln\ a_R$	[29]
Sips	$Q_e = \frac{k_S {C_e}^n}{1+Q_{max} {C_e}^n}$	$\ln\left(\frac{Q_e}{Q_{max}-Q_e}\right) = \frac{1}{n} \ln C_e + ln k_S$	[30]
Koble-Corrigan	$Q_e = \frac{A {C_e}^n}{1+B {C_e}^n}$	$\frac{1}{Q_e} = \frac{1}{A {C_e}^n} + \frac{B}{A}$	[31]
Toth	$Q_e = \frac{k_T C_e}{(a_T + C_e)^{\frac{1}{t}}}$	$ln \frac{Q_e}{k_T} = \ln C_e - \frac{1}{t} \ln (a_T + C_e)$	[32]

When fitting two-parameter isotherm models, linear equations were used to plot the y values as a function of *Qe* vs the x values as function of *Ce*. From the linear line, various constant values were obtained. When fitting three-parameter isotherm models, nonlinear equations were used, and all three isotherm constants were evaluated with the use of a solver add-in function in Microsoft Excel. Thereafter, after calculating all parameters, the values of *Qe* were recalculated using a nonlinear equation. The difference in the *Qe* values derived from the experimental data from different isotherm models was obtained by analyzing the coefficient of determination (R^2) following the below equation:

$$R^2 = \frac{\sum (Q_{e,cal} - Q_{e,exp})^2}{\sum (Q_{e,cal} - Q_{e,exp})^2 + (Q_{e,cal} - Q_{e,exp})^2} \quad 4.11$$

Table 4.6. *Coefficient of determination parameters, R^2, for the adsorption isotherms of lysozyme onto TOCN-MPS.*

	TOCN-DS	TOCN-MPS		
		100	**300**	**500**
Langmuir	0.79	0.82	0.83	0.77
Freundlich	0.77	0.80	0.82	0.85
Redlich-Peterson (R-P)	0.77	0.80	0.82	0.85
Sips	0.89	0.94	0.99	0.94
Koble-Corrigan (K-C)	0.89	0.94	0.99	0.94
Temkin	0.85	0.89	0.92	0.92
Toth	0.90	0.93	0.97	0.93

Overall, the fit of the Sips, K-C and Toth models were correlated relatively well to the experimental data. The Toth model is applicable to predict heterogeneous adsorption with the assumption that the majority of the sites have an adsorption energy lower than the peak or maximum adsorption energy usually applied.[32,33] While the Sips and K-C models predict only the heterogeneity and the interactions between the particle surface with the adsorbed molecule.[30,31,34] The constants *o* and *n* indicate the level of heterogeneity in the system for the Toth, Sips and K-C models, respectively, and if the respective values deviate away from one this indicates that the system will be heterogeneous. As illustrated in **Figure 4.9b**, the particles containing the fibrous network on the porous surface (MPS 100 and MPS 300) are more heterogeneous and provide multi-layer adsorption (o <0.6 and n <0.4) when compared with particles (DS and MPS500) having no fibrous networks on the porous surface (o >0.6 and n >0.5). These results indicate that the adsorbent surfaces are more complex and comprise multiple sets of adsorption site energies and levels, which leads to heterogeneous adsorption and a combination of mono- and multi-layer adsorptions.[28]

4.4 Conclusion

In this study, composite nanostructured particles loaded with TOCN on the surface were successfully prepared demonstrating outstanding adsorption capabilities. The differences in structure and pore size in the macropore range influenced the variation in TOCN loading deposition and the respective adsorption performance. Because TOCN has a high aspect ratio, the deposition is observed not only on the external surface of the skeleton, but also within the internal porous structure. All particles exhibit excellent adsorption

abilities (>1,000 mg/g) in <5 min. Interestingly, the 'TOCN-MPS 300' particle, which has a TOCN network stretching across the porous surface, exhibits the highest adsorption capacity. Even though all particles have a high negative zeta potential and spontaneous adsorption, 'TOCN-MPS 300' successfully satisfies the three criteria to be an advanced adsorbent: first, the surface is highly negatively-charged, which induces effective adsorption (adsorption capacities >1,500 mg/g); second, a high surface area and pore volume is achieved with >50% of the total pore volume being mesoporous; and third, efficient ingress of guest molecules through open and continuous macroporous channels proven by the observed broad pore size distribution and a multi-step diffusion process calculated from the Morin-Weber models. Furthermore, the complex structure of 'TOCN-MPS 300' provides an abundance of accessible active sites that can adsorb large molecules such as lysozyme through a multi-layer adsorption process *via* a pore-filling mechanism.

4.5 References

[1] A.M. Rahmatika, Y. Goi, T. Kitamura, W. Widiyastuti, T. Ogi, TEMPO-oxidized cellulose nanofiber (TOCN) decorated macroporous silica particles: Synthesis, characterization, and their application in protein adsorption, Mater. Sci. Eng. C. 105 (2019) 110033.

[2] T. Saito, S. Kimura, Y. Nishiyama, A. Isogai, Cellulose nanofibers prepared by TEMPO-mediated oxidation of native cellulose, Biomacromolecules. 8 (2007) 2485–2491.

[3] A. Isogai, T. Saito, H. Fukuzumi, TEMPO-oxidized cellulose nanofibers, Nanoscale. 3 (2011) 71–85.

[4] H. Voisin, L. Bergström, P. Liu, A. Mathew, Nanocellulose-Based Materials for Water Purification, Nanomaterials. 7 (2017) 57.

[5] S. Lombardo, W. Thielemans, Thermodynamics of adsorption on nanocellulose surfaces, Cellulose. 26 (2019) 249–279.

[6] A.M. Rahmatika, W. Yuan, A.F. Arif, R. Balgis, K. Miyajima, G.M. Anilkumar, K. Okuyama, T. Ogi, Energy-efficient templating method for the industrial production of porous carbon particles by a spray pyrolysis process using poly(methyl methacrylate), Ind. Eng. Chem. Res. 57 (2018) 11335–11341.

[7] A.F. Arif, R. Balgis, T. Ogi, T. Mori, K. Okuyama, Experimental and theoretical approach to evaluation of nanostructured carbon particles derived from phenolic resin

via spray pyrolysis, Chem. Eng. J. 271 (2015) 79–86.

[8] R. Balgis, L. Ernawati, T. Ogi, K. Okuyama, L. Gradon, Controlled surface topography of nanostructured particles prepared by spray-drying process, AIChE J. 63 (2017) 1503–1511.

[9] T. Ogi, A.B.D. Nandiyanto, K. Okuyama, Nanostructuring strategies in functional fine-particle synthesis towards resource and energy saving applications, Adv. Powder Technol. 25 (2014) 3–17.

[10] A.F. Arif, Y. Chikuchi, R. Balgis, T. Ogi, K. Okuyama, Synthesis of nitrogen-functionalized macroporous carbon particles via spray pyrolysis of melamine-resin, RSC Adv. 6 (2016) 83421–83428.

[11] R. Balgis, T. Ogi, A.F. Arif, G.M. Anilkumar, T. Mori, K. Okuyama, Morphology control of hierarchical porous carbon particles from phenolic resin and polystyrene latex template via aerosol process, Carbon N. Y. 84 (2015) 281–289.

[12] H.N. Abdelhamid, H.-F. Wu, Proteomics analysis of the mode of antibacterial action of nanoparticles and their interactions with proteins, TrAC Trends Anal. Chem. 65 (2015) 30–46.

[13] S. Patil, A. Sandberg, E. Heckert, W. Self, S. Seal, Protein adsorption and cellular uptake of cerium oxide nanoparticles as a function of zeta potential, Biomaterials. 28 (2007) 4600–4607.

[14] S. Shen, P.S. Chow, S. Kim, K. Zhu, R.B.H. Tan, Synthesis of carboxyl-modified rod-like SBA-15 by rapid co-condensation, 321 (2008) 365–372.

[15] G.T. Beckham, J.F. Matthews, Y.J. Bomble, L. Bu, W.S. Adney, M.E. Himmel, M.R. Nimlos, M.F. Crowley, Identification of amino acids responsible for processivity in a family 1 carbohydrate-binding module from a fungal cellulase, J. Phys. Chem. B. 114 (2010) 1447–1453.

[16] J. Men, R. Wang, X. Hu, H. Zhao, H. Wei, C. Hu, B. Gao, Preparation of heparin-functionalized microspheres and study on their adsorption characteristic for basic protein lysozyme, Macromol. Res. 24 (2016) 114–122.

[17] H. Larsericsdotter, S. Oscarsson, J. Buijs, Thermodynamic analysis of lysozyme adsorbed to silica, J. Colloid Interface Sci. 276 (2004) 261–268.

[18] P.C.G. Mól, L.A.A. Veríssimo, M.R. Eller, V.P.R. Minim, L.A. Minim, Development of an affinity cryogel for one step purification of lysozyme from chicken egg white, J. Chromatogr. B. 1044–1045 (2017) 17–23.

[19] J. Kim, R.J. Desch, S.W. Thiel, V. V. Guliants, N.G. Pinto, Energetics of biomolecule adsorption on mesostructured cellular foam silica, Microporous Mesoporous Mater. 170 (2013) 95–104.

[20] K. Mishra, P.K. Das, Thermodynamics of adsorption of lysozyme on gold nanoparticles from second harmonic light scattering, Phys. Chem. Chem. Phys. 21 (2019) 7675–7684.

[21] X. Guo, J. Wang, A general kinetic model for adsorption: Theoretical analysis and modeling, J. Mol. Liq. 288 (2019) 111100.

[22] X. He, K.B. Male, P.N. Nesterenko, D. Brabazon, B. Paull, J.H.T. Luong, Adsorption and desorption of methylene blue on porous carbon monoliths and nanocrystalline cellulose, ACS Appl. Mater. Interfaces. 5 (2013) 8796–8804.

[23] R.H. Müller, D. Rühl, M. Lück, B.R. Paulke, Influence of fluorescent labelling of polystyrene particles on phagocytic uptake, surface hydrophobicity, and plasma protein adsorption, Pharm. Res. 14 (1997) 18–24.

[24] J.R. Deka, D. Saikia, Y.S. Lai, C.H. Tsai, W.C. Chang, H.M. Kao, Roles of nanostructures and carboxylic acid functionalization of ordered cubic mesoporous silicas in lysozyme immobilization, Microporous Mesoporous Mater. 213 (2015) 150–160.

[25] G. Ersan, Y. Kaya, M.S. Ersan, O.G. Apul, T. Karanfil, Adsorption kinetics and aggregation for three classes of carbonaceous adsorbents in the presence of natural organic matter, Chemosphere. 229 (2019) 515–524.

[26] H.-J. Kang, J.-H. Kim, adsorption kinetics, mechanism, isotherm, and thermodynamic analysis of paclitaxel from extracts of taxus chinensis cell cultures onto sylopute, Biotechnol. Bioprocess Eng. 24 (2019) 513–521.

[27] H.M.F. Freundlich, Adsorption in solution, Z. Phys. Chem. (1906).

[28] K.Y. Foo, B.H. Hameed, Insights into the modeling of adsorption isotherm systems, Chem. Eng. J. 156 (2010) 2–10.

[29] O. Redlich, D.L. Peterson, A Useful Adsorption Isotherm, J. Phys. Chem. 63 (1959) 1024–1024.

[30] I. Langmuir, the adsorption of gases on plane surfaces of glass, mica and platinum., J. Am. Chem. Soc. 40 (1918) 1361–1403.

[31] R.A. Koble, T.E. Corrigan, Adsorption isotherms for pure hydrocarbons, Ind. Eng. Chem. 44 (1952) 383–387.

[32] J. Toth, State Equations of Solid-Gas Interface Layers, Acta Chim. Acad. Sci. Hungaricae. 69 (1971) 311–317.

[33] K. Vijayaraghavan, T. Padmesh, K. Palanivelu, M. Velan, Biosorption of nickel(II) ions onto sargassum wightii: Application of two-parameter and three-parameter isotherm models, J. Hazard. Mater. 133 (2006) 304–308.

[34] A. Günay, E. Arslankaya, İ. Tosun, Lead removal from aqueous solution by natural and pretreated clinoptilolite: Adsorption equilibrium and kinetics, J. Hazard. Mater. 146 (2007) 362

Chapter 5

Summary and Conclusions

Adsorption of proteins has enabled the development of diverse biomedical applications. Thus, developing a novel advanced protein adsorbent that exhibited excellent adsorption performance, relatively low-cost and practical feasible is highly demanded. This dissertation was aimed to develop an advanced protein adsorbent by engineering hierarchical macro/mesoporous structures that offer an abundance of accessible binding sites by combining the advantage of macroporous particles with TEMPO oxidized cellulose nanofibers. Furthermore, the mechanism of protein adsorption onto our material was approached by theoretical adsorption equations. The major highlights of this dissertation are followed:

1. Template selection is a critical step to determine an effective and efficient method for the synthesis of macroporous materials. In this study, we introduce the use of the low-cost poly(methyl methacrylate) (PMMA) as a template in a spray pyrolysis process for the synthesis of a porous carbon particle. In this study, we found that despite having the same morphology, the PMMA template produced two times higher specific surface area than that using polystyrene latex (PSL) template. The high surface area is attributed to the low PMMA decomposition residue and the formation of a micropore and a mesopore. The use of PMMA reduces the energy consumption for template decomposition by 32% compared with PSL. This benefit suggests an excellent potential for the use of PMMA in the scaled-up production of porous materials.
2. In developing of adsorbent, macroporous particles as supporting material used to load TEMPO oxidized cellulose nanofibers (TOCN) as anionic polymer. The TOCN@macroporous SiO_2 particle has a unique cellulose nanofiber network structure on the macroporous, highly-negative zeta potential (-62 ± 2 mV) and relatively high surface area for cellulose based particles. The interesting point here is TOCN@macroporous SiO_2 particle had a similar functional group, similar zeta potential, yet higher surface area than that of pure TOCN. As a result, these TOCN@macroporous SiO_2 characteristics provide sites rich with electrostatic interaction to exhibit an outstanding adsorption capacity of lysozyme, rapid adsorption, good reusability, and good release of the adsorbate. The results suggest the potential for TOCN@macroporous

SiO_2 particles in drug delivery, protein adsorption, and other applications in the biomedical field.

3. As a further development of TOCN@macroporous SiO_2 particles, the differences in structure and pore size in the macropore is demonstrated the variation in CNF loading deposition and the respective adsorption performance. The as-prepared adsorbent particles exhibited a high negative charge (~−59 mV) and excellent protein adsorption ability (>1,000 mg/g) in <5 min. Furthermore, tuning the macropore size influenced the CNF deposition either to the external surface or penetrating within the pores. As a result, the optimum macropore successfully enhances the adsorption capability to >1,500 mg/g as a result of improved interconnectivity between the channels. Here exposed macropores of >100 nm allows ingress of protein to the interior structure that houses an abundance of binding sites comprising the dispersed TOCN. Additionally, the adsorption kinetics, thermodynamics, and isothermal parameters were studied to analyze the mechanism of lysozyme adsorption. The adsorption process is confirmed to occur spontaneously at any temperature with a pseudo-second-order model describing the kinetic model, and TOCN deposition affecting the heterogeneity of the binding sites. Furthermore, the complex structure provides an abundance of accessible active sites that can adsorb large molecules such as lysozyme through a multi-layer adsorption process *via* a pore-filling mechanism.

The presented TOCN@macroporous SiO_2 particles represent a promising adsorbent material to enhance adsorption capacity in rapid time. Moreover, we expect that the macroporous silica could be substituted with another material that is promising for wide application such as in protein adsorption, drug delivery, and biosensors.

Nomenclature

a_R	Redlich-Peterson isotherm constant	(1/mg)
a_S	Sips isotherm model constant	(L/mg)
a_T	Toth isotherm model constant	(L/mg)
A	Koble-Corrigan isotherm constant	($L^n mg^{1-n}/g$)
A_T	Temkin isotherm equilibrium binding constant	(L/g)
b_T	Temkin isotherm constant	
B	Koble-Corrigan isotherm constant	$(L/mg)^n$
C_0	Lysozyme concentration before adsorption	(mg/mL)
C_1	Lysozyme concentration after adsorption	(mg/mL)
C_2	Lysozyme concentration after desorption	(mg/mL)
C_e	Equilibrium concentration	(mg/mL)
C_x	Adsorbed lysozyme on adsorbent ($C_1 - C_0$)	(mg/mL)
g	Redlich-Peterson isotherm exponent	
K	Equilibrium constant (Q_e/C_e)	
k_F	Freundlich isotherm constant related to adsorption capacity	(mg/g) $(dm^3/g)^n$
k_L	Langmuir isotherm constant	(dm^3/mg)
k_R	Redlich-Peterson isotherm constant	(L/g)
k_S	Sips isotherm model constant	(L/g)
k_T	Toth isotherm constant	(mg/g)
k_1	PFO rate constant	(min^{-1})
k_2	PSO rate constant models	(g/mg·min)
m	Weight of adsorbent	(g)
n	Adsorption intensity, heterogeneity factor	
o	Toth isotherm constant, heterogeneity factor	
Q_e	Lysozyme uptake in the adsorbent at equilibrium	(mg/g)
Q_{e1}	Equilibrium adsorption capacity of the PFO model	(mg/g)
Q_{e2}	Equilibrium adsorption capacity of the PSO model	(mg/g)

Q_{max}	Maximum monolayer coverage capacity of lysozyme	(mg/g)
Q_t	Adsorption uptake as a function of time	(mg/g)
Q_S	Theoretical isotherm saturation capacity	(mg/g)
R	Universal gas constant	(8.314 J/mol·K)
R^2	Coefficient of determination	
R_{id}	Rate constant of intraparticle transport	
t	Time	(min)
T	Temperature	(K)
V	Solution volume	(mL)
W_{am}	Weight loss of porous silica after PDDA modification	(%)
W_{bm}	Weight loss of porous silica before PDDA modification	*(%)*
$W_{CNF-MPS}$	Weight loss of CNF-MPS after CNF loading	*(%)*
ΔH^0	*Enthalpy change*	*(kJ/mol)*
ΔS^0	*Entropy change*	*(J/mol·K)*
ΔG^0	*Gibbs free energy*	*(kJ/mol)*
ε	$RTln\left(1+\frac{1}{C_e}\right)$	
ζ	Zeta potential	mV

List of Tabels

List of Figures

List of Publications

1. **A. M. Rahmatika**, Y. Weilin, A. F. Arif, R. Balgis, K. Miyajima, G. M. Anilkumar, K. Okuyama ,T. Ogi, Energy-efficient templating method for the industrial production of porous carbon particles by a spray pyrolysis process using poly(methyl methacrylate), ***Industrial & Engineering Chemistry Research***, 57(33), 11335-11341, July, 2018.
2. **A. M. Rahmatika**, Y. Goi, T. Kitamura, W. Widiyastuti, T. Ogi, TEMPO-Oxidized Cellulose Nanofiber (TOCN) decorated macroporous silica particles: synthesis, characterization, and their application in protein adsorption, ***Materials Science and Engineering: C***, 105, 110033, July, 2019.
3. T. Ogi, H. Fukazawa, **A. M. Rahmatika**, T. Hirano, K. L. A. Cao, F. Iskandar, Improving the crystallinity and purity of monodisperse Ag fine particles by heating colloidal sprays in-flight, ***Industrial & Engineering Chemistry Research***, 59(13), 5745-5751,
4. **A. M. Rahmatika**, Y. Goi, T. Kitamura, Y. Morita, F. Iskandar, T. Ogi, Silica-supported carboxylated cellulose nanofibers for effective lysozyme adsorption: Effect of macropore size, ***Advanced Powder Technology***, 2020 in press.
5. L. Gradon, R. Balgis, T. Hirano, **A. M. Rahmatika**, T. Ogi, K. Okuyama, Advanced aerosol technologies towards structure and morphologically controlled next-generation catalytic materials, ***Journal of Aerosol Science***, 2020 in press.

Acknowledgment

Praise be to the God almighty for His merciful blessing.

I would like to express my deepest gratitude to Associate Professor Takashi Ogi who gave me the opportunity to work in his group and helped me to gather the knowledge needed to compose this dissertation, the freedom to fulfill my scientific aims and the possibility to collaborate with an international scientific community. I am also grateful to Professor Kikuo Okuyama, Assistant Professor Ratna Balgis, and Dr. Aditya Farhan Arif for all their help and advice.

A special gratitude to my Ph.D referees: Prof. Toshinori Tsuru, Prof. Akihiro Yabuki and Prof. Kiyofumi Katagiri for the constructive critics, suggestions, and insights.

I would like to thank all my former and current colleagues of the Thermal Fluid and Engineering group, special mention goes to Mrs. Tachibana, En, Nishida, Ghana, Taniguchi, Kamikubo, Hirano, Kiet, Kikkawa, Toyoda, and Tue for their collaboration, laugh, support and the familiar atmosphere which always helped me despite of language barrier. Furthermore, I would like to acknowledge all my co-authors Dr. Widiyastuti from Institut Teknologi Sepuluh Nopember and Assoc. Prof. Ferry Iskandar from Institut Teknologi Bandung for the constructive advice improving the quality of the manuscripts and this dissertation.

I also indebted to Ministry of Education, Culture, Sports, Science, and Technology of Japan for the Ph. D scholarship and to Hosokawa Foundation for the research fund.

I am truly grateful to my colleagues in Universitas Gadjah Mada and my friends in Higashihiroshima for their ongoing support and the continual encouragements. My acknowledgement would be incomplete without thanking the biggest source of my strength, my beloved mother, Choiriyah, my sister Irma, and my brothers Ivan and Adit. I would like to dedicate this work to them for listening, watching over me and praying for me constantly even in the midst of a bad condition due to pandemic

Annie Mufyda Rahmatika